Nanofotonische adaptieve antennes
op basis van siliciumchips voor draadloze optische toepassingen

Nanophotonic Beamsteering Elements
Using Silicon Technology for Wireless Optical Applications

Karel Van Acoleyen

Promotor: prof. dr. ir. R. Baets
Proefschrift ingediend tot het behalen van de graad van
Doctor in de Ingenieurswetenschappen: Fotonica

Vakgroep Informatietechnologie
Voorzitter: prof. dr. ir. D. De Zutter
Faculteit Ingenieurswetenschappen en Architectuur
Academiejaar 2011 - 2012

UNIVERSITEIT
GENT

ISBN 978-90-8578-525-5
NUR 959
Wettelijk depot: D/2012/10.500/51

Universiteit Gent
Faculteit Ingenieurswetenschappen en Architectuur
Vakgroep Informatietechnologie

Nanophotonic Beamsteering Elements Using Silicon Technology for Wireless Optical Applications

Nanofotonische adaptieve antennes op basis van siliciumchips voor draadloze optische toepassingen

Karel Van Acoleyen

Proefschrift tot het bekomen van de graad van
Doctor in de Ingenieurswetenschappen:
Fotonica
Academiejaar 2011-2012

Promotor:

Prof. Dr. Ir. Roel Baets

Examencommissie:

Prof. Dr. Ir. Rik Van de Walle (voorzitter)	Universiteit Gent, ELIS
Prof. Dr. Ir. Roel Baets (promotor)	Universiteit Gent, INTEC
Prof. Dr. Ir. Wim Bogaerts (secretaris)	Universiteit Gent, INTEC
Prof. Dr. Ir. Hendrik Rogier	Universiteit Gent, INTEC
Prof. Dr. Ir. Herbert De Smet	Universiteit Gent, ELIS
Prof. Dr. Dominic O'Brien	University of Oxford
Prof. Ir. Ton Koonen	TU Eindhoven

Universiteit Gent
Faculteit Ingenieurswetenschappen en Architectuur

Vakgroep Informatietechnologie
Sint-Pietersnieuwstraat 41, B-9000 Gent, België

Tel.: +32-9-264.33.16
Fax.: +32-9-331.35.93

Dit werk kwam tot stand in het kader van een aspirantenbeurs van het Fonds voor Wetenschappelijk Onderzoek - Vlaanderen (FWO-Vlaanderen).

Dankwoord

Het zit erop. Welgeteld drie jaar en acht maanden waarin ik heel wat heb beleefd en veel nieuwe mensen heb leren kennen. Ze zijn alweer voorbijgevlogen. Het is nu al iets meer dan 5 jaar geleden dat ik voor het eerst in contact kwam met fotonica, gegeven door prof. Roel Baets. Wist ik toen wat voor een avontuur me te wachten stond. Via het Erasmus Mundus Master of Science in Photonics programma stortte ik me direct in een buitenlands fotonica avontuur in Zweden. Mede dankzij deze ervaring besloot ik om me toch wat verder te verdiepen in deze wondere wereld en begon ik mijn doctoraat aan de UGent, onder leiding van diezelfde prof. Roel Baets, wie ik dan ook als eerste wens te bedanken om dit avontuur mogelijk te maken.

Als tweede zou ik graag prof. Hendrik Rogier bedanken voor zijn steun en begeleiding in het eerste jaar van mijn doctoraat. Ook al is het doctoraat een andere richting uitgegaan, kijk ik daar toch tevreden op terug. Vervolgens een woord van dank aan de overige leden van de examencommissie, prof. Herbert De Smet, prof. Ton Koonen, prof. Dominic O'Brien en prof. Wim Bogaerts voor hun waardevolle feedback, vragen en suggesties op dit werk.

Verder waren er uiteraard de collega's. Het is moeilijk om in dit dankwoord samen te vatten wat jullie allemaal voor mij hebben betekend. Ik heb dan ook veel mensen zien komen en gaan en daarin zijn ook enkele goede vriendschappen ontstaan: Elewout, ik denk dat er geen enkele zin is die onze band correct kan beschrijven; Cristina, dank voor alle leuke dansfeestjes waarvan er nog vele mogen komen; Kristof, om me onder te dompelen in films waarvan ik niet wist dat iemand zoiets maakt en aan wie ik het systeem van continue economische groei nog steeds moet verdedigen; Wout en Marie, oooh, de liefde kan toch zo mooi zijn; Joris, mijn mentor in de meetkamer, fruitpauze goeroe en van wiens rationele en objectieve kijk ik misschien nog iets kan leren. Jullie hebben het allemaal samen echt een tijd voor mij gemaakt om nooit meer te vergeten!

Daarnaast waren er de bureaugenoten. Bedankt om het een plezier te maken om elke dag naar de bureau te komen: Martin, die me altijd bijstond bij elke computer-, server- of simulatievraag; Bart en Yannick, voor een laatste update

van ofwel de beurs, het nieuws, of bepaalde ontwikkelingen in de groep; Marie en Nebiyu. Het was echt een waar genoegen om dit avontuur met jullie te delen.

En dan de rest van de collega's, de lijst is eindeloos lang: Eva, Peter D. H., Diedrik, Thijs, Thomas, Sam, Pauline, Nannicha, Martijn, Shankar, Stevan, Shahram, Sukumar, Gunay, ... bedankt voor de leuke werk en niet-werk gerelateerde discussies. Ook niet te vergeten zijn de mensen van de 'oude garde': dank aan Dave en Lieven voor de interessante koffiepauze onderwerpen, Joost, Koen, Peter D. B., Jonathan, ... om me als beginnend doctoraatsstudent te introduceren in de after-work café activiteiten. Ook nog dank aan Peter B. en Geert voor alle lekkere 'de Brug / Sint-Jans'-lunchen die me van de nodige energie voorzagen.

Een doctoraat kan je niet alleen doen. Ik zou dan ook graag een speciaal woord van dank richten aan alle mensen die het praktisch voor mij mogelijk gemaakt hebben al dit werk te verrichten: Kasia, voor haar processing hulp; Steven voor alle praktische hulp in de cleanroom; Liesbet voor onze uren samen in de SEM/FIB kamer; Luc en Peter G. die elke wild meetopstelling idee dat ik had tot een goed einde brachten; Manu en Michael, voor alle (meet)software hulp; Wim, voor een software-framework waar je wonderen mee kan verrichten als je maar het juiste commando te pakken krijgt; de Ilses, voor alle administratieve rompslomp tot een goed einde te brengen en Kristien die met een glimlach me altijd hielp bij elke computerprobleem.

Ook een woord van dank aan Pieter, die zich verdiept heeft in het (trage) geluid i.p.v. licht, bedankt voor de middagpauzes en na-middagpauze-drink waarin we onze onderzoeksfrustraties konden delen. Daarnaast zou ik ook graag mijn 'vrienden van het jeugdhuis' bedanken: Isabel, Filip, Susan, Lennert, Wim, Tom, Kevin, Valérie, Bert, Steffie, Frederik, Kelly, David, Francisca, Elisabeth en Wouter. Bedankt voor alle vrijdagavonden. Ook nog een woord van dank aan Ellen, om de laatste maand van mijn doctoraat toch net dat extraatje te geven.

Tot slot ook nog een speciaal woord van dank aan mijn ouders en familie, zonder wie dit allemaal niet mogelijk zou zijn.

Bedankt!

Gent, augustus 2012
Karel Van Acoleyen

Table of Contents

List of Figures

List of Tables

List of Acronyms

A

AEL	Accessible Emission Limit
ANSI	American National Standards Institute
AO	Acousto-Optic
APD	Avalanche Photo Diode
AWG	Arrayed Waveguide Grating

B

BCB	Benzocyclobutene
BPSK	Binary Phase Shift Keying

C

CCR	Corner Cube Reflector
CERR	Cat's Eye Retro Reflector
CMOS	Complementary Metal Oxide Semiconductor
CT	Computed Tomography

D

DI	Deionized

DOA	Direction Of Arrival
DT	Diffuse Tomography

E

EM	Electro-Magnetic
EIRP	Equivalent Isotropically Radiated Power
EO	Electro-Optic

F

FCC	Federal Communications Commission
FOV	Field Of View
FP7	European Framework Program 7
FSR	Free Spectral Range
FTTC	Fiber To The Cabinet/Curb
FTTH	Fiber To The Home
FWHM	Full Width at Half Maximum

H

HAN	Home Area Network
HD	High-Definition
HF	Hydrofluoric acid

I

IC	Integrated Circuit
IEC	International Electrotechnical Commission
IPA	Isopropyl alcohol, Isopropanol
IR	Infrared

L

LAN	Local Area Network
LC	Liquid Crystal
LC OPA	Liquid Crystal Optical Phased Array
LCPG	Liquid Crystal Polarization Grating
LED	Light Emitting Diode
LIDAR	Light Detection And Ranging
LOS	Line Of Sight

M

MAC	Media Access Control
Mbps	Megabit per second
MEMS	Micro-Electro-Mechanical Systems
MIMO	Multiple-Input Multiple-Output
MMI	Multimode Interference (splitter/combiner)
MO	Microscope Objective
MPW	Multi-Project Wafer
MRI	Magnetic Resonance Imaging
MSM	Metal Semiconductor Metal
MZI	Mach-Zehnder Interferometer

N

N/A	Not Applicable
NA	Numerical Aperture
NEMS	Nano-Electro-Mechanical Systems
NI	National Instruments

O

OCT	Optical Coherence Tomography
OFDM	Orthogonal Frequency Division Multiplexing
OPA	Optical Phased Array
OPD	Optical Path Difference
OSA	Optical Spectrum Analyzer

P

PCI	Peripheral Component Interconnect
PET	Positron Emission Tomography
PL	Path Loss
PIC	Photonic Integrated Circuit
PR	Photoresist
PXI	PCI EXtensions for Instrumentation

Q

QAM	Quadrature Amplitude Modulation
QPSK	Quadrature Phase Shift Keying

R

RCLED	Resonant Cavity Light Emitting Diode
RF	Radio Frequency

S

SEM	Scanning Electron Microscope

SLED	Superluminescent Light Emitting Diode
SNR	Signal-to-Noise Ratio
SOI	Silicon-On-Insulator

T

TE	Transverse-Electric
TO	Thermo-Optic

U

UV	Ultraviolet

V

VCSEL	Vertical Cavity Surface Emitting Laser

W

WDM	Wavelength Division Multiplexing

Nederlandse samenvatting –Summary in Dutch–

Optische draadloze verbindingen worden momenteel meer en meer belangrijk. Om aan de groeiende vraag naar meer bandbreedte te kunnen voldoen moeten nieuwe technologieën onderzocht worden. Uit voorspellingen blijkt immers dat de huidige draadloze technologie, die gebaseerd is op radiogolven, niet in staat zal zijn om de vereiste bandbreedte te leveren, niet enkel door technologische beperkingen, maar ook voor een groot deel door de heel stricte reglementeringen in de radio wereld. Voor lange-afstandscommunicatie is men reeds overgeschakeld van elektrische signalen die langs koperkabels verstuurd worden, naar optische signalen die door een optische vezel verstuurd worden. Deze optische signalen hebben immers een immens grote bandbreedte. Eenzelfde tendens kan men nu doortrekken naar draadloze toepassingen. Ook voor heel korte afstanden kunnen deze optische draadloze verbindingen een belangrijke rol vervullen. De snelheid van de huidige geïntegreerde circuits (ICs) is immers voor een groot deel beperkt door de koper verbindingen, die verschillende delen van eenzelfde IC verbinden of verschillende ICs met elkaar moeten verbinden. Optische interconnects is dan ook een belangrijk domein waar veel onderzoek naar verricht wordt en waar optische draadloze verbindingen een meerwaarde kunnen bieden.

De toepassingen van draadloze optische links reiken echter verder dan enkel communicatie. Optische detectie van materialen of gassen, opmeten van concentratie van gassen, meten van windsnelheden en opstellen van windprofielen. Het zijn enkele van de toepassingen waar men ook een draadloze optische link opstelt: licht wordt verzonden naar het te detecteren materiaal en het gereflecteerde licht wordt geanalyseerd. Dit gebeurt met een zogenaamde *licht radar* of *LIDAR* (Light Detection And Ranging). Deze wordt ook gebruikt bij het opstellen van topografie kaarten. Voor al deze toepassingen is het belangrijk om licht in verschillende richtingen efficiënt te kunnen uitsturen.

Optische Fasegestuurde Roosters

De meest voor de hand liggende manier om een lichtstraal te sturen is door bijvoorbeeld een spiegel mechanisch te bewegen. Wanneer men dit echter heel nauwkeurig wil doen, zijn de compontenten typisch zwaar, hetgeen nodig is voor de stabiliteit. Dit beperkt echter hun snelheid. Zulke structuren zijn bovendien ook gevoelig aan versnelling. Daarom hebben we in dit werk een manier gebruikt om een straal te sturen zonder enige mechanische beweging.

Hiervoor gebruiken we een Optisch Fasegestuurd Rooster (Engels: Optical Phased Array, OPA). Een OPA bestaat uit een rooster van elementen die licht uitsturen en waarvan men de fase van het licht dat elk element uitstuurt actief kan aanpassen. Op deze manier kan men een willekeurig fasefront van licht creëren. Hierdoor reiken de toepassingen van OPAs verder dan enkel sturing van het licht. We kunnen ook de vorm van de lichtstraal beïnvloeden om bijvoorbeeld licht te focussen. OPAs spelen ook een belangrijke rol in de zogenaamde adaptieve optica. Hier probeert men bijvoorbeeld het fasefront van licht te reconstrueren na propagatie door de atmosfeer. Dit wordt gebruikt in de astronomische beeldvorming of bij lange-afstand optische draadloze links door de atmosfeer. Ook in de medische beeldvorming kan men adaptieve optica gebruiken om drie-dimensionale beelden te creëren van weefsel.

De fabricage van OPAs is technologisch zeer uitdagend. Wanneer men een continue sturing over een groot bereik wenst, moeten de individuele elementen dichter bij elkaar staan dan een halve golflengte. Het is echter zeer moeilijk om aan deze voorwaarde te voldoen omwille van de zeer kleine golflengte van licht. Wanneer men bovendien een heel gerichte lichtstraal wil hebben, moet de totale apertuur groot zijn. Beide voorwaarden betekenen echter dat er een groot aantal elementen nodig is. Adressering van al deze elementen wordt dan ook problematisch. Aan beide voorwaarden wordt dan typisch ook niet voldaan. Om een groot sturingsbereik te verkrijgen gebruikt men meestal een cascade van stapsgewijze sturing over een groot bereik en nadien continue sturing over een klein bereik.

De meeste OPAs worden typisch gemaakt met vloeibare kristallen. Deze hebben echter een beperkte snelheid en een beperkt bereik. In dit werk werd het geïntegreerd silicium fotonica platform onderzocht om OPAs te fabriceren.

Silicium Fotonica

Momenteel wordt er zeer veel onderzoek verricht naar fotonische integratie. Het doel van deze integratie is om complexe functionaliteit te verkrijgen: geïntegreerde detectoren leveren ons hogere data snelheden, integratie be-

tekent miniaturisatie en dus een lager vermogensverbruik, meer nauwkeurige detectie wordt mogelijk. Dit alles is bovendien mogelijk tegen een lage kostprijs indien men in staat is om op grote schaal te produceren. Er is echter een veelvoud aan fotonische integratieplatformen: GaAs, InP, glas- of polymeergebaseerd, Si. De keuze in dit onderzoekswerk is gevallen op het silicium fotonica platform.

Er is een sterke rationale om te kiezen voor silicium als integratieplatform. Eerst en vooral is silicium transparant in het telecom gebied. Ten tweede heeft silicium-op-isolator (Engels: silicon-on-insulator, SOI) een hoog brekingsindex contrast, hetgeen zeer compacte integratie toelaat. Ten derde heeft men lage golfgeleider verliezen reeds aangetoond en geïntegreerde detectoren kunnen worden gemaakt door germanium te integreren. Het enige ontbrekende element om een optische link te kunnen opstellen is de generatie van licht. De indirecte energiekloof van silicium laat niet toe om op efficiënte wijze licht te genereren. Men kan echter wel overschakelen naar hybride integratie van III-V halfgeleiders, waarin het wel mogelijk is om efficiënt licht te genereren. Door silicium te gebruiken kan men bovendien de complexe en uiterst verfijnde fabricagetechnieken, ontwikkeld door de CMOS (Complementary Metal Oxide Semiconductor) industrie, aanwenden voor de ontwikkeling van fotonische structuren op nanometer schaal.

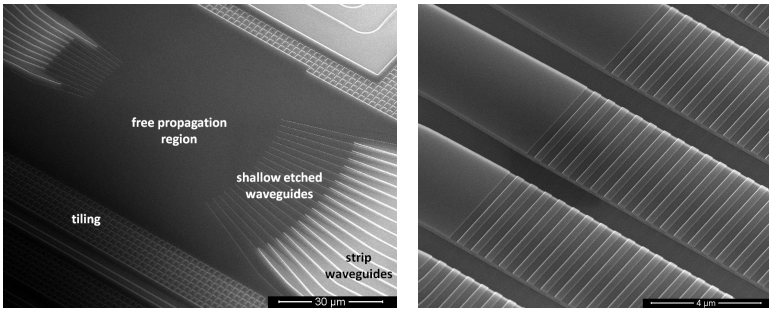

(a) (b)

Figuur 1: Rasterelektronenmicroscoop foto's van geïntegreerde componenten op silicium-op-isolator: (a) sterkoppelaar , (b) rooster van roosterkoppelaars.

Het silicium fotonica platform levert ons al de functionaliteit die nodig is om OPAs te maken: licht kan tussen verschillende elementen verdeeld worden door bijvoorbeeld een sterkoppelaar te gebruiken (Figuur 1(a)), het kan uit het vlak van de chip gestuurd worden door roosterkoppelaars (Figuur 1(b)) en de fase kan aangepast worden door middel van geïntegreerde fase tuners. Deze

aanpassing van de fase is een zeer belangrijk element van een OPA en werd in meer detail onderzocht.

Bij de eerste experimentele OPAs werden thermo-optische fase tuners gebruikt. Wanneer men een golfgeleider opwarmt, verandert diens brekingsindex en dus ook de fase van het licht in deze golfgeleider. Daarnaast hebben we ook een nieuwe soort fase tuner voorgesteld en aangetoond op basis van NEMS (Nano-Electro-Mechanische Systemen) technologie. Door een voltage aan te leggen over een ondergeëtste slot van een slotgolfgeleider, zal de slot samentrekken waardoor de effective index ervan wijzigt.

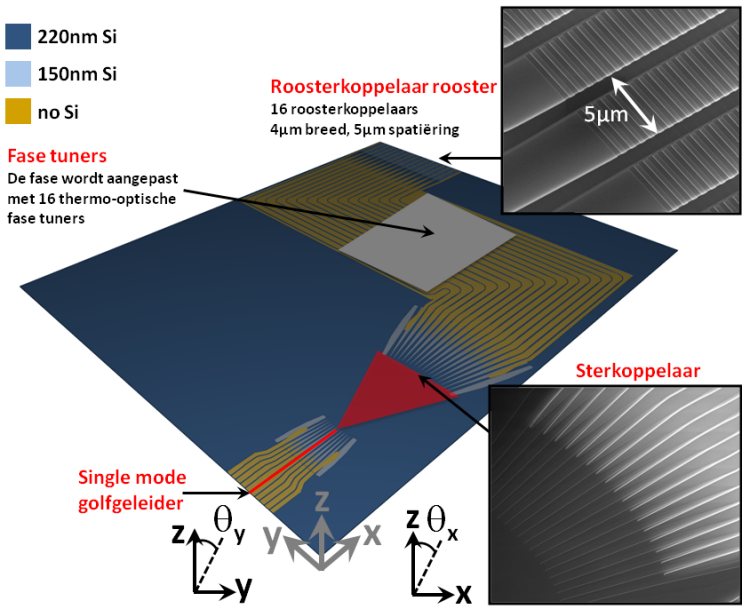

Figuur 2: Eén-dimensionale OPA met 16 thermo-optische fase tuners waarmee een random fasefront kan gecreëerd worden.

Experimentele resultaten

In dit werk werden één-dimensionale OPAs op SOI gefabriceerd en gekarakteriseerd zoals geschetst in Figuur 2. Met deze structuur werd een continue sturing van licht over een bereik van ±18° aangetoond, waarbij thermo-optische fase tuners gebruikt werden. Figuur 3 toont het één-dimensionale verre-veld patroon voor sturing van het licht naar 0°, 6°, 12° of 18°. Vermits we volledige controle hebben over het één-dimensionale fase front, komen ook verschillende andere toepassingen aan bod. Wanneer het fasefront zo geprogrammeerd

wordt dat het een lens nabootst, kunnen we het licht focussen boven de chip. Dit is vooral van belang bij optische detectietechnieken.

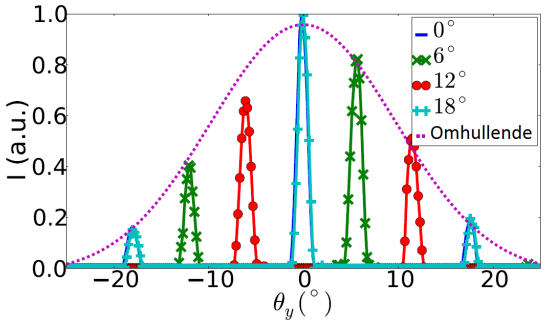

Figuur 3: Opgemeten verre-veld patroon in de θ_y-richting waarbij thermo-optisch gebaseerde sturing werd gebruikt. Het licht wordt naar een hoek van 0°, 6°, 12° of 18° gestuurd. De streepjeslijn duidt de omhullende van het verre-veld patroon aan.

Wanneer deze OPA als ontvanger gebruikt wordt, kan men het inkomende fase front onderzoeken door middel van de fase tuners. Dit werd gebruikt om te onderzoeken uit welke richting een lichtbundel invalt op de OPA (Engels: direction-of-arrival). Dit is nodig om een optische link aan hoge datasnelheden op te stellen, waarbij verzender en ontvanger nauwkeurig gealigneerd moeten worden. Daarnaast werden ook de mogelijkheden van deze OPA onderzocht om verstrooid licht coherent samen te voegen in een singlemode golfgeleider. Door de juiste fases te kiezen werd het opgevangen optisch vermogen met 10 dB verhoogd voor een OPA met 16 elementen. Dit heeft onder meer toepassingen in biologische spectroscopie.

Door de roosterkoppelaars in een twee-dimensionaal rooster te plaatsen, verkrijgt men een twee-dimensionale OPA. Zulke OPAs hebben echter typisch een grote spatiëring van de elementen en een lage vulfactor omwille van de adressering. De sturingsefficiëntie is dan ook sterk gelimiteerd en verschillende hogere orde lobes zijn zichtbaar. Figuur 4 toont een typische verre-veld patroon van zo een 2D OPA.

Waneer we een gelijkaardige structuur gebruiken als in Figuur 2, waarbij nu een vast lengteverschil geïntroduceerd wordt tussen de verschillende golfgeleiders in het fase tuner gebied, verkrijgt men een twee-dimensionale dispersieve structuur, waarbij het licht over een twee-dimensionale ruimte gestuurd wordt wanneer men de golflengte wijzigt. Door het vaste lengteverschil creëert men een gefaseerd golfgeleider rooster (Engels: arrayed waveguide grating, AWG), hetgeen typisch een rooster is van hoge orde. De roosterkoppelaar is daaren-

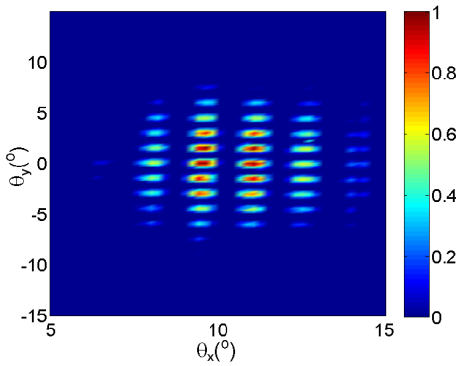

Figuur 4: Opgemeten verre-veld patroon van een 2 × 2 OPA op SOI.

tegen een rooster van lage orde. Deze twee roosters zullen het licht nu in de twee-dimensionale ruimte sturen in functie van de golflengte: het ene rooster stuurt het licht vlug in de ene dimensie (hoog orde rooster), terwijl het andere het licht traag in de andere dimensie stuurt (laag orde rooster). Een totaal bereik van 15° × 50° werd opgemeten voor een golflengtebereik van 100 nm.

Als laatste werd ook een retroreflectieve structuur gefabriceerd op SOI. Deze vinden onder andere toepassing als optische markers. Een retroreflectief bereik van 4° × 57° werd opgemeten. Al deze componenten tonen duidelijk het potentieel aan van silicium fotonica voor draadloze optische toepassingen.

English summary

Optical wireless links are rapidly gaining importance. To satisfy the growing demand for bandwidth, different technologies will need to be explored and developed. In the wireless communication world, a bandwidth bottleneck is foreseen in the coming years due to the strict regulations and technological limitations. In the wired world, people have shifted from copper cables to optical fibers to satisfy these increasing bandwidth needs. The same can now be done in the wireless world. Also short to very-short range links can greatly benefit from a wireless optical implementation. Optical interconnects, for example, is a fast growing domain to solve the problem of high-speed interconnects between different parts of an electronic chip as the current speed of electronic chips is at the limits of what copper interconnects are able to handle. The use of free-space optical links can help to tackle this problem.

The applications of optical wireless are, however, not limited to communication but also reach to sensing and spectroscopy applications: monitoring pollution, gas concentrations, measuring air speed, wind profiling. In these applications, an optical radar (LIDAR) is typically used. This is a wireless beam steering component sending out light and analyzing the reflected light. This technique is also used to create high-definition topography maps. All these applications need efficient beam steering.

Optical Phased Arrays

The most straightforward beam steering approach is to use mechanical motion (a movable mirror for example). For very accurate pointing, heavy masses are needed, making this a bulky approach. It furthermore limits the effect in speed and is sensitive to acceleration. Therefore, we have looked into the fabrication of a beam steering component using no mechanical motion.

We have used the Optical Phased Array (OPA) principle. Such an OPA consists of an array of light emitting apertures of which the phase can be tuned. Any desired phase front can then be programmed resulting in not only beam steering applications, but also optical beam shaping. OPAs also play a key role

in adaptive optics applications, i.e., reconstructing the phase front of light traveling through the atmosphere for astronomic imaging or long-haul wireless optical links. Also in biomedical imaging adaptive optics can be used to generate 3D images of biological media.

There are some technological challenges when fabricating OPAs. For large range continuous steering, the element spacing should be smaller than half a wavelength. This condition is very difficult to meet due to the small wavelength of light. Furthermore, large apertures are needed for directive beams. This means we need a large number of elements. Routing issues then also come into play. Therefore, there is usually not a one-type-fit-all solution. To get a large steering range, a cascade of large-angle step steering and small-angle continuous steering is typically used.

Mainstream OPAs are fabricated using liquid crystal (LC) technology. The steering speed and range is, however, limited. In this work, we have investigated the silicon photonics platform to fabricate OPAs.

Silicon Photonics

Photonic integration is currently heavily being researched. Using integration allows us to obtain complex functionality: higher data rates of integrated detectors, lower power consumption, improved sensing, all-optical functionality and reduced cost if mass-production is possible. While there is a multitude of platforms for photonic integration (GaAs, InP, glass or polymer based, Si), the platform of our choice is the silicon photonics platform.

There is a strong rationale behind the silicon photonics platform. Silicon is transparent at the wavelengths heavily used in present-day optical communication systems (1310 nm and 1550 nm), silicon-on-insulator (SOI) has a high index contrast allowing dense integration, low-loss waveguiding has been shown, integration of Ge allows to fabricate integrated detectors. The only missing element is light generation in silicon. The indirect bandgap does not allow efficient light generation. Hybrid integration of other III-V semiconductors can then for example be used. When using silicon, the immense technology development that has happened through the CMOS (Complementary Metal Oxide Semiconductor) industry can be brought to use to fabricate nanoscale photonic structures.

The silicon photonics platform offers us all the needed functionality to fabricate OPAs. Light can be split using, for example, a star coupler (Figure 1(a)), it can be sent off-chip using grating couplers (Figure 1(b)) and its phase can be tuned using integrated phase tuners. As the phase tuning is of key importance for an OPA, this has been investigated in more detail.

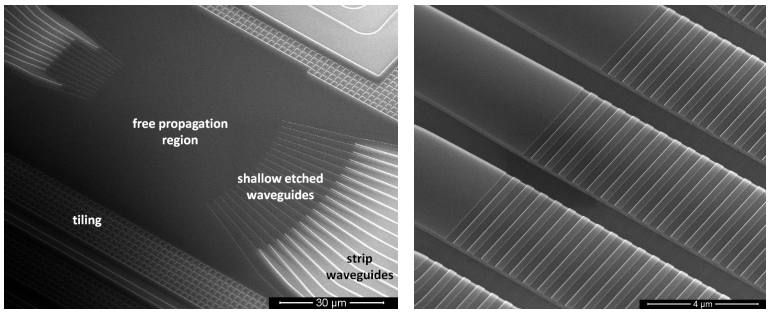

(a) (b)

Figure 1: Scanning electron microscope pictures of integrated components on silicon-on-insulator: (a) star coupler, (b) grating coupler array.

The proof-of-principle components were fabricated using thermo-optic phase tuners, i.e., by heating a waveguide its refractive index changes and thus the phase of the light inside the waveguide is tuned. We have also proposed and demonstrated a novel phase tuning technique using NEMS (Nano-Electro-Mechanical Systems) technology. By applying a voltage over a free-standing slot waveguide, the slot beams are attracted and its effective index changes.

Experimental results

We have successfully fabricated and characterized one-dimensional OPAs on SOI as shown in Figure 2. Using this structure, full continuous steering over $\pm 18°$ was shown using thermo-optic phase tuners. Figure 3 shows the one-dimensional beam profile being steered to an angle of 0°, 6°, 12° or 18°. As we have full control over the one-dimensional phase front, several other applications were investigated. By programming all the phases to mimic a lens, the beam can be focused above the chip. This is especially useful in sensing applications.

When the OPA acts as a receiver, the incoming phase front can be investigated using the integrated phase tuners. Direction-of-arrival measurements were performed allowing us to investigate the direction of incidence of a light beam. This is needed in high-speed wireless link setup, where a beam needs to be pointed to its receiver. We have furthermore looked into the application of coherent combining of scattered light in a single mode waveguide. By applying the right phase to each element, we are able to improve the collection into a single mode waveguide by 10 dB for a 16 element array. This is useful in biological spectroscopy applications.

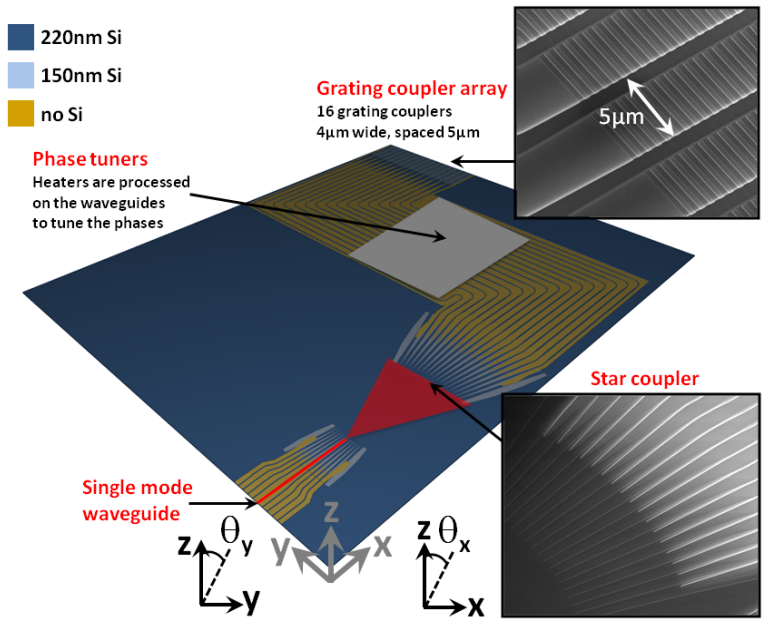

Figure 2: One-dimensional OPA with 16 addressing electrodes: the heaters can be tuned to impose a random phase front.

By placing grating couplers in a two-dimensional configuration, we get a 2D OPA. These OPAs however suffer from large element spacing and low fill-factor due to the needed routing and therefore only have a limited steering efficiency and a lot of higher order lobes. A typical far-field pattern can be found in Figure 4.

When we use a similar layout as shown in Figure 2, but a fixed delay length difference is introduced in the delay lines (instead of the phase tuner region of Figure 2), a two-dimensional dispersive beam steerer is obtained. The delay length difference creates an Arrayed Waveguide Grating (AWG), which typically is a high-order grating, while the out-coupling grating is a low-order grating. These two gratings will shift the beam in the 2D angular space, when the wavelength is changed: the high-order grating quickly steers the light in one dimension, while the low-order grating slowly steers the light in the other dimension. A total coverage range of $15° \times 50°$ is obtained for a 100 nm wavelength shift.

We have also designed and fabricated an optical retroreflector using the silicon photonics platform. Such retroreflectors find applications in for example optical marker applications. Retroreflectivity over a coverage range of $4° \times 57°$ was observed. These structures clearly show the potential of the silicon photonics platform in beam steering and shaping applications.

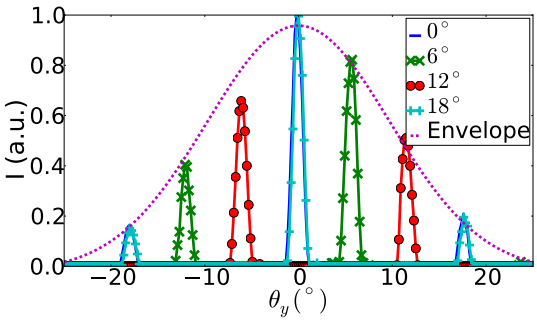

Figure 3: Measured far-field in the θ_y-direction using thermo-optic steering at 1550 nm. The beam is steered to the angles 0°, 6°, 12° and 18°. The dashed line shows the envelope of the far-field pattern.

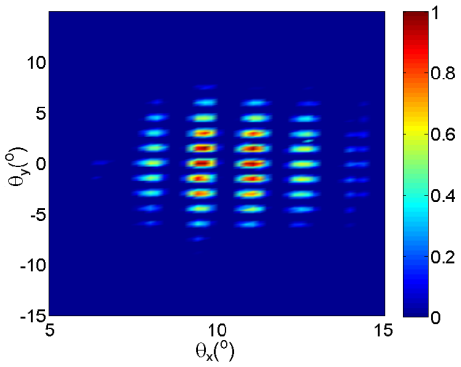

Figure 4: Measured far-field pattern of a 2 × 2 OPA on SOI.

1 Introduction

Bandwidth. It is one of the most important aspects of today's communication systems. People want more, and they want it faster. HD (High-Definition) television, video conferencing, online streaming, Internet file sharing are several of the applications that consume large amounts of bandwidth. The large bandwidth that is needed for all these services today is given to us by the optical communication systems using optical fibers. A large shift to the optical domain has been seen over the last decades for the long haul networks. At the end-user side, however, one typically still uses a copper cable connection to the network. This last mile copper cable technology prevents the network to provide Gbps connections to end users, but as the demand for higher data rates is increasing, network providers will have no other choice in the future than to deliver fiber-to-the-home (FTTH) services.

Now suppose a fiber-optic Gbps connection is reaching your home. There is still the issue to distribute this connection speed across your home. People nowadays are very keen of wireless systems as only a small setup cost is typically needed and large coverage range and mobility is reached. Just think about the popularity of the current WiFi networks. While this technology can deliver great services up to several hundred Mbps, they will prove to be inadequate for Gbps connections. Optical wireless links on the other hands have proven to be able to provide the needed bandwidth. Several technological issues, however, still limit the widespread use of these optical links.

This research work deals with this technological issue to fabricate components capable to setup wireless optical links with beam steering functionality to provide a large coverage range. For this, the integrated silicon photonics technology is investigated that allows us to fabricate nanometer scale structures with advanced functionality that furthermore have the possibility to be integrated in the same platform as your electronic chip. Such an integrated optics approach is the same evolution one has seen in electronics: from very bulky transistor devices with limited functionality to ultra small electronic chips with advanced functionality.

The applications of optical beam steering are not limited to medium or long range data communication links. It can also be used at the very short range, e.g., interconnecting different parts of an electronic integrated circuit at high speed. It furthermore also offers a multitude of applications in several sensing domains. Optical spectroscopy can identify unknown substances, gases, liquids or molecules based on their absorption spectrum. Using optical scanners, a high resolution topography map can be made or three dimensional images of a room can be created. Optical bio-imaging allows us to create biological images using non-invasive and non-harmful radiation. The components used nowadays are typically very bulky and/or expensive. The structures investigated in this work also provide a relevant functionality in some or several of these domains showing the potential of this platform.

Figure 1.1 shows a schematic view of a photonic-electronic chip using off-chip beam steering for interconnecting, sensing, scanning or data communication. Generation, detection, filtering can all happen on-chip using the integrated photonics platform, while electronics can offer the drivers and post-processing functionality. This research work deals with the elements coupling light off-chip with beam steering and/or shaping functionality.

1.1 Rationale and Goal

The rationale of this work can be summarized as investigating the use of the silicon photonics platform in optical wireless and beam steering applications. What can silicon photonics offer us here? While this is a very broad description of the work, it will become clear that the focus lies on certain aspects, mainly beam steering.

The goal of this work is not basic component research where one optimizes e.g., waveguide losses, design of splitting components, interfacing between optical fibers and photonic integrated circuits. Here, we take it one step further. The research and know-how from the last years on component design, fabrication and integration is put to use to fabricate more complex functionality. Basic building blocks are used such as waveguides, splitters, star couplers and grating

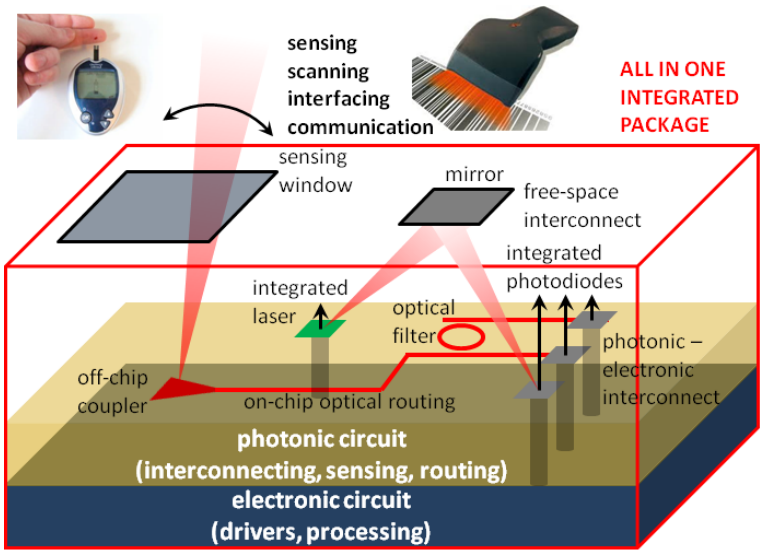

Figure 1.1: Schematic view of a photonic-electronic integrated chip with off-chip beam steering functionality.

couplers. While the structures still remain relatively simple, it clearly shows the importance of design tools, libraries of standard building blocks and the possibilities of silicon photonics in the integration of many components. Using this approach, we are able to demonstrate complex functionality on a complex technology platform using a relatively straightforward approach.

Apart from the (passive) basic building blocks, phase tuning is an essential active function needed for the beam steering approach. Therefore we need to investigate phase tuning techniques in silicon photonics. Firstly, in-house technology is used and optimized to achieve this functionality, namely integration of thermo-optic phase tuners. While the thermo-optic effect has been studied for several years in our research group to tune a ring for example, we will take this one step further by fabricating a multitude of phase tuners that can be driven simultaneously. A dedicated electrical probing setup is therefore developed. We also look into another novel type of phase tuning based on Nano-Electro-Mechanical Systems (NEMS).

Finally, both the passive building blocks and active functionality are brought together to fabricate the beam steering elements as shown schematically in Figure 1.2. These beam steering structures will split a light beam into multiple beams. The different beams will then go through active phase control drivers so the phase can be controlled between all the elements. After this phase control section, light is sent off-chip using grating couplers. In this way, the phase

front of the light beam which is coupled off-chip can be controlled and can thus be steered in any wanted direction. This is a so-called optical phased array. The phase can also be indirectly controlled by introducing delay lines in the phase control section and using the wavelength to steer the beam. The components can furthermore act as a receiver where the off-chip coupling section will then couple light on-chip and the phase controllers will make sure all the contributions will add up in the splitting section (which then acts as a combiner) into the input waveguide, which then of course acts as an output waveguide. A dedicated measurement setup is also built to characterize this type of components.

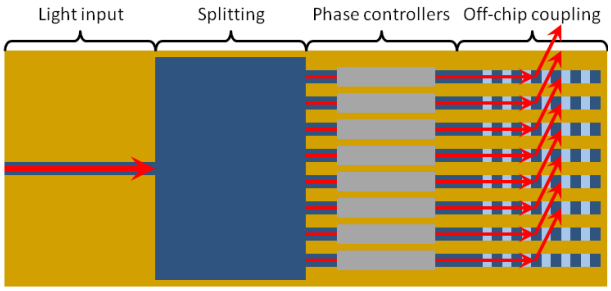

Figure 1.2: Schematic view of the beam steering elements.

1.2 Outline

The next chapter deals with wireless optical communication, one of the main drivers that started this work. As the goal is to fabricate components using the silicon photonics platform that are able to setup wireless links, one must look into the advantages and disadvantages of wireless optical versus radio links. Chapter 2 deals with this in some detail giving a comparison between the optical and radio links, the different possibilities to setup optical wireless links and some of the latest results in wireless optical communication links.

Chapter 3 deals with Optical Phased Arrays (OPAs). These are the main components under investigation to allow optical beam steering using a non-mechanical approach. First, the theory of phased arrays is reviewed. Then we look into some technological implementations, where we also briefly go over some other steering approaches. Finally some of the main applications of these OPA-based beam steering components are given.

In Chapter 4, a brief summary of the silicon photonics platform is given. This is the platform of our choice and is used for the fabrication of our components. The chapter is only meant as a short introduction to the technology platform and the different components that have been used.

Optical phase tuning is presented in Chapter 5. OPA technology needs two main components: radiating elements and phase tuners. While the radiating elements fabricated on the silicon photonics platform are discussed in Chapter 4, Chapter 5 discusses the possibilities to fabricate phase tuners. A very straightforward approach using the thermo-optic effect in silicon is first investigated. Afterward a novel type of phase modulation based on Nano-Electro-Mechanical systems (NEMS) is presented. The chapter concludes with a small summary of some other common phase tuning or modulation techniques in silicon.

After introducing the key ingredients of OPA technology in Chapters 3, 4 and 5, the fabricated structures are presented in Chapter 6. It starts with an overview of the measurement setup and then deals with the different beam steering structures that have been fabricated: one- and two-dimensional OPAs, dispersive beam scanners and also a retroreflector design.

Chapter 7 finally deals with the main conclusions and future perspectives.

1.3 Own Contributions

The work presented here depends heavily on the research knowledge of the Photonics Research Group where this work was done. The basic building blocks of the silicon photonics platform discussed in Chapter 4 were already developed and ready to use for this research under the form of basic building block libraries.

The thermo-optic phase tuners discussed in Chapter 5 were developed by dr. Katarzyna Komorowska. During this research, this technology was further developed by the author in collaboration with dr. Katarzyna Komorowska to suit the needs of OPA technology. Resistivity and efficiency characterizations were done to correctly design the heaters used in the OPA designs. The NEMS phase tuners were designed and fabricated by dr. ir. Joris Roels, a former PhD student. In this work, the under-etch process for these NEMS phase tuners was developed and the characterization measurements were performed.

The first proof-of-principle one-dimensional OPA discussed in Section 6.2.1 was designed by prof. Wim Bogaerts and characterized with the help of prof. Nicolas Le Thomas from l'École Polytechnique Fédérale de Lausanne, Switzerland where the author has spent a two week exchange. Afterward, a simplified version of this Fourier imaging setup was built by the author for the characterization of future OPA structures. This setup was then further extended with motorized movement and electrical probing functionality by the author. The author also played a large role in developing a software measurement platform based on the Python scripting language to write the custom measurement scripts needed for the experiments.

The next OPA structures (1D OPA with multiple electrode, 2D OPAs, dispersive beam scanners and retroreflectors) were all designed, post-processed and characterized by the author. The design made use of the basic building blocks which were integrated in a more complex design with the Python based design software developed by prof. Wim Bogaerts. The retroreflectors were designed in collaboration with the group of prof. Dominic O'Brien from Oxford University. The fabrication and measurements were, however, done by the author.

The main contribution of the author thus consisted in bringing together and optimizing the different basic building blocks to fabricate more complex OPA structures to allow beam steering using an integrated platform and developing the needed hardware and software for the characterization of these structures.

1.4 Publications

Publications in international journals

1. K. Van Acoleyen, J. Roels, P. Mechet, T. Claes, D. Van Thourhout and R. Baets. *Ultra-compact phase modulator based on a cascade of NEMS-operated slot waveguides fabricated in Silicon-On-Insulator.* IEEE Photonics Journal, 4(3):779–788, May 2012.

2. K. Van Acoleyen, E. Ryckeboer, W. Bogaerts and R. Baets. *Efficient Light Collection and Direction-Of-Arrival Estimation using a Photonic Integrated Circuit.* IEEE Photonics Technoloy Letter, 24(11):933–935, March 2012.

3. K. Van Acoleyen, K. Komorowska, W. Bogaerts and R. Baets. *One-dimensional off-chip beam steering and shaping using optical phased arrays on silicon-on-insulator.* IEEE/OSA Journal of Lightwave Technology, 29(23):3500–3505, October 2011.

4. K. Van Acoleyen, D.C. O'Brien, F. Payne, W. Bogaerts and R. Baets. *Optical Retroreflective Marker Fabricated on Silicon-On-Insulator.* IEEE Photonics Journal, 3(5):789–798 , August 2011.

5. K. Van Acoleyen, W. Bogaerts and R. Baets. *Two-dimensional Dispersive Off-chip Beam Scanner Fabricated on Silicon-On-Insulator.* IEEE Photonics Technology Letters, 23(17):1270–1272 , June 2011.

6. K. Van Acoleyen, H. Rogier and R. Baets. *Two-dimensional Optical Phased Array Antenna on Silicon-On-Insulator.* Optics Express, 23(17):13655–13660 , June 2010.

7. K. Van Acoleyen, W. Bogaerts, J. Jágerská, N. Le Thomas, R. Houdré and R. Baets. *Off-chip beam steering with a one-dimensional optical phased array on silicon-on-insulator.* Optics Letters, 34(9):1477–1479 , April 2009.

Publications in international conferences

1. K. Van Acoleyen, W. Bogaerts and R. Baets. *Integrated optical beam steerers.* Optical Fiber Communication Conference and Exposition (OFC) / National Fiber Optic Engineers Conference (NFOEC) 2013, Anaheim, California, USA, March 2013 (invited).

2. K. Van Acoleyen, K. Komorowska, W. Bogaerts and R. Baets. *Off-chip beam steering using optical phased arrays on silicon-on-insulator.* In 16th Annual Symposium of the IEEE Photonics Benelux Chapter, page 133–136, Ghent, Belgium, December 2012.

3. K. Van Acoleyen, E.M.P. Ryckeboer, K. Komorowska and R. Baets. *Light collection from scattering media in a silicon photonics integrated circuit.* IEEE Photonics 2011 (IPC11), page 543–544, Arlington, VA, USA, October 2011.

4. K. Van Acoleyen, J. Roels, T. Claes, D. Van Thourhout and R. Baets. *NEMS-based optical phase modulator fabricated on Silicon-On-Insulator.* In 8th International Conference on Group IV Photonics, pages 371–373 (FC6), London, United Kindom, September 2011.

5. K. Van Acoleyen and R. Baets. *Compact lens-assisted focusing tapers fabricated on Silicon-On-Insulator.* In 8th International Conference on Group IV Photonics, pages 157–159 (ThA2), London, United Kindom, September 2011.

6. H. Nikkhah, K. Van Acoleyen and R. Baets. *Optical Phased Arrays in Silicon on Insulator for Optical Wireless Systems.* In International Symposium on Green Radio over Fiber & All Optical technologies for Wireless Access Networks (GROWAN 2011), page P5, Brest, France, June 2011.

7. K. Van Acoleyen, W. Bogaerts, H. Rogier and R. Baets. *Two-dimensional Dispersive Beam Steerer Fabricated on Silicon-On-Insulator.* In 7th International Conference on Group IV Photonics, page P2.7, Beijing, China, September 2010.

8. K. Van Acoleyen, H. Rogier and R. Baets. *Chip-to-chip Optical Wireless Link Feasibility Using Optical Phased Arrays on Silicon-On-Insulator.* In 7th International Conference on Group IV Photonics, page FC7, Beijing, China, September 2010.

9. D. Vermeulen, K. Van Acoleyen, S. Ghosh, S. Selvaraja, W.A.D. De Cort, N.A Yebo, E. Hallynck, K. De Vos, P.P.P. Debackere, P. Dumon, W. Bogaerts, G. Roelkens, D. Van Thourhout and R. Baets. *Efficient Tapering to the Fundamental Quasi-TM Mode in Asymmetrical Waveguides*. In European Conference on Integrated Optics (ECIO2010), page WeP16, Cambridge, United Kingdom, April 2010.

10. K. Van Acoleyen, H. Rogier and R. Baets. *Optical wireless communication using Silicon-on-Insulator technology*. In 14th Annual Symposium of the IEEE Photonics Benelux Chapter, page 33–36, Brussels, Belgium, November 2009.

11. K. Van Acoleyen, H. Rogier and R. Baets. *Feasibility Study of Integrated Optical Phased Arrays for Indoor Gb/s Wireless Optical Links*. In 35th European Conference on Optical Communications (ECOC 2009), page P4.18, Vienna, Austria, September 2009.

12. K. Van Acoleyen. *Optical beam steering for wireless optical applications*. In 5th Optoelectronic and Photonic Winter School: CMOS Photonics, Trento, Italy, March 2009.

Publications in national conferences

1. K. Van Acoleyen and R. Baets. *Optical beam steering for wireless optical applications*. In 12th FEA PhD Symposium, page 99, Ghent, Belgium, December 2011.

2. K. Van Acoleyen, H. Rogier and R. Baets. *Wireless Optical Communication using Silicon-on-Insulator technology*. In 10th UGent-FirW PhD Symposium, pages 298-299, Ghent, Belgium, December 2009.

2

Optical Wireless Communication

"In the future, equipping rooms with 'optical wireless hotspots' that enable fast free-space data transmission to laptops or mobile phones by means of light beams rather than radio waves, could dramatically boost the speed of wireless communication." (Dominic O'Brien et. al. [1]).

Wireless communication is becoming increasingly important in our current society. One can think of the exponential growth of wireless devices reaching from mobile phones to the emergence of WiFi networks in almost every living room. These networks are currently stretched to their limits to allow the ever increasing data rates. It is predicted that by 2017 wireless radio communication will no longer suffice for this increasing bandwidth need [2]. In the wired world, the problem has been solved by moving from copper cable to the optical fiber because of the extremely large bandwidth available in the optical domain. While at first only long haul links were replaced, this trend continues with fiber-to-the-cabinet (FTTC) and eventually fiber-to-the-home (FTTH) to allow high data rates to the end user.

To keep up with the increasing speed of the wired connections, one also needs to boost the speed of wireless connections and a similar trend of going to the optical domain can be seen. There are many trade-offs that need to be considered when choosing between an optical or a radio link as will become clear in this chapter. The chapter is mainly meant to familiarize the reader with

the growing importance of wireless optical communication. The rest of the research work will focus on the technological component implementation of certain beam steering components that can have a large influence in the wireless communication domain, but we do not specifically deal with the communication aspects of setting up a real link.

In Section 2.1, a comparison of wireless optical versus radio communication is given where focus lies on the different properties of both communication channels. Next, the different types of wireless optical links will be discussed in Section 2.2. Section 2.3 discusses the current state-of-the-art. A conclusion is formulated in Section 2.4.

2.1 Optical versus Radio Frequency

Optical and RF (Radio Frequency) waves are both electromagnetic (EM) waves. Due to the huge difference in carrier frequency, several hundreds of THz for optical compared to kHz to a few tens of GHz for radio signals, they both have very different characteristics and technological implementations [3].

2.1.1 Bandwidth

The most important difference between optical and radio waves is the available bandwidth. Not only does bandwidth increase with higher carrier frequency, the optical domain is furthermore free from FCC (Federal Communications Commission) regulations, opening up several THz of bandwidth. For radio waves, the frequency spectrum is strictly regulated.

Most of the current widespread wireless applications such as WiFi and bluetooth work in the ISM (Industrial, Scientific and Medical) bands. Although designed to be used in non-communication applications, they are heavily used for wireless communication as they are unlicensed. The most commonly used ISM band is the 2.45 GHz ±50 MHz band with 100 MHz bandwidth. Due to the heavy use this band is getting highly congested.

To keep up with the increasing bandwidth need, complicated modulation schemes or multiple antennas (MIMO, Multiple-Input Multiple-Output) are used. Another option is to shift to the 60 GHz ISM band, were 5-7 GHz of unlicensed bandwidth is available worldwide. This band is mainly intended for short range, high speed communication such as HD video [4, 5].

Light on the other hand has a huge unlicensed bandwidth. For wired optical links, this bandwidth is being exploited heavily. There are two main factors that need to be taken into account when looking at a present-day wireless optical link, especially at the receiver side:

- The noise power depends linearly on the bandwidth and a high bandwidth will therefore require a high received power.
- The bandwidth is limited by the area of the photodiode. Large area photodiodes have a high capacitance resulting in a large RC constant and thus a limited bandwidth.

The noise power limitation is discussed in Section 2.1.6. For a photodiode the bandwidth is limited by the RC constant of the receiver and the transit time of the carriers. The maximum bandwidth is given by

$$\Delta f = \frac{1}{2\pi(\tau_{tr} + \tau_{RC})}, \tag{2.1}$$

with τ_{tr} the transit time of carriers, which is equal to the depletion width of the photo detector ($W_d \sim 5\mu m$) divided by the drift velocity of the carrier ($v_d \sim 10^5 m/s$). The capacitance is simply modeled as

$$C = \epsilon \frac{A_{PD}}{W_d}, \tag{2.2}$$

with ϵ the dielectric constant and A_{PD} the area of the photodiode. When the area of the photodiode is known, its capacitance can be calculated by (2.2) and the maximal resistance for a certain bandwidth follows from (2.1). A large photodiode will thus result in a large received power which is needed for high speed links, but at the same time, the bandwidth is limited due to the diode capacitance. The problem can be solved by using concentrators although these limit the field-of-view (FOV) as discussed below. The capacitance seen by the circuit can be decreased by using a so-called bootstrapped transimpedance amplifier, which reduces the effective capacitance seen by the electrical circuit [6].

2.1.2 Field-of-view and antenna size

For an RF antenna, the FOV is determined by the antenna size. As a rule of thumb, the FOV of an antenna can be approximated by [7]:

$$\text{FOV} \propto \frac{\lambda}{D}, \tag{2.3}$$

with λ the wavelength and D the size of the antenna. This is true for any type of EM radiation and the same rule of thumb holds for the optical case. This shows the advantage of using optics for directive links: the 'antennas' can be kept small to get directive links due to the small wavelength of light.

When using optical concentrators, the FOV is reduced while the effective detection area is increased. The maximum concentration ratio C (ratio of the

power collected with concentrator to the power collected without concentrator) is given by [6]:

$$C = 0.82\left(\frac{n}{\sin\phi}\right)^2, \tag{2.4}$$

with n the refractive index of the concentrator and ϕ the acceptance half-angle (where $\phi < 65°$). A small FOV thus allows a very large concentration ratio. Different types of concentrators exist with a trade-off between concentration ratio and FOV [3]. Another method of increasing the FOV is by using an imaging receiver. In this type of concentrator, every direction of incidence is focused onto a different spot in a detector array. This system has been demonstrated using an integrated CMOS detector array in [8], which is discussed further in Sections 2.2.5 and 2.3.

2.1.3 Security and Interference

RF signals, at the lower frequency range (up to several GHz), can easily penetrate walls. This has spurred their widespread use in WiFi applications. Due to their penetration, it is, however, a less secure medium as an eavesdropper can easily pick up the signal. Light on the other hand does not penetrate through walls and is therefore a secure alternative. When one tries to pick in on the optical signal of a directive link, the receiver will immediately notice a large decrease in transmission. When using an RF link with a high carrier frequency such as the 60 GHz band, the link also starts to have optical characteristics such as being directive and unable to efficiently penetrate objects or walls.

Furthermore, optical links do not suffer from EM interference and can be used in areas where extra EM radiation is not desired such as in hospitals or airplanes.

2.1.4 Generation, Modulation and Detection

A large difference between both technologies are the elements used to emit or receive the signals. For RF signals, metal antennas are typically used for generation and detection of the signals. These antennas directly measure the electric field which is then down-converted to measure the data signal imposed on the carrier. As the measured power depends linearly on the EM power, this is a very sensitive approach. The limitation is mainly due to other users or devices working in the same frequency band. This technique allows complicated modulation formats such as OFDM (Orthogonal Frequency Division Multiplexing), where the data is modulated onto several subcarriers using BPSK (Binary Phase Shift Keying), QPSK (Quadrature Phase Shift Keying) or QAM (Quadrature Amplitude Modulation) to reach high spectral efficiency.

Optical signals are typically generated and received by two different components. Light generation happens with LEDs (Light Emitting Diodes) or lasers while a photodiode typically receives the light. The latter is a quantum detector: it measures the photons impinging on the receiver. Such a quantum detector is a quadratic detector, i.e., not electric field but field intensity is measured: the photodiode converts an impinging optical power to an electrical current, which are related by the photodiode responsivity. The photodiode is also typically several hundreds of wavelengths in extent. This results in the fact that optical links do not suffer from fading (destructive interference of multiple reflections of the same signal). The quadratic detection has an interesting implication. When the path losses increase with 3 dB, the SNR (Signal-to-Noise Ratio) will degrade by 6 dB, meaning that high path losses can not be tolerated. However, the same holds for the transmit power: increasing the power by 3 dB will improve the SNR by 6 dB. This means that a degradation of the SNR by 3 dB only needs to be compensated by a 1.5 dB increase of transmit power. Practical limitations such as noise and limited transmit power put a limit on this effect [9].

As intensity is measured, a typical optical link uses IM/DD (Intensity Modulation / Direct Detection), using either simple OOK (On-Off Keying) or PPM (Pulse Position Modulation). More complicated modulation such as using different subcarriers imposed on the optical signal (optical OFDM) can be used, but these are typically not much more power efficient [3]. For high data rates, however, optical OFDM can be used to combat inter-symbol-interference [10]. Multi-wavelength modulation is another option when using optical links, i.e., using different wavelengths for different signals. This is the same as Wavelength Division Multiplexing (WDM) [11].

2.1.5 Power limitations

Not only the frequency bands but also the allowed power transmission in the radio spectrum is regulated by the FCC and/or national law, mainly to reduce interference and because of possible health risks. The limit is given in EIRP (Equivalent Isotropically Radiated Power) but also depends on the maximum antenna gain (how much the antenna radiates in a certain direction compared to an isotropic radiator) that is allowed. For antennas with less than 6 dB directivity, the allowed EIRP for wireless LANs (Local Area Networks) is 1 W.

In the optical case, there are certain eye and skin safety limitations which need to be taken into account and limit the maximum emitted power that is allowed. Lasers are divided into four different classes:

- Class I: no hazard at any wavelength or exposure time.
- Class II: blink response of the eye ($\approx$0.25 s) can protect the eye from damage. This class is only valid for visible wavelengths. When the natural

protection mechanism of the eye fails, damage to the eye can occur.

- Class III: not hazardous to the skin, but dangerous for the eye; damage can occur in less than the blink time of the eye.
- Class IV: hazardous to the eye and skin, specular reflection can also cause damage.

Table 2.1 gives the ANSI (American National Standards Institute) standards classification for the four different classes of continuous-wave lasers. Note that the use of the 1550 nm wavelength allows a much higher laser power to be emitted, as the cornea is not transparent anymore in this region.

Wavelength Range (nm)	Class I	Class II	Class III	Class IV
200-400	$<0.8\times10^{-9}$ W $<8\times10^{-6}$ W wav. depend.	N/A	<0.5 W wav. depend.	>0.5 W
400-550	$<0.4\times10^{-6}$ W	$<1\times10^{-3}$W	<0.5 W	>0.5 W
500-1060	$<0.4\times10^{-6}$ W $<200\times10^{-6}$ W wav. depend.	N/A	<0.5 W wav. depend.	>0.5 W
1060-1400	$<200\times10^{-6}$ W		<0.5 W	>0.5 W
>1400	$<0.8\times10^{-3}$ W		<0.5 W	>0.5 W

Table 2.1: Classification of eye-safety power limits for continuous-wave lasers [12].

These limitations are very restrictive since it is assumed that the laser light can shine directly on the retina. When taking into account the actual size of the source, the so-called Accessible Emission Limit (AEL) can be given which is a function of viewing time, wavelength and size of the optical source. Using the IEC (International Electrotechnical Commission) standard, a maximum allowed transmit power for a point source emitter of 8.8 mW and 10 mW is given at a wavelength of 1310 nm and 1550 nm, respectively. [6, 13].

2.1.6 Noise

In a radio link, the noise power P_n can be calculated using an equivalent temperature T_{eq} as:

$$P_n = kT_{eq}\Delta f F, \tag{2.5}$$

with k_B Boltzmann's constant, Δf the bandwidth and F the noise figure. For widespread wireless LANs in the ISM bands, the main noise is, however, coming from interference of other users or devices. For a 60 GHz link, which works

directive and short range, this interference of other users is limited and the noise power becomes less than -70 dBm [14].

In a wireless optical link, the receiver converts an impinging optical power into a photocurrent (and not into an electrical power as for the RF case). There are two main noise contributions on this photocurrent: shot noise and thermal noise. Shot noise due to ambient light has been recognized as the limiting factor for low data rate links, while in the absence of ambient light or at higher data rates (>Gbps) the thermal noise of the preamplifier becomes more important [15, 16].

Thermal noise

Thermal noise depends on the effective noise bandwidth Δf and load resistance R_L. The thermal noise variance is given by

$$\sigma_{th}^2 =< i_{th}^2 >= \frac{4k_B T}{R_L}\Delta f, \tag{2.6}$$

with k_B Boltzmann's constant and T the noise temperature. The noise is dependent on the load resistance. While this resistance should be high to get low thermal noise, a high R_L will result in a large RC constant and thus a low usable bandwidth.

Shot noise

The shot noise variance is given by

$$\sigma_s^2 =< i_s^2 >= 2q(I_s + I_d + I_a)\Delta f, \tag{2.7}$$

with q the elementary charge, I_s the signal current, I_d the dark current and I_a the ambient light current. The ambient light is considered to be sunlight. For example, the light irradiated by the sun in the 1000 nm–1700 nm range is equal to P_{AL}=285 W/m^2 [17]. The ambient light power P_{AL} is usually the limiting noise factor giving:

$$\sigma_s^2 = 2qRP_{AL}A_{capt}\Delta f, \tag{2.8}$$

with A_{capt} the effective area that captures the light and R the responsivity of the photodetector. The influence of different ambient light source on optical links is discussed in [18]. By using a filter that blocks all the light apart from the signal band, the shot noise can be greatly reduced.

2.1.7 Optical and RF

From the discussion above, it is clear that neither optical nor RF can suit all our needs. Optics can work very directive but only limited power can be emitted compared to RF links at 2.45 GHz (mW-range for optical, W-range for RF).

The inherent difference between RF antennas and photodiodes results in the fact the receiver sensitivity of RF receivers is few order of magnitude better than for the optical case (μW-level for optical, nW-level for RF). Therefore, the main added value of optical links lies in very directive, high bandwidth links. When the links are not directive, the path loss quickly becomes too high to allow large data rates. An example of such a typical link budget using our fabricated components is given in Section 6.2.3.

The future vision of a Home Area Network (HAN) lies in the combination of both technologies. RF technology can be used to ensure connectivity in the network, while optical links can be setup for high speed data rates when needed. If the link is blocked, there will be the back-up RF network. This vision is displayed schematically in Figure 2.1. The next generation of 4G networks will probably use both optical and RF technologies to keep up with the increasing data rates [16].

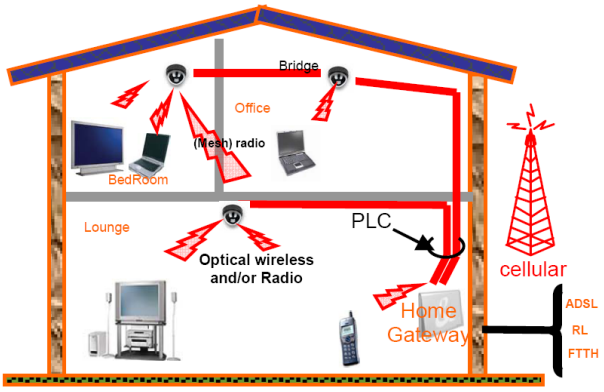

Figure 2.1: Future vision of a Home Area Network [15].

2.2 Optical link schemes

There exist different optical link schemes for both transmitter and receiver. They can be classified in directive and non-directive links, diffuse or line-of-sight (LOS) links or hybrid links. The most important types are discussed below.

2.2.1 Directive versus non-directive

First of all, a distinction needs to be made between directive or non-directive links. In a directive link, there is a narrow FOV at both the transmitter and receiver side. Therefore, there is a high need for beam steering. A non-directive

link has a wide FOV at both transmitter and receiver. These links requires no or limited steering but suffer from inter-symbol-interference due to multipath propagation. In a hybrid link, one of the transceivers is directive, while the other remains non-directive so only steering at one side is needed.

2.2.2 Diffuse link

In a diffuse optical link, there is no need for a direct path between transmitter and receiver. The link relies on diffusely reflected light. The probability of blocking is very low, but the path loss is high. Furthermore, due to multipath propagation, i.e., different reflections of the same signal, the speed is typically limited to 10 Mbps. Equalization techniques are required to improve the data rates.

2.2.3 LOS link

These links can achieve very high data rates, especially in the directive case. One can think of wireless optical telescopic links (for example between buildings) that are used as last-mile high speed connections. Directive links are prone to blocking as there is only one single path between transmitter and receiver. To ensure connectivity multiple directive links are needed. Short blocking of the signal might not be detrimental as very high data rates can be sent when the link is not blocked. A backup network is then useful (like an RF network) to ensure connectivity.

2.2.4 Multispot diffuse link

A multispot diffuse link tries to combine the advantages of diffuse and LOS links. To combat the multipath propagation, light is sent across several directive beams to either directly hit the receiver or to diffusely reflect on for example the ceiling before reaching the receiver. This also increases user mobility while keeping the probability of complete blocking low. Special angle and power adaptation algorithms can then be used to improve the SNR from transmitter to receiver showing feasible links of 2.5 Gbps [19, 20].

2.2.5 Transmitter and receiver configurations

The optical transmitter or receiver has to be carefully designed depending on the link. A simple transmitter with certain FOV can be used or an array can be made to transmit light in different directions. Using optics, their FOV can be changed to the link needs.

There are also different receiver configurations as shown in Figure 2.2. The direct receiver is the most simple configuration, but will receive a lot of ambient light noise. Both the non-imaging and imaging receivers split up the light coming from different angles to different photodiodes. In this way, a lot of noise can be canceled and special adaptation algorithms can be used to improve reception. A trade-off needs to be made between bandwidth, sensitivity and noise [21].

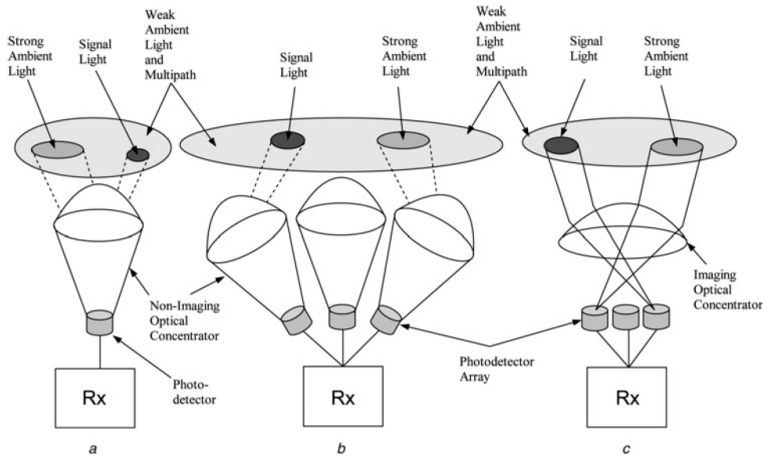

Figure 2.2: Receiver configurations: (a) single receiver, (b) angle diversity receiver, (c) imaging angle diversity receiver [21].

2.3 State-of-the-art

The first optical link was proposed by Gfeller [22]. A diffuse optical link working at 125 kbps at a 950 nm wavelength was shown with a feasibility of links up to 1 Mbps. Nowadays, commercial links are available working at 10 Mbps while in research they reach up to 100 Mbps.

There has been quite some progress in the development of high speed wireless links for indoor communication using optical links in the last few years. The FP7 (European Framework Program 7) project Omega [23] (2008-2010) had the goal to develop technologies for Gbps indoor wireless links using power-lines, WiFi, 60 GHz links and also using visible and infrared light communication. All these technologies of course need special protocols to work together for which an Inter-MAC (Media Access Control) is needed, which was developed in the project. In [24], a 230 Mbps link was shown using white (phosphorent) LEDs used for lighting purposes and an avalanche photodiode (APD). After optimiza-

tion, a link of 513 Mbps was shown in [25].

In [26] a tracking optical link is demonstrated. The transmitter consists of a hexagonal array of 7 resonant cavity LEDs (RCLEDs) and an imaging receiver with 7 photodiodes. The CMOS circuitry is integrated with the photodiodes making the receiver very compact. 100 Mbps data rates were shown.

In [27], a 1.25 Gbps LOS link was shown using an angle diversity technique. The transmitter module consisted of an visible 850 nm laser. By using three lasers and a diffuser to spread out the light, the FOV was 25° × 8°. The receiver was an APD with collimation optics and ambient light filter. In [28], an integrated pin photodiode was fabricated using BiCMOS technology capable of working at 1.25 Gbps for a link of 3.2 m, showing the potential of integrated receiver modules.

2.4 Conclusions

Optical wireless communication is now being widely recognized as a complementary technology to RF to offer Gbps indoor wireless links. Diffuse light radiation or an RF backbone network can ensure network connectivity, while directive LOS links can establish Gbps links for fast data transfer when the path is not blocked. The used link scheme and technological implementation depend on the specific application in mind. Using CMOS integration compact modules can be fabricated at relatively low-cost which can assist our need for high data rates in future home or office networks. One of the key functionalities to allow these directive links is beam steering, which is dealt with in more detail in Chapter 3.

References

[1] Dominic O'Brien, Gareth Parry, and Paul Stavrinou. *Optical hotspots speed up wireless communication.* Nature Photonics, 1:245–247, 2007.

[2] Tom Jeltes. *The connecting thread is about to be disconnected.* Cursor, Eindhoven University of Technology, November 3:5, 2011.

[3] J. M. Kahn and J. R. Barry. *Wireless infrared communications.* Proceedings of the IEEE, 85(2):265–298, 1997.

[4] P. Smulders. *Exploiting the 60 GHz band for local wireless multimedia access: Prospects and future directions.* IEEE Communications Magazine, 40(1):140–147, 2002.

[5] S. K. Yong and C. C. Chong. *An overview of multigigabit wireless through millimeter wave technology: Potentials and technical challenges.* Eurasip Journal on Wireless Communications and Networking, page 10, 2007.

[6] A. M. Street, P. N. Stavrinou, D. C. O'Brien, and D. J. Edwards. *Indoor optical wireless systems - A review.* Optical and Quantum Electronics, 29(3):349–378, 1997.

[7] M. I. Skolnik. *Introduction to Radar Systems.* McGraw-Hill, 1962.

[8] D. C. O'Brien, G. E. Faulkner, K. Jim, E. B. Zyambo, D. J. Edwards, M. Whitehead, P. Stavrinou, G. Parry, J. Bellon, M. J. Sibley, V. A. Lalithambika, V. M. Joyner, R. J. Samsudin, D. M. Holburn, and R. J. Mears. *High-speed integrated transceivers for optical wireless.* IEEE Communications Magazine, 41(3):58–62, 2003.

[9] M. Wolf and D. Kress. *Short-range wireless infrared transmission: The link budget compared to RF.* IEEE Wireless Communications, 10(2):8–14, 2003.

[10] Mohamed E. Khedr, Moustafa H. Aly, and Mohamed E. Tamazin. *Optical Orthogonal Frequency Division Multiplexing For High Speed Wireless Optical Communications.* In 5th IFIP International Conference on Wireless and Optical Communications Networks, 2008 (WOCN '08), pages 1–5, Surabaya, 2008.

[11] J. R. Barry, J. M. Kahn, E. A. Lee, and D. G. Messerschmitt. *High-Speed Nondirective Optical Communication for Wireless Networks.* IEEE Network Magazine, 1991.

[12] L. Matthews and G. Garcia. *Laser and Eye Safety in the Laboratory.* IEEE Press, 1995.

[13] Heatley D. J. T., D. R. Wisely, I. Neild, and P. Cochrane. *Optical wireless: The story so far.* IEEE Communications Magazine, 36(12):72–82, 1998.

[14] P. Smulders, H. Yang, and I. Akkermans. *On the design of low-cost 60-GHz radios for multigigabit-per-second transmission over short distances.* IEEE Communications Magazine, 45(12):44–51, 2007.

[15] K. D. Langer, J. Grubor, O. Bouchet, M. El Tabach, J. W. Walewski, S. Randel, M. Franke, S. Nerreter, D. C. O'Brien, G. E. Faulkner, L. Neokosmidis, G. Ntogari, and M. Wolf. *Optical wireless communications for broadband access in home area networks.* In Marciniak, M., editor, 10th International Conference on Transparent Optical Networks, pages 149–154, Athens, Greece, 2008.

[16] A. Paraskevopoulos, J. Vucic, S. H. Voss, R. Swoboda, and K. D. Langer. *Optical Wireless Communication Systems in the Mb/s to Gb/s Range, Suitable for Industrial Applications.* IEEE/ASME Transaction on Mechatronics, 15(4):541–547, 2010.

[17] Gueymard C. A. *The sun's total and spectral irradiance for solar energy applications and solar radiation models.* Solar Energy, 76(4):423–453, 2004.

[18] A. C. Boucouvalas. *Indoor ambient light noise and its effect on wireless optical links.* IEE Proceedings-Optoelectronics, 143(6):334–338, 1996.

[19] F. E. Alsaadi, M. Nikkar, and J. M. H. Elmirghani. *Adaptive Mobile Optical Wireless Systems Employing a Beam Clustering Method, Diversity Detection, and Relay Nodes.* IEEE Transactions on Communications, 58(3):869–879, 2010.

[20] F. E. Alsaadi and J. M. H. Elmirghani. *Multibeam 2.5 Gbit/s Mobile Optical Wireless Systems Employing Beam Power and Angle Adaptation Method.* In Communications (ICC), 2010 IEEE International Conference on, pages 1–6, Cape Town, South Africa, 2010.

[21] R. J. Green, H. Joshi, M. D. Higgins, and M. S. Leeson. *Recent developments in indoor optical wireless systems.* IET Communications, 2(1):3–10, 2008.

[22] Gfeller F. R. and U. Bapst. *Wireless In-House Data Communication via Diffuse Infrared Radiation.* Proceedings of the IEEE, 67(11):1474–1486, 1979.

[23] Seventh Research Framework Programme (FP7). *OMEGA.* http://www.ict-omega.eu/, 2008-2010.

[24] J. Vucic, C. Kottke, Nerreter S., K. Habel, A. Buttner, K. D. Langer, and J. W. Walewski. *230 Mbit/s via a wireless visible-light link based on OOK modulation of phosphorescent white LEDs.* In Optical Fiber Communication (OFC), collocated National Fiber Optic Engineers Conference, 2010 Conference on (OFC/NFOEC), pages 1–3, San Diego, CA, 2010.

[25] Jelena Vucic, Christoph Kottke, Stefan Nerreter, Klaus-Dieter Langer, and Joachim W. Walewski. *513 Mbit/s Visible Light Communications Link Based on DMT-Modulation of a White LED.* Journal of Lightwave Technology, 28(24):3512–3518, 2010.

[26] D. C. O'Brien, G. E. Faulkner, K. Jim, D. J. Edwards, E. B. Zyambo, P. Stavrinou, G. Parry, J. Bellon, M. J. Sibley, R. J. Samsudin, D. M. Holburn, V. A. Lalithambika, V. M. Joyner, and R. J. Mears. *Experimental characterization of integrated optical wireless components.* IEEE Photonics Technology Letters, 18(5-8):977–979, 2006.

[27] Hoa Le Minh, Dominic O'Brien, Grahame Faulkner, Olivier Bouchet, Mike Wolf, Liane Grobe, and Jianhui Li. *A 1.25-Gb/s Indoor Cellular Optical Wireless Communications Demonstrator*. IEEE Photonics Technology Letters, 22(21):1598–1600, 2010.

[28] P. Brandl, R. Swoboda, W. Gaberl, and H. Zimmermann. *Integrated optical receiver for indoor wireless gigabit communication*. Optics Communications, 285:1075–1077, 2012.

3

Optical Phased Arrays

"Optical phased arrays represent an enabling new technology that makes possible simple, affordable, lightweight, optical sensors offering very precise stabilization, random-access pointing, programmable multiple simultaneous beams, a dynamic focus/defocus capability and moderate to excellent optical power handling capability." (Paul F. McManamon et. al. [1]).

Phased array technology has proven to be a versatile way to provide high performance and operational flexibility for microwave systems. By splitting up a large antenna into multiple small antennas and having phase and/or amplitude control over these antennas, the advantages of a large antenna (being very directive) and a small antenna (having a large coverage range) can be combined. This technology is used in the microwave world where large antenna arrays have been deployed in for example the astronomy world. Also in the MIMO (Multiple-Input Multiple-Output) domain, the use of antenna arrays increases the data capacity and reliability of wireless networks [2].

The same principle can be transferred to the optical domain, i.e., splitting a large aperture into small sub-apertures over which the phase can be controlled. This results in a so-called Optical Phased Array (OPA). While the principle is the same, the technological implementation is quite different due to the specific nature of the optical signal. First of all, due to the small wavelength of light (nm-μm range) it becomes challenging to overcome the $\lambda/2$ spacing constraint

to avoid higher output orders of the array. Secondly, phase tuning of light has a different technological implementation than phase tuning of RF signals. As an ideal OPA allows to create a random phase profile of a light beam, it is not only useful in beam steering but also beam focusing, shaping and wavefront sensing or correction applications.

A major advantage of OPAs is the absence of mechanical motion. For optical beam steering, there is the need for accurate pointing and stabilization due to the small wavelength of light. A bulk mechanical steering approach is therefore less preferred as it is sensitive to acceleration, expensive and limited in speed due to the masses involved. Random pointing and rapid steering then become difficult and often require a large amount of power. OPAs do not require any mechanical motion, making them insensitive to acceleration. The steering speed is determined by the phase tuning speed. This can happen fast depending on the technological implementation.

Next, in Section 3.1, the OPA theory will be explained, where we exploit the analogy with RF phased arrays but also point out some differences. Section 3.2 gives an overview of the technological implementations of OPAs as well as a short overview of other optical steering techniques. Finally, Section 3.3 deals with application areas where OPAs show great potential in present-day or future applications. Section 3.4 presents the conclusions.

3.1 Theory

While there is a large difference in wavelength between microwave phased arrays and optical phased arrays, the main theoretical concepts remain the same and are found in any standard microwave radar book [3]. In this section, a brief overview of the main concepts is presented with a focus on the optical domain. Firstly, diffraction theory is reviewed in Section 3.1.1. Then the link with far-field radiation pattern terminology is made and specific definitions that will be used throughout this work are introduced in Section 3.1.2 and 3.1.3.

While we try to exploit the analogy with RF theory, one needs to take care whether the definitions also have a meaning in the optical domain. Some conditions or assumptions might not be met anymore due to the very small wavelength of light compared to typical RF signals. Section 3.1.4 deals with the physics behind non-mechanical beam steering followed by the phased array concept in Section 3.1.5. Finally some relevant examples are given in Section 3.1.6.

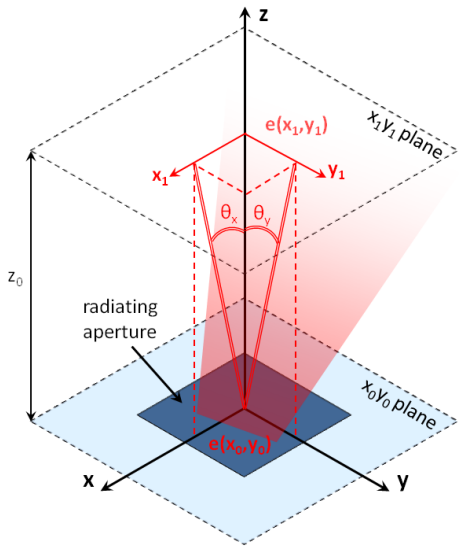

Figure 3.1: Diffraction of light through an aperture.

3.1.1 Diffraction theory

Using scalar diffraction theory, the far-field of a radiating aperture can be calculated. This theory holds when the aperture is large compared to the wavelength and when the fields of interest are at a large distance from the aperture. An in-depth analysis of diffraction theory and Fourier optics can be found in literature [4]. The main results are summarized below.

The diffraction of an aperture with a scalar field e in the x_0y_0-plane to the x_1y_1-plane at a distance z_0 (Figure 3.1) can be described by the Fresnel diffraction integral:

$$e(x_1,y_1) = \frac{je^{-jkz_0}}{\lambda z_0} e^{-\frac{jk}{2z_0}(x_1^2+y_1^2)} \iint_{-\infty}^{+\infty} e(x_0,y_0) e^{-\frac{jk}{2z_0}(x_0^2+y_0^2)} e^{j\frac{2\pi}{\lambda z_0}(x_1x_0+y_1y_0)} \mathrm{d}x_0 \mathrm{d}y_0. \tag{3.1}$$

When the distance z_0 is large:

$$z_0 >> \frac{k}{2}(x_0^2+y_0^2), \tag{3.2}$$

the phase term can be neglected and we obtain the Fraunhofer diffraction formula:

$$e(x_1,y_1) = \frac{je^{-jkz_0}}{\lambda z_0} e^{-\frac{jk}{2z_0}(x_1^2+y_1^2)} \iint_{-\infty}^{+\infty} e(x_0,y_0) e^{j\frac{2\pi}{\lambda z_0}(x_1x_0+y_1y_0)} \mathrm{d}x_0 \mathrm{d}y_0, \tag{3.3}$$

where we can see that the far-field becomes a simple Fourier transform of the near-field. A few special cases can be solved analytically.

Rectangular aperture

$$e(x_0, y_0) = \text{rect}(x_0/w_x)\text{rect}(y_0/w_y), \tag{3.4}$$

where the rect-function is defined as:

$$\text{rect}(x) = \begin{cases} 1 & ,|x| \leq 1/2 \\ 0 & ,|x| > 1/2 \end{cases} \tag{3.5}$$

The radiation pattern at a distance z_0 is given by a sinc pattern:

$$e(x_1, y_1) = \frac{je^{-jkz_0}}{\lambda z_0} e^{-\frac{jk}{2z_0}(x_1^2+y_1^2)} w_x w_y \text{sinc}\frac{\pi w_x x_1}{\lambda z_0} \text{sinc}\frac{\pi w_y y_1}{\lambda z_0}. \tag{3.6}$$

Gaussian aperture

$$e(x_0, y_0) = e^{-\frac{x_0^2+y_0^2}{w^2}}, \tag{3.7}$$

The radiation pattern at a distance z_0 is again a Gaussian, given by:

$$e(x_1, y_1) = \frac{je^{-jkz_0}}{\lambda z_0} e^{-\frac{jk}{2z_0}(x_1^2+y_1^2)} w^2 e^{-(\frac{\pi w}{\lambda z_0})^2(x_1^2+y_1^2)}. \tag{3.8}$$

3.1.2 Far-field patterns

In microwave theory, the far-field radiation pattern of an antenna is given by:

$$e(\mathbf{r}) = F(\theta, \phi)\frac{e^{-jk_0R}}{R}, \tag{3.9}$$

with $F(\theta, \phi)$ the radiation vector and $R = |\mathbf{r}|$. The last factor e^{-jk_0R}/R is the far-field pattern of an isotropic radiator. This is only valid in the far-field region, i.e., when $R > 2d^2/\lambda$ with d the size of the antenna and λ the wavelength of radiation. The radiation vector (which is just a scalar quantity in this case) gives the radiation distribution relative to an isotropic radiator. It only depends on the direction of emission (θ, ϕ) which are usually the standard spherical angles.

In the following discussion, a different set of angles θ_x and θ_y will be used as shown in Figure 3.1. These are not the standard spherical angles, but the angles of the radiation pattern when looking at an xz-cut and yz-cut, respectively. Such a representation allows to more easily describe the far-field pattern in the different cuts. There is a simple relation between these angles and the standard

spherical angles θ and ϕ (with θ the angle with the z-axis and ϕ the angle between the projection on the xy-plane and the x-axis):

$$\sin\theta_x = \sin\theta\cos\phi \tag{3.10}$$

$$\sin\theta_y = \sin\theta\sin\phi \tag{3.11}$$

Equation (3.3) and (3.9) show a big similarity. The e^{-jkz_0}/z_0 represents the isotropic radiator and the remainder represents the radiation vector which is, apart from the phase factor, a function of x_1/z_0 and y_1/z_0. Noting that in the derivation of Equation (3.3) it has been approximated that $R \approx z_0$, we can write:

$$\frac{x_1}{z_0} \approx \frac{x_1}{R} = \sin\theta_x \tag{3.12}$$

$$\frac{y_1}{z_0} \approx \frac{y_1}{R} = \sin\theta_y, \tag{3.13}$$

which shows that the distribution of the radiation vector is, apart from the phase factor, only dependent on the direction of emission.

3.1.3 Antenna directivity and gain

Antenna directivity $D(\Omega)$ is defined as the amount of power radiated in a specific direction Ω compared to the power radiated by an isotropic radiator:

$$D(\Omega) = 4\pi\frac{|F(\Omega)|^2}{2Z_cP_{rad}}, \tag{3.14}$$

with Ω the solid angle of emission, Z_c the characteristic impedance of the medium and P_{rad} the radiated power. The factor $|F(\Omega)|^2/2Z_c$ is equal to the radiated intensity $I(\Omega)$. Taking into account the antenna efficiency η, the antenna gain $G(\Omega)$is defined as:

$$G(\Omega) = \eta D(\Omega). \tag{3.15}$$

Both directivity and gain are expressed in dBi which refers to a dB scale compared to an isotropic radiator. One needs to take care when translating this concept to an optical antenna. All these formulas assume that we are working in the far-field, such that only one direction of emission reaches the receiver. Due to the small wavelength of light, this condition is not always met in the optical case as a light beam can be very directional. A modification to the formulas can be used to extend the validity of the model [5]:

$$G(\Omega) = 4\pi\eta\frac{\int_{\Omega_{div}}|F(\Omega)|^2\mathrm{d}\Omega_{div}}{2Z_cP_{rad}\Omega_{div}}, \tag{3.16}$$

with Ω_{div} the divergence solid angle of the optical beam from transmitter to receiver. Note that the gain will become dependent on the receiver position

through Ω_{div}. For the case where there is a large diffraction of the optical beam, which is often the case for the small integrated structures considered in this work, Equation (3.15) works as a good approximation.

Using the above definitions, the optical analog of Friis formula to perform link budget calculations with optical antennas is given by:

$$P_r = P_t G_t (\frac{\lambda}{4\pi d})^2 Q_{rt} G_r, \tag{3.17}$$

with P_r the received power, $G_{t,r}$ the transmitter/receiver gain, d the distance between the antennas and Q_{rt} a polarization mismatch factor. The factor $[\lambda/(4\pi d)]^2$ represents the loss factor of a spherical wave that has propagated a distance d. This formula is valid when the optical receiver is working as an antenna (for example an optical fiber that captures the light in an EM mode) and not just as a photodiode. The formalism is used in Chapter 6 to investigate the directivity of the fabricated OPAs. Knowing the directivity of the antenna, a link budget calculation can be done using Equation (3.17).

3.1.4 Non-mechanical beam steering

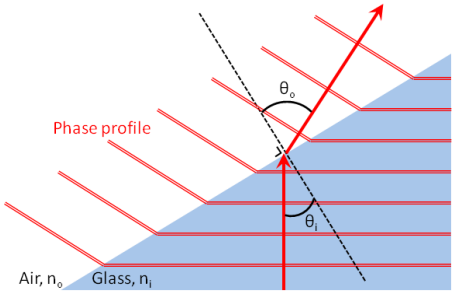

Figure 3.2: Beam steering using a prism.

Before discussing the principle of phased arrays, the physics behind non-mechanical beam steering are explained here. The simplest way to look at beam steering is to look at the effect of a beam incident on a prism as shown in Figure 3.2. The law of Snellius says that:

$$n_i \sin\theta_i = n_o \sin\theta_o, \tag{3.18}$$

with $n_{i,o}$ the refractive indices of the two materials and $\theta_{i,o}$ the angles with the normal of the surface. What happens with the phase profile? As glass has a higher refractive index than air, the wave travels more slowly in the prism. As soon as the light exits the prism, it will travel faster again. Due to the oblique

side of the prism, the wavefront is tilted as shown in Figure 3.2 resulting in beam steering. By dynamically defining a prism, it is possible to steer the beam. The difficulty arises in the large optical path differences (OPD) that are needed for large apertures. This can be solved by using 2π phase resets as shown in Figure 3.3, resulting in a blazed grating. These resets will make the steering efficiency wavelength dependent as for a different wavelength, the resets will not be correct. Therefore, this approach is only possible in narrowband systems.

While the blazed grating can be programmed as such, the blaze can also be discretized using a staircase approximation. This latter approach is used in the integrated OPAs fabricated in this work. The diffraction efficiency of a grating with a staircase blaze designed to maximize energy in the first order is given by:

$$\eta = \left(\frac{sin(\pi/q)}{\pi/q}\right)^2, \tag{3.19}$$

with q the number of steps in the blaze profile. For $q \to \infty$, this efficiency becomes 1. To avoid the 2π phase resets, the maximum steering angle θ_{max} will remain very small and is limited to:

$$\sin\theta_{max} = \frac{\lambda}{N\Lambda}, \tag{3.20}$$

with N the number of elements and Λ the element spacing, $N\Lambda$ is thus the aperture size. As will become clear from the discussion in Section 3.1.5, discretization of the aperture with a spacing larger than half a wavelength also leads to higher order lobes spaced at a distance, called free spectral range (FSR):

$$\Delta\theta_{FSR} \approx \arcsin\frac{\lambda}{\Lambda}[\approx \frac{\lambda}{\Lambda}], \tag{3.21}$$

where the last approximation is valid for small $\Delta\theta_{FSR}$ or when λ/Λ is small.

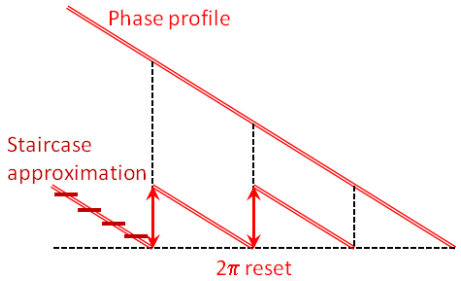

Figure 3.3: Tilted phase front with corresponding saw-tooth profile and staircase approximation.

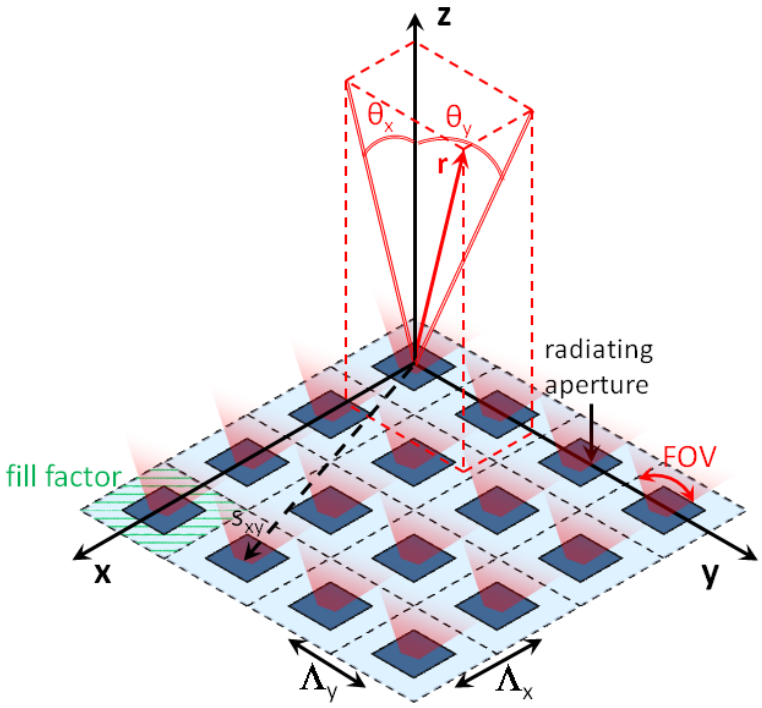

Figure 3.4: Schematic representation of an OPA.

3.1.5 Phased arrays

Figure 3.4 shows a schematic representation of a two-dimensional OPA. It consists of an $N_x \times N_y$ array of radiating apertures spaced Λ_x and Λ_y, respectively. Each radiating aperture can be thought of as a single antenna. The total FOV of the OPA is determined by the FOV of one such aperture as indicated in the figure.

The (scalar) far-field e at a certain point $\mathbf{r}$ in space can be written as the mathematical sum of all the radiation patterns $F_{xy}(\theta_x, \theta_y)$ with the proper phase factors:

$$e(\mathbf{r}) = \sum_{n_x=0}^{N_x-1} \sum_{n_y=0}^{N_y-1} A_{xy} e^{j\beta_{xy}} F_{xy}(\theta_x, \theta_y) \frac{e^{-jk_0|\mathbf{r}-\mathbf{s}_{xy}|}}{|\mathbf{r}-\mathbf{s}_{xy}|}, \tag{3.22}$$

where A_{xy} is the field amplitude and β_{xy} is the relative phase at each element. F_{xy} denotes the far-field of each element, referenced to its own phase center (hence the index xy), k_0 is the free-space wave vector and $\mathbf{s}_{xy}$ is the position of the radiating element.

Some further simplifications are possible. In the far-field, the radiation patterns $F_{xy}(\theta_x, \theta_y)$ can to a good approximation be considered to be referenced to

the same phase center $F_{xy}(\theta_x,\theta_y) \approx F_{00}(\theta_x,\theta_y) = F(\theta_x,\theta_y)$. The denominator in (3.22) can be approximated by $|\mathbf{r}-\mathbf{s}_{xy}| \approx |\mathbf{r}| = R$. For the phase factor, a more accurate approximation is needed as this factor is more sensitive to variations:

$$|\mathbf{r}-\mathbf{s}_{xy}| \approx R - \mathbf{u}_r \cdot \mathbf{s}_{xy}, \tag{3.23}$$

with $\mathbf{u}_r$ the unit vector along the $\mathbf{r}$-direction. This finally results in:

$$e(\mathbf{r}) = \underbrace{F(\theta_x,\theta_y)\frac{e^{-jk_0R}}{R}}_{1} \underbrace{\sum_{n_x=0}^{N_x-1}\sum_{n_y=0}^{N_y-1} A_{xy}e^{j\beta_{xy}}e^{-j\mathbf{k}\cdot\mathbf{s}_{xy}}}_{2}, \tag{3.24}$$

The field expression (3.24) consists of two contributions. The first factor is the far-field of one element (Equation (3.9)), while the second factor is a summation factor to take into account all the different contributions, this is called the array factor $T(\theta_x,\theta_y)$:

$$T(\theta_x,\theta_y) = \sum_{n_x=0}^{N_x-1}\sum_{n_y=0}^{N_y-1} A_{xy}e^{j\beta_{xy}}e^{-j\mathbf{k}\cdot\mathbf{s}_{xy}}. \tag{3.25}$$

Uniform arrays

Assume an equal amplitude $A_{xy} = A$ and phase $\beta_{xy} = \beta$ to each element. When there is a uniform spacing of the elements, $\mathbf{s}_{xy} = n_x\Lambda_x\mathbf{u}_x + n_y\Lambda_y\mathbf{u}_y$, with Λ_x and Λ_y the element spacing in the x- and y-direction, respectively, the array factor can be calculated in closed form:

$$\begin{aligned} T(\theta_x,\theta_y) &= Ae^{j\beta}\sum_{n_x=0}^{N_x-1}\sum_{n_y=0}^{N_y-1} e^{-j\mathbf{k}\cdot\mathbf{s}_{xy}} \\ &= Ae^{j\beta}\sum_{n_x=0}^{N_x-1}\sum_{n_y=0}^{N_y-1} e^{-j[n_xk_0\Lambda_x\sin\theta_x + n_yk_0\Lambda_y\sin\theta_y]} \\ &= Ae^{j\beta}e^{j\gamma}\frac{\sin(\frac{N_x}{2}k_0\Lambda_x\sin\theta_x)}{\sin(\frac{1}{2}k_0\Lambda_x\sin\theta_x)}\frac{\sin(\frac{N_y}{2}k_0\Lambda_y\sin\theta_y)}{\sin(\frac{1}{2}k_0\Lambda_y\sin\theta_y)}, \end{aligned} \tag{3.26}$$

where γ is a phase factor given by:

$$\gamma = \frac{N_x-1}{2}k_0\Lambda_x\sin\theta_x + \frac{N_y-1}{2}k_0\Lambda_y\sin\theta_y. \tag{3.27}$$

Scanning arrays

To use the OPAs as scanning arrays, there should be a fixed phase difference $\Delta\varphi_{x,y}$ between the elements:

$$\beta_{xy} = n_x\Delta\varphi_x + n_y\Delta\varphi_y. \tag{3.28}$$

Equation (3.26) can then be written as:

$$\begin{aligned} T(\theta_x,\theta_y) &= A\sum_{n_x=0}^{N_x-1}\sum_{n_y=0}^{N_y-1} e^{-j[n_x(k_0\Lambda_x\sin\theta_x-\Delta\varphi_x)+n_y(k_0\Lambda_y\sin\theta_y-\Delta\varphi_y)]} \\ &= Ae^{j\gamma}\frac{\sin[\frac{N_x}{2}(k_0\Lambda_x\sin\theta_x-\Delta\varphi_x)]}{\sin[\frac{1}{2}(k_0\Lambda_x\sin\theta_x-\Delta\varphi_x)]}\frac{\sin[\frac{N_y}{2}(k_0\Lambda_y\sin\theta_y-\Delta\varphi_y)]}{\sin[\frac{1}{2}(k_0\Lambda_y\sin\theta_y-\Delta\varphi_y)]}, \end{aligned} \tag{3.29}$$

with γ a similar phase factor as defined above:

$$\gamma = \frac{N_x-1}{2}(k_0\Lambda_x\sin\theta_x-\Delta\varphi_x)+\frac{N_y-1}{2}(k_0\Lambda_y\sin\theta_y-\Delta\varphi_y). \tag{3.30}$$

The array factor shows a maximum when both numerator and denominator become zero or when:

$$\begin{aligned} \frac{1}{2}(k_0\Lambda_x\sin\theta_x-\Delta\varphi_x) &= q\pi \\ \sin\theta_x &= (q+\frac{\Delta\varphi_x}{2\pi})\frac{\lambda}{\Lambda_x}, \end{aligned} \tag{3.31}$$

with q an integer. A similar expression holds for the θ_y-angle. Different orders are emitted by the array, indicated by the integer m. Only when the spacing $\Lambda_x < \lambda/2$, there will only be one order visible, independent of the beam steering phase difference $\Delta\varphi_x$. This $\lambda/2$ spacing constraint is well-known in phased array technology. The uniform phase difference $\Delta\varphi_x$ results in a linear shift of the sine of the angle and for a 2π phase difference, we end up at a higher order. The spacing between the different orders of the array factor is given by:

$$\sin\theta_{x,q+1}-\sin\theta_{x,q} = \frac{\lambda}{\Lambda_x}. \tag{3.32}$$

When the angles θ_x are relatively small, this is usually approximated as:

$$\Delta\theta_{FSR,x} \approx \arcsin\frac{\lambda}{\Lambda_x}[\approx \frac{\lambda}{\Lambda_x}], \tag{3.33}$$

The FWHM (Full Width at Half Maximum) beamwidth $\Delta\theta_{FWHM,x}$ is approximately equal to:

$$\Delta\theta_{FWHM,x} \approx 0.886\frac{\lambda}{N_x\Lambda_x\cos\theta_x}, \tag{3.34}$$

where it is dependent on the steered angle θ_x. For small steering angles this can further be approximated by the rule of thumb:

$$\Delta\theta_{FWHM,x} \approx \frac{\lambda}{N_x\Lambda_x}. \tag{3.35}$$

Looking at Equation (3.33) and Equation (3.35), we can see the important result that the number of resolvable spots scales with the number or elements N_x:

$$\frac{\Delta\theta_{FSR,x}}{\Delta\theta_{FWHM,x}} \approx \frac{\frac{\lambda}{\Lambda_x}}{\frac{\lambda}{N_x\Lambda_x}} = N_x. \tag{3.36}$$

While the number of resolvable spots is determined by the number of independent elements, the tracking accuracy, i.e., the accuracy with which one can steer the beam, depends on the phase accuracy between the elements. The better the different phases can be controlled, the more accurate the beam can be steered. This accuracy thus depends on the technological implementation of the phase tuners.

There is another interesting implication of the above formulas. The directivity of a certain radiating aperture is directly related to its size: very large apertures are very directive. It is noteworthy mentioning that this directivity is independent of fill-factor or spacing of the elements. When we divide the aperture in several subapertures and increase their spacing, extra higher order lobes will arise due to the increased spacing, but at the same time, the lobes get narrower following Equation (3.34). On average, both effects cancel out and the directivity remains constant.

3.1.6 Examples

Some far-field patterns of typical OPAs relevant for this research are explored in this section. First, the standard example of an array of rectangular apertures is given. Next, some examples of Gaussian and exponential fields are presented. The latter is interesting as a grating aperture that couples out light from a silicon photonics circuit can typically be described by such an aperture. We will limit the examples to a one-dimensional approach as the two-dimensional fields can in general be described by two one-dimensional fields.

Rectangular aperture array

For a rectangular aperture, the far-field was given by Equation (3.6), together with the array factor given by Equation (3.26), the far-field is thus of the form:

$$I = I_0 \left| \frac{\sin(k_0 \frac{w_x}{2} \sin\theta_x)}{k_0 \frac{w_x}{2} \sin\theta_x} \times \frac{\sin(\frac{N_x}{2} k_0 \Lambda_x \sin\theta_x)}{\sin(\frac{1}{2} k_0 \Lambda_x \sin\theta_x)} \right|^2, \tag{3.37}$$

with I_0 a constant factor, k_0 the free-space wave vector, w_x the width of the aperture, N_x the number of apertures and Λ_x the aperture spacing. It is interesting to look at the influence of the fill-factor of the array. For a uniform fill

factor $w_x = \Lambda_x$, the zeros of the sinc are at:

$$\pi \frac{w_x}{\lambda} \sin\theta_x = q\pi \tag{3.38}$$

$$\sin\theta_x = q\frac{\lambda}{w_x}, \tag{3.39}$$

with q a non-zero integer. This is exactly equal to the spacing of the peaks of the array factor given by Equation (3.31). For a uniform fill factor, the array actually acts as one large uniform apertures and thus only one peak is visible. This is, however, only when the peak is not steered. This is shown in Figure 3.5, where the far-field of a 10 μm rectangular aperture is shown, as well as the array factor of 16 of these apertures with a uniform fill-factor. The envelope has a FWHM of 8.0°. As soon as steering comes into play, two peaks will become visible as the peaks of the array factor will shift. For a decreasing fill-factor, more peaks will be visible in the far-field pattern because the spacing of the peaks of the array factor will decrease. This will become clear in the next examples.

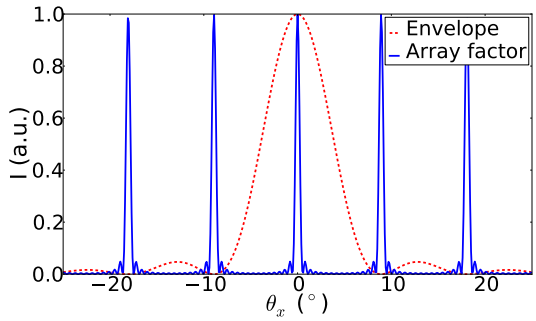

Figure 3.5: Envelope of a 10 μm wide aperture and array factor of 16 apertures with uniform fill-factor (spacing $\Lambda_x = w_x = 10$ μm) at $\lambda = 1550$ nm.

Gaussian aperture array

A more practical example is the Gaussian aperture. The fundamental mode of an integrated photonic waveguide or optical fiber can be approximated with a Gaussian function which can also be solved analytically. Assume for example a Gaussian with a full 1/e-width of 7.5 μm. This is approximately the mode-width of an optical fiber at a wavelength of 1550 nm, and thus also of the standard grating couplers that are used to couple to such a fiber [6]. Figure 3.6 shows the far-field of such a Gaussian, as well as the far-field of arrays of these Gaussians spaced 50 μm. The practical relevance of this example will become clear in Chapter 6. The far-field of one of these Gaussians has an intensity FWHM

beamwidth $\Delta\theta_{FWHM,x}$ of:

$$\Delta\theta_{FWHM,x} \approx \frac{\lambda}{\pi w_x}\sqrt{2\ln 2}, \tag{3.40}$$

with w_x the half 1/e-width. This results in $\Delta\theta_{FWHM,x} = 8.9°$. As the number of elements is increased to N, the lobes get smaller by the same factor N as indicated by Equation (3.34).

The effect of the element spacing becomes clear when comparing Figure 3.5 and Figure 3.6. As the spacing becomes a factor 5 larger (10 μm → 50 μm), the peak spacing of the array factor will roughly decrease with a factor 5 resulting from Equation (3.33).

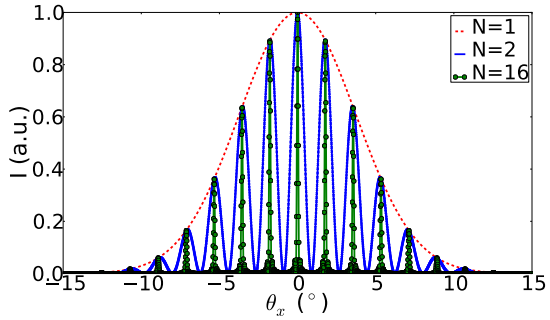

Figure 3.6: Far-field of an array of Gaussians with a full 1/e-width of 7.5 μm, spaced 50 μm, for different number of elements at λ = 1550 nm.

Due to the large element spacing there is a multitude of higher order lobes, which is unwanted in most applications where we want a single directive beam. By using narrower waveguides that are spaced closer, the steering becomes much more directive as the number of higher order lobes decreases. Figure 3.7, for example, shows the far-field of a Gaussian with a full 1/e-width of 614 nm (corresponding to the TE (Transverse Electric) fundamental mode width of an 800 nm wide integrated photonic waveguide on SOI (Silicon-On-Insulator), discussed in Chapter 4) with a 2 μm spacing for different elements. The envelope beamwidth is now $\Delta\theta_{FWHM,x} = 110.0°$ while the spacing of the output lobes is 50.8° at λ = 1550 nm. For these small apertures and large angles, the scalar formalism above is, however, not strictly valid anymore, but remains a good approximation as will become clear in the experimental results.

Exponential aperture

As a final example, the far-field of an exponential decaying field is plotted in Figure 3.8. The output field of a grating can typically be described by an expo-

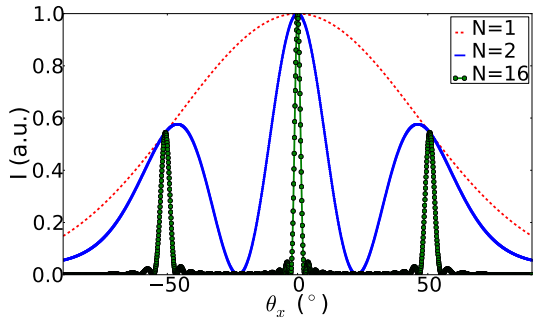

Figure 3.7: Far-field of an array of Gaussians with a full 1/e-width of 0.614 μm, spaced 2 μm, for different number of elements at $\lambda = 1550$ nm.

nential decaying field, where the decay strength α is depending on the strength of the grating (i.e., the refractive index difference):

$$f(x) = \begin{cases} 0 & , x < 0 \\ \exp(-\alpha x) & , x \geq 0. \end{cases} \tag{3.41}$$

The Fourier transform can be done analytically and is a Lorentzian shape of the form:

$$I = \frac{\alpha^2 I_0^2}{\alpha^2 + k_0^2 \sin^2 \theta_x} \tag{3.42}$$

A typical decay length for the gratings which are used extensively in this work is $1/\alpha \approx 7$ μm. It is this type of decaying field that is then coupled into free space. By tailoring the grating strength, one can increase of decrease this decay length and thus shape the far-field. These gratings are discussed in more detail in Chapter 4. The far-field of such an exponential can be found in Figure 3.8.

3.2 Technological Implementations

In this section, some of the different OPA technologies will be reviewed. A more in-depth review is given in [1, 7].

There are two main classes of OPAs. Passive OPAs do not generate the light beam themselves, but act on an existing beam as opposed to microwave phased arrays where the signal is generated at the element level itself. These passive OPAs only need to perform phase and/or amplitude tuning on an existing light beam. In active arrays, the different transmitters also generate the light.

The main parameters when looking at OPAs are their speed, power consumption, fill-factor, element spacing, modulation depth and aperture size. Let

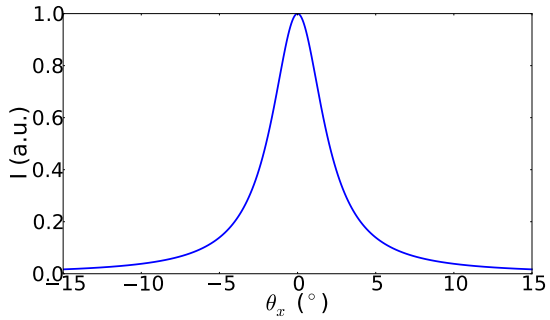

Figure 3.8: Far-field of an exponential with a decay length of $1/\alpha \approx 7$ μm.

us look for example at large angle, large aperture steering. The first condition means that the elements need to be spaced tightly, preferably with high fill factor, while the latter condition then implies a large number of elements to obtain a large aperture. There is then a multitude of steering states (being the range divided by the beam spot size) which increases the complexity of the system as a large number of variables (read: individually addressable phase tuners) is needed to address all these states, dramatically increasing the complexity. There is not a one-type-fit-all solution, but a combination of different approaches will be needed depending on the application in mind.

One of the main challenges of OPAs is their extremely small element size when wanting to obey the $\lambda/2$ spacing constraint (discussed in Section 3.1.5) for large angle steering. To achieve this, 1D arrays are a much more practical approach than full 2D arrays. Layouting and addressing become increasingly difficult in a 2D configuration. When the OPAs work in transmissive mode, full steering can be obtained by using two orthogonal oriented 1D arrays. To enable large-angle steering, usually a cascade is used of fine small-angle (continuous) steering and coarse large-angle (discrete) steering systems.

A brief overview of the mainstream OPA technology, liquid crystal OPAs is presented in the next section. Micro-Electro-Mechanical Systems (MEMS) is another OPA technology briefly discussed in Section 3.2.2. Section 3.2.3 introduces the integrated OPAs on which the remainder of this work is focused. Finally, Section 3.2.4 gives a brief overview of other OPA or non-OPA steering approaches. This is not meant as an in-depth overview, but mainly to familiarize the reader with existing (bulk) steering techniques and to put the current work in perspective with other steering approaches.

3.2.1 Liquid crystal OPAs

Liquid crystals (LC) are the leading OPA technology. The LC technology has undergone a tremendous development, mainly driven by the display market. While these systems work on the principle of polarization rotation due to the tunable birefringence of a LC, there is also a phase shift involved. By removing the polarizers, the phase shift can be observed. For a standard display, the pixel-spacing is relatively large and the phase modulation is limited, resulting in a limited steering efficiency and angle.

To improve the performance, LC elements have been developed that create a linear phase ramp across each pixel. Although every pixel is still a multiple of wavelengths in extent and spacing, due to the linear phase ramp over each element, steering angles of 20° and large apertures should be possible. 1D LC-OPAs with spacings of less than a free-space wavelength have been shown as well, which can steer a beam into a single, diffraction limited beam, but still limited in steering angle due to the needed phase resets as discussed below.

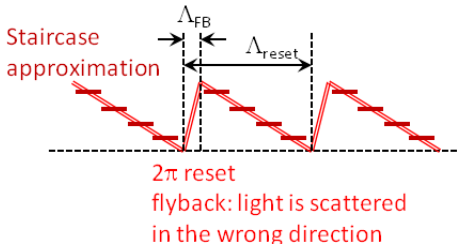

Figure 3.9: Influence of flyback on the beam steering efficiency.

For large angle steering, 2π phase resets are needed. These resets are, however, wavelength dependent and make the steering dispersive. Furthermore, there is the so-called flyback region, i.e., the liquid crystal cannot abruptly mimic a phase reset, this happens over a certain space resulting in a reduced efficiency [8]. This is shown schematically in Figure 3.9. The light that passes through the flyback region is deflected into the wrong direction. The efficiency η_{FB} can be written as:

$$\eta_{FB} = \left(1 - \frac{\Lambda_{FB}}{\Lambda_{reset}}\right)^2, \tag{3.43}$$

with Λ_{reset} the spacing of resets and Λ_{FB} the width of the flyback region. This flyback region typically reduces the efficiency from 99% at 0.1° steering to 90% at 1° steering and then quickly to 25% at 10° steering while 20° is typically the maximal achievable angle. Using a staircase approximation of the blaze, the efficiency is given by Equation (3.19), but this is more than 95% for an 8 step discretization and thus not a significant source of loss.

These LC systems require little power, even for large apertures which can be useful in missile interceptors or satellite communications. Due to the large development of the display market, these systems can be produced at high volume with relatively low cost. One major drawback in these systems is their switching speed which is of the order Hz to kHz.

3.2.2 MEMS

Another approach to fabricate phased arrays is by using MEMS technology. These OPAs consist of micrometer scale mirrors. Two techniques can be used. Firstly, the mirrors can move perpendicular to the substrate to impose a phase difference of the reflected light between two neighboring mirrors. Two important issues here are the fill-factor and the minimal mirror size, as half-wavelength size mirrors are impractical to make. Secondly, the mirrors can be tilted to the desired angle to impose a blazed grating. The blaze will be perfect over the mirror (as long as it is flat) but we are restricted by the 2π resets in order not to have phase discontinuity. This is in contrast with the typical amplitude modulation that is used in MEMS, where the mirrors are used to deflect light out of the optical path. For large angle step-steering, the MEMS approach is feasible. MEMS also work in reflective mode which can be a disadvantage in certain applications. As they depend on mechanical motion, the speed is relatively slow, upto kHz range [9, 10].

3.2.3 Integrated OPAs

In this research, focus lies on the fabrication of integrated optical phased arrays using the silicon photonics platform. The details of this platform are discussed in Chapter 4. Using an integrated approach, one can overcome several limitations of the bulk approach:

- The systems can be made very small. Integrated photonics has undergone tremendous improvements over the last decade and the fabrication of 100 nm structures is now feasible with standard deep-UV (Ultraviolet) lithography.
- Using integrated phase tuning (discussed in Chapter 5), phase modulation can be done without the need of external bulky phase modulators.
- Depending on the wanted speed, different tuning mechanisms can be chosen and steering (random access pointing) at frequencies of more than 10 GHz is possible.
- Using an integrated approach large volume production can be possible at low-cost. This is especially true when using standardized processes.

- When making use of silicon photonics, integration with CMOS driver circuitry can be possible in the future which would result in complex functionality at low-cost.

The first integrated OPA was presented by Vasey [11]. The OPA was fabricated on the AlGaAs platform and worked at a wavelength around 850 nm. Phase tuning was achieved electro-optically using Schottky junctions. A beam with a width of 0.086° was steered over a 0.83° range using 43 elements. The performance was limited due to the large element spacing.

In this work, we will present several OPAs with different steering mechanism and increased performance. Recently (October, 2011) similar work on fabricating integrated OPAs on silicon has been presented in [12]. The components in the work presented here, however, clearly have an improved performance, mainly thanks to the better controlled and well-established fabrication technology.

3.2.4 Other approaches

Microlens array

Steering using lenses requires a minimum of two lenses. By moving the last lens off-axis, beam steering can be obtained. A triplet of lenses is usually used to ensure all the light entering through the first lens, passed through the last lens. Main advantage is that using lenses a smaller optical path difference (OPD) (factor 4) needs to be covered for the same steering effect of a sawtooth grating, but multiple layers are needed [13, 14].

Birefringent prisms

Using a birefringent prism, the different polarizations of light are steered to a different direction. By incorporating a LC polarization rotator between the prism, a binary deflection is obtained. A steering range of ±20° has been shown using such an approach. Liquid crystals can also be used to act as switchable birefringent prisms [15, 16].

Electro-optic and acousto-optic steering

By putting electro-optic (EO) modulators in a (one-dimensional) array configuration, a fast-steerable OPA can be fabricated. This has been shown by [17], where 46 lithium tantalate EO-modulators were shown. In [18] an array of EO prisms was shown. Both were one of the first to investigate the OPA principle. While steering can happen fast, the needed voltages are high due to the EO-

effect. Due to the high spacing of these bulk systems, the steering angle is usually limited to much less than 1°.

Other non-OPA related approaches are the use of electro-optic (EO) or acousto-optic (AO) deflectors. The first can steer a beam in the nanosecond range, while the latter works in the microsecond range. Both approaches need either high voltages or high driving power and are used for small angle (few mrad) fast and fine beam steering applications.

Electrowetting

The principle is again to program a prism-like profile over a pixel. By applying a voltage over a water and oil mixture, we can create a straight, but tilted interface between water and oil. Angles up to 45° are possible. For cells of a few tens of μm, the switching time is in the order of milliseconds [19, 20].

Holographic gratings

Holographic step steering is used as a large angle discrete steering mechanism. A signal and reference beam are used to write a hologram in a holographic medium. When the signal beam then impinges on the hologram, it will be diffracted into the reference beam direction. Multiple holograms can be written in such a medium. The right hologram is then chosen with a small steering mechanism [21, 22]. Using for example two LC steering mechanism with a holographic volume grating in between, continuous steering of 45° has been shown. The first LC steerer chooses the holographic grating for large angle steering while the second LC steerer allows fine tuning [8].

Liquid crystal polarization gratings

While most approaches depend on the creation of an OPD, liquid crystal polarization gratings (LCPG) work on a different principle to create a phase delay. The phase of circularly polarized light passing through a half-wave plate depends on the angle of the half-wave plate. Using polarizers and quarter wave plates we can change this polarization to a linear polarization. Using LCs, such a functionality can be obtained. Main advantage of such an approach is that cells can be made thin and resets can be avoided since the phase change does not directly depend on the molecule orientation [23].

3.3 Applications

Some of the present and future application domains of OPAs are presented here. Wireless optical communication is a large application field which was already

covered in Chapter 2. Another recent hot-topic is optical interconnects, discussed in Section 3.3.1. Sections 3.3.2 and 3.3.3 finally deal with optical scanning and sensing applications.

3.3.1 Optical interconnects

Also at the very short range, such as on- or intra-chip communication, a shift from electrical to optical signals can be observed. The electronic world is reaching an interconnect bottleneck for which optical interconnects can offer several advantages. While waveguides can be used as optical interconnects, free-space interconnects have recently also gained attention, especially for so-called 'off-board' interconnect on boards and backplanes [24] or intra-chip interconnects. These free-space interconnects can have a high signal density with limited crosstalk as free-space optical signals do not interfere with each other. They further exhibit low latency and high energy density.

In [25], a free-space intra-chip interconnect using a VCSEL (Vertical Cavity Surface Emitting Laser) array and integrated MSM (Metal Semiconductor Metal) Ge detectors was shown working at 3.3 GHz bandwidth, where the speed was mainly limited by the VCSEL bandwidth. A schematic of such an interconnect can be found in Figure 3.10. When having beam steering functionality, the interconnect can furthermore immediately act as dynamic router. Phased array technology and especially integrated phased arrays show great potential in this area.

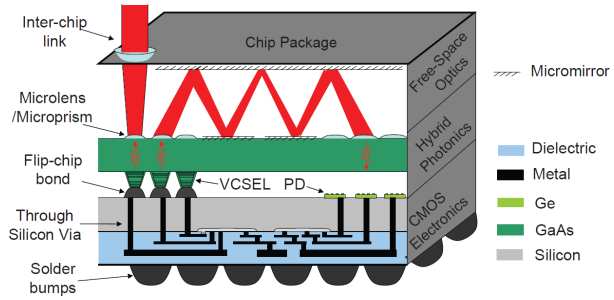

Figure 3.10: Illustration of a free-space interconnect using a 3D integrated chip stack [25].

3.3.2 Optical scanning: LIDAR

One of the key areas of phased arrays is laser scanning such as in LIDAR (LIght Detection And Ranging) type applications. LIDAR has the advantage of accurate localization and imaging of objects with high resolution thanks to the small

wavelength (and thus large directivity) of light, which can be used to accurately model objects or to make accurate topography maps. LIDARs are also used extensively in atmospheric research. Investigation of backscattered light gives information about wind profiling, aerosol or other gas concentration. It furthermore has applications in automation and remote sensing.

3.3.3 Optical sensing

There is a multitude of optical sensing methods in our present day society. Biomedical imaging is one important application field. Using common (non-optical) techniques such as MRI (Magnetic Resonance Imaging), CT (Computed Tomography) or PET (Positron Emission Tomography) scans, a trade-off needs to be made between imaging depth, resolution, speed and cost. Optical techniques perform better on almost all points. The main drawback of optics is the limited penetration depth in turbid tissue such as skin or muscle. This is usually limited to a few 100 μm due to the scattering of the medium preventing the formation of a sharp image. Wavefront shaping has been investigated in [26] to counter these scattering effects and focus light through tissue. Optical phased arrays can play a vital role in this as they can act as wavefront shaper.

This wavefront shaping is especially useful in so-called 'interferometric focusing'. Interferometric focusing tries to combine the strengths of techniques relying on ballistic (i.e., not scattered) light, such as confocal microscopy or Optical Coherence Tomography (OCT), and diffuse light, such as Diffuse Tomography [1]. The former has a high resolution but limited penetration depth while the latter has a high penetration depth but lower resolution. Interferometric focusing relies on the inference of scattered light to form a focus. By modifying the phase front impinging (i.e., creating a phase conjugate field), one can make the light focus through the turbid medium. The more independent control over the phases, the better the focus will be. Drawback is that a feedback loop is necessary to construct the phase conjugate field. With present techniques, this takes seconds to minutes. Integrated structures can play an important role here as the speed and sensitivity can be increased by scaling down the components.

Phased array wavefront correctors are also used in adaptive optics applications such as laser beam propagation [27] through the atmosphere. Applications are also found in astronomy where the atmospheric influence on telescope images needs to be countered [28].

[1] Diffuse Tomography captures the diffuse scattered light and estimates where the scattering occurred to determine an image.

3.4 Conclusions

OPAs are very versatile components, allowing fast and precise beam steering without the need of any mechanical motion. The theory about OPAs is very similar to antenna array theory. Some definitions, however, are not strictly valid anymore in the optical domain.

The main OPA technology uses LCs. While a huge number of pixels can be addressed, there are some drawbacks in steering efficiency and speed. MEMS technology typically suffers from the same drawbacks. Integrated OPAs can be fabricated with small elements resulting in a large steering range, as will become clear in Chapter 6. Large radiating apertures are, however, difficult. Some other steering approaches have been reviewed as well.

Finally, some of the main applications of OPAs were presented. They are useful in wireless LOS link schemes for wireless optical communication as discussed in Chapter 2. They also find applications in a variety of sensing domains. They furthermore can act as adaptive optics components to compensate for phase errors in for example astronomic images.

References

[1] P. F. McManamon, T. A. Dorschner, D. L. Corkum, L. J. Friedman, D. S. Hobbs, M. Holz, S. Liberman, H. Q. Nguyen, D. P. Resler, R. C. Sharp, and E. A. Watson. *Optical phased array technology.* Proceedings of the IEEE, 84(2):268–298, 1996.

[2] Lizhong Zheng and David N. C.l Tse. *Diversity and Multiplexing: A Fundamental Tradeoff in Multiple-Antenna Channels.* IEEE Transactions on Information Theory, 49(5):1073–1096, 2003.

[3] M. I. Skolnik. *Introduction to Radar Systems.* McGraw-Hill, 1962.

[4] Joseph W. Goodman. *Introduction to Fourier Optics.* McGraw-Hill, Inc., 1986.

[5] A. Polishuk and S. Arnon. *Communication performance analysis of microsatellites using an optical phased array antenna.* Optical Engineering, 42(7):2015–2024, 2003.

[6] D. Taillaert. *Grating Couplers as Interface Between Optical Fibres and Nanophotonic Waveguides.* UGent, PhD Thesis, 2006.

[7] P. F. McManamon, P. J. Bos, M. J. Escuti, J. Heikenfeld, S. Serati, H. K. Xie, and E. A. Watson. *A Review of Phased Array Steering for Narrow-Band Electrooptical Systems.* Proceedings of the IEEE, 97(6):1078–1096, 2009.

[8] Paul F. McManamon. *Agile nonmechanical beam steering.* Optics and Photonics News, 17(3):24–29, 2006.

[9] V. Milanovic, G. A. Matus, and D. T. McCormick. *Gimbal-less monolithic silicon actuators for tip-tilt-piston micromirror applications.* IEEE Journal of Selected Topics in Quantum Electronics, 10(3):462–471, 2004.

[10] L. Wu and H. Xie. *A large vertical displacement electrothermal bimorph microactuator with very small lateral shift.* Sensors and Actuators A, 145:371–379, 2008.

[11] F. Vasey, F. K. Reinhart, R. Houdré, and J. M. Stauffer. *Spatial Optical Beam Steering with an Algaas Integrated Phased-Array.* Applied Optics, 32(18):3220–3232, 1993.

[12] J. K. Doylend, M. J. R. Heck, J. T. Bovington, J. D. Peters, L. A. Coldren, and J. E. Bowers. *Two-dimensional free-space beam steering with an optical phased array on silicon-on-insulator.* Optics Express, 19(22):21595–21604, 2011.

[13] E. A. Watson. *Analysis of beam steering with decentered microlens arrays.* Optical Engineering, 32(11):2665–2670, 1993.

[14] E. A. Watson, W. E. Whitaker, C. D. Brewer, and S. R. Harris. *Implementing optical phased array beam steering with cascaded microlens array.* IEEE Aerospace Conference Proceedings, 3:1429–1436, 2002.

[15] U. Schmidt and W. Hust. *Optical deflection system including an alternating sequence of birefringent prisms and polarizers.* United States Patent 3 572 895, 1986.

[16] Khan S. A. and N. A. Riza. *Demonstration of 3-dimensional wide angle laser beam scanner using liquid crystals.* Optics Express, 12(5):868–882, 2004.

[17] R. A. Meyer. *Optical Beam Steering Using a Multichannel Lithium Tantalate Crystal.* Applied Optics, 11(3):613, 1972.

[18] Y. Ninomiya. *Ultrahigh resolving electrooptic prism array light deflectors.* IEEE Journal of Quantum Electronics, QE 9(8):791–795, 1973.

[19] N. R. Smith, D. C. Abeysinghe, J. W. Haus, and J. Heikenfeld. *Agile wide-angle beam steering with electrowetting microprisms.* Optics Express, 14(14):6557–6563, 2006.

[20] N. R. Smith, L. Hou, J. Zhang, and J. Heikenfeld. *Experimental validation of > 1 kHz electrowetting modulation.* In 17th Biennial University/Government/Industry Micro/Nano Symposium Proceedings (UGIM 2008).

[21] J. P. Huignard, A. M. Roy, and C. Slezak. *Electro-optical deflection apparatus using holographic grating.* United States Patent 3 980 389, 1976.

[22] I. W. Smith and M. K. O. Holz. *Wide angle beam steering system.* United States Patent 7 215 472, 2007.

[23] J. Kim, C. Oh, M. J. Escuti, L. Hosting, and S. Serati. *Wide-angle, nonmechanical beam steering with high throughput utilizing polarization grating.* Applied Optics, 50(17):2636–2639, 2011.

[24] D. A. B. Miller. *Device Requirements for Optical Interconnects to Silicon Chips.* Proceedings of the IEEE, 97(7):1166–1185, 2009.

[25] Berkehan Ciftcioglu, Rebecca Berman, Shang Wang, Jianyun Hu, Ioannis Savidis, Manish Jain, Duncan Moore, Michael Huang, Eby G. Friedman, Gary Wicks, and Hui Wu. *3-D integrated heterogeneous intra-chip free-space optical interconnect.* Optics Express, 20(4):4331–4345, 2012.

[26] I. M. Vellekoop and C. M. Aegerter. *Focusing light through living tissue.* Proceeding SPIE, 7554:755430, 2010.

[27] Chao Geng, Xinyang Li, Xiaojun Zhang, and Changhui Rao. *Coherent beam combination of an optical array using adaptive fiber optics collimators.* Optics Communications, 284(24):5531–5536, 2011.

[28] Chao Liu, Lifa Hu, Zhaoliang Cao, Quanquan Mua, and Li Xuan. *Modal prediction of atmospheric turbulence wavefront for open-loop liquid-crystal adaptive optics system with recursive least-squares algorithm.* Optics Communications, 285(3):238–244, 2012.

4

Silicon Photonics

"Combining silicon heterogeneously with other materials will lead to applications that we can only dream of today, or we cannot even envision yet." (Pieter Dumon et. al. [1]).

In this chapter a brief overview of silicon photonics with the main focus on the elements needed for OPA technology is presented. It is not the purpose to provide the reader an in-depth overview of silicon photonics, but to explain the basic principles and processes that are used throughout this work. An in-depth introduction to silicon photonics, related breakthroughs and prospects can be found in several review papers [2, 3] and books [4, 5].

Photonic integration has been under investigation for several decades with the main goal to introduce a similar evolution that electronics has undergone. Integration means scaling down in size. This offers several advantages in terms of performance and power consumption. A similar improvement of photonic functions is expected through integration: higher data rates of integrated detectors, lower power consumption, improved sensing, all-optical functions and reduced cost if mass-production is possible. It is thus clear why integration is important [6]. Instead of looking at improved performance, there is also a large advantage by looking into integrated components for sensing that do not compete with state-of-the art lab equipment, but that can perform the task they were designed for at a low cost for mass use by the general public.

Electronics has undergone a tremendous development to keep up with Moore's law, i.e., doubling the transistor density every 18 months [7, 8]. But while electronics is mainly based on silicon, there are a multitude of platforms for photonics: InP, GaAs, Si, glass-based, electro-optic materials, quantum dots and combinations of these platforms, each with its advantages and disadvantages. This makes integrated photonics a very rich research area, but a more complex platform to follow a similar law as in electronics. There is not one platform that — without doubt — outperforms the other, as has been the case for silicon in electronics.

There is, however, a strong rationale to use silicon as preferred integrated photonics platform. First of all, silicon is transparent in the telecom region for wavelengths larger than 1.1 μm, while detectors can be made by incorporating Ge and modulators are fabricated by heating or doping the silicon. Second, silicon, and more specifically SOI (Silicon-On-Insulator) has a high index contrast (n_{Si}=3.47) compared to silica (n_{SiO_2}=1.44) or air (n_{air} = 1.0). This allows a size reduction of a factor 100 compared to glass based integrated circuits and a factor 10 compared to III-V based integrated circuits. Third, by making use of the same platform as used in electronics, the very advanced fabrication technology developed by the CMOS industry can be used. It also enables the integration of photonics and electronics onto the same chip. Luxtera has shown such an integrated platform where photonics and electronics are fabricated in the same layer [9]. 3D stacking approaches allow further and more compact integration.

These factors clearly show the potential of silicon photonics. It can result in a multitude of new devices, improved performances, faster data rates, sensing components, etc. This has spurred a lot of interest from governments and companies resulting in large investments from the year 2000 onwards and several breakthroughs related to low-loss nanophotonic waveguides, grating couplers, filters, integrated detectors, lasers and modulators.

There is one main drawback in silicon: there is no efficient way of generating light using silicon, as it has an indirect bandgap. Fabrication of an integrated (preferably electrically pumped) laser is the holy grail of silicon photonics. Many researchers have tried to generate light in silicon by integrating rare-earth dopants, band-gap engineering (e.g., Ge-on-Si strain-based [10]), non-linear processes (e.g., Raman laser developed by Intel [11]), but as to date no efficient electrically pumped silicon laser has been demonstrated. This problem is tackled by either using an external laser or by integrating III-V (or other active) materials on silicon by molecular or BCB (benzocyclobutene) bonding.

Careful investigation of all the functionality silicon photonics has to offer shows the rationale of using it in OPA technology. Grating couplers can act as light emitting elements sending light off-chip, integrated modulators offer the possibility to tune the phase of the emitted light, while (hybrid) integrated lasers

and detectors can act as source and detector in an OPA link. Very small high-index contrast waveguides furthermore allow to route light on-chip.

Next, the process flow of the silicon photonics platform that has been used throughout this work is discussed. In Section 4.2, the basic components used in the fabrication of the OPAs discussed in Chapter 6 are given. A conclusion is finally formulated in Section 4.3.

4.1 Process flow

One of the hurdles to overcome in developing silicon photonics circuits are the costs related to fabricating these components. A lot of research in silicon has been done using e-beam lithography. This is typically a smaller scale lithography process than optical lithography, but can offer very high precision. The main drawback is that the lithography pattern is written in a step-by-step way which takes a long time. While this is an excellent tool in a research, or high-end market environment, the fabrication is expensive as this is a low volume production.

Deep-UV steppers on the other hand can make >135 wafers/hour where each wafer consists of several hundred integrated circuit (ICs). This incredible production capacity allows mass-production, but also results in very high development costs. When used in research, one is usually not interested in thousands of PICs (Photonic Integrated Circuits), except for uniformity and repeatability studies or when a post-processing process needs to be developed. However, the cost to develop one wafer only differs marginally from the cost to develop a complete lot of typically 25 wafers, as each process step comes with a very high fixed cost unrelated to the number of wafers.

To spread the production costs, MPW (Multi Project Wafer) shuttle runs have been offered since 2004 through ePIXfab [12]. Combining several designs of different research groups into one large maskset results in cost-sharing, bringing this expensive technology in reach of research groups. To ensure process repeatability and uniformity, standardized process steps are offered. The OPAs fabricated in this work rely heavily on the *standard passives technology* of this platform of which the details are explained below.

More advanced fabrication steps have been added later by incorporating an extra poly-Si layer on top of the grating to increase their efficiency [13]. Finally carrier based modulators and integrated heaters have recently been developed in this platform. For more information, we refer to [12].

Imec's standard passives process (ePIXfab)

The PICs in the standard passives run are processed on a 200mm SOI wafer from SOITEC [14] with a 2 μm buried oxide layer and a 220 nm top layer. Two etch steps are used in the standard passives process using deep-UV 193 nm lithography. The fabrication details can be found in [15]. There is one full etch of 220 nm that allows fabricating strip waveguides, deep etched gratings and an etch of 70 nm to fabricate rib waveguides, taper sections and gratings as can be seen schematically in Figure 4.1.

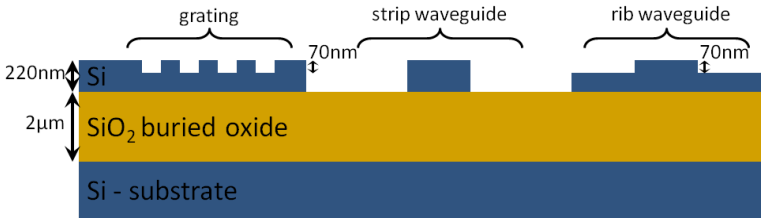

Figure 4.1: SOI process flow: an etch of 220 nm and 70 nm allows us to fabricate a.o., gratings, strip and rib waveguides.

4.2 Basic components

This section gives a brief overview of the components used in this work. In Chapters 5 and 6, designs are presented that are composed of several of these components.

4.2.1 Integrated waveguides

The key functionality of a photonic waveguide is its ability to guide light. Optical fibers for example are a well-established propagation medium due to their low propagation losses of 0.2 dB/km [16]. On an integrated platform, losses are typically higher. The propagation losses for a 450 nm wide, 220 nm high strip waveguide on SOI (fabricated with the process flow discussed above), shown in Figure 4.2 is between 2-3 dB/cm with bend losses of less than 0.01 dB/90° bend for a 5 μm radius [15].

The main loss factor is attributed to scattering losses at the edges of the strip waveguide. By using rib waveguides, this can be reduced by an order of magnitude to 0.272 dB/cm. Using a rib-strip waveguide transition, sharp bends can be obtained [17, 18]. The sidewall roughness also introduces phase errors. In the delay lines of an AWG (Arrayed Waveguide Grating), for example, these errors result in crosstalk between the output channels: because the phases of

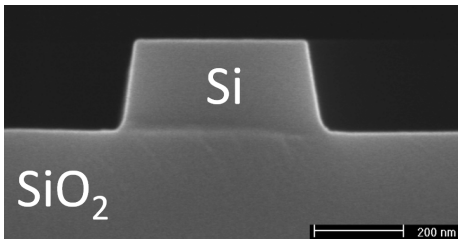

Figure 4.2: SEM picture of an integrated strip waveguide on SOI [15].

all the contributions of the delays lines are distorted, part of the light will focus on the wrong output channels in the free-propagation region, resulting in crosstalk. For this reason, the strip delay lines are widened to 800 nm to reduce the phase error. Phase errors also play an important role in the OPAs fabricated on SOI as discussed in Chapter 6. As phase control is vital for an OPA, the waveguides that guide the light to the light emitting elements (being the grating couplers discussed below) need to have a fixed phase. Phase errors should thus be avoided in these access waveguides. When using these widened waveguides, only a short tapering is needed to adiabatically taper to 450 nm which is needed to take sharp bends while maintaining the single mode condition.

4.2.2 Grating couplers

A lot of research has been done in the development of grating couplers, mainly to couple light from an optical fiber into an integrated circuit [19–22]. Here, our main interest lies in the properties of these gratings when coupling to free space. A grating consists of a periodic structure that will diffract the light. Due to the periodic nature of these diffraction events, constructive interference will occur in certain directions, described by the grating equation. A simple approach to look at these grating couplers is by using Bragg theory of periodic media.

The Bragg condition for periodic media dictates that the k-vector of the diffracted light $\mathbf{k}_{out}$ from a periodic medium equals the sum of the k-vector of the incident light $\mathbf{k}_{in}$ with an integer times the k-vector of the periodic medium $\mathbf{K}$:

$$\mathbf{k}_{out} = \mathbf{k}_{in} + q\mathbf{K}, \tag{4.1}$$

with q an integer. When the grating is wide (i.e., in the out-of-plane direction of Figure 4.3), the problem is actually a 2D problem and the grating can be described by a one dimensional grating. Having such a 1D grating with period Λ_{gr}, the grating k-vector is:

$$\mathbf{K} = \frac{2\pi}{\Lambda_{gr}}\mathbf{s}_x, \tag{4.2}$$

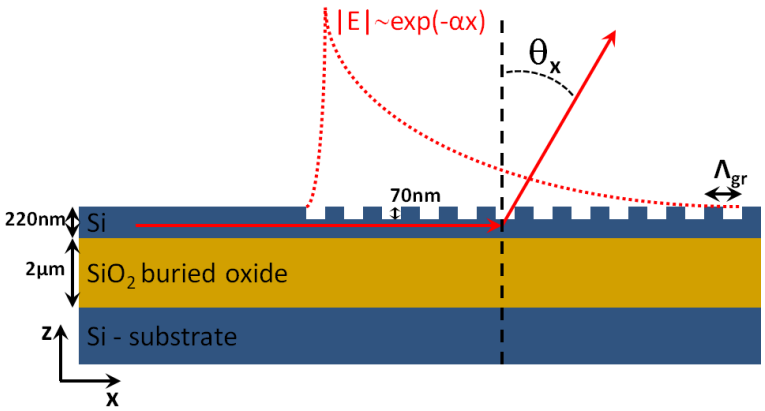

Figure 4.3: Cross-sectional view of a grating coupler.

with $\mathbf{s}_x$ the unity vector along the x-direction. Since there is no periodicity in the z-direction, there is a continuum of grating k-vectors that can be added in the z-direction. The Bragg condition is best understood using a k-vector diagram.

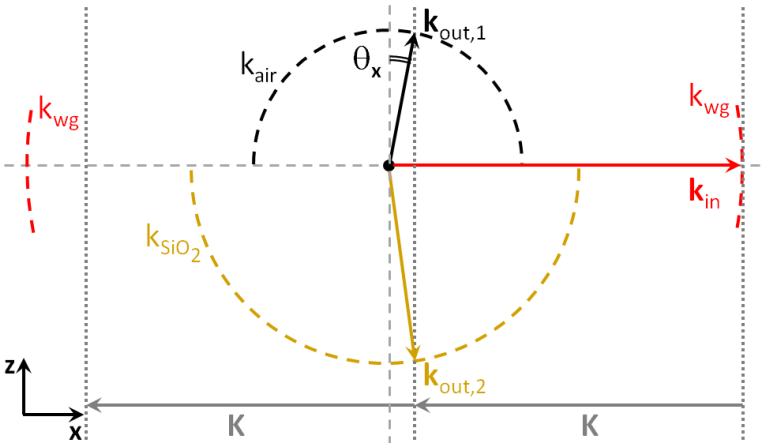

Figure 4.4: Bragg condition for a grating coupler using a k-vector diagram.

Figure 4.4 shows the such a k-vector diagram. The diagram is drawn to scale for a grating period of 630 nm. This is the period of standard grating couplers used throughout this work. The incoming light, traveling in the positive x-direction, feels an effective index $n_{eff,gr}$, being the effective index of the fundamental mode in the grating. The magnitude of the wavevector inside the grating is denoted by k_{wg}. This effective index is only felt for light traveling inside the waveguide, so only in the positive or negative x-direction. Light that would

couple upwards feels an index of air ($n_{air} = 1$), therefore a circle is drawn with radius k_{air}, being the size of a wavevector in air, while light coupling downwards feels the buried oxide index ($n_{SiO_2} = 1.44$), and thus a circle is drawn with radius k_{SiO_2}.

To find the diffracted light directions, we need to add an integer times the wavevector of the grating, denoted as **K**, while we can add any k-vector in the z-direction. Therefore vertical lines are drawn in Figure 4.4, spaced a distance |**K**| in the x-direction. The diffracted light should lie on one of these lines. Only the intersection of these lines with the circles are then viable solutions. One can see one beam diffracted upwards, $\mathbf{k}_{out,1}$ and one beam diffracted downwards, $\mathbf{k}_{out,2}$.

Such a k-vector diagram gives clear insight in what direction light can be diffracted. Suppose we want to make a first-order reflector. The k-vector of the grating **K** then needs to be twice the k-vector in the incident light $\mathbf{k}_{in}$. There is then only one solution to the Bragg condition.

$$|\mathbf{K}| = 2|\mathbf{k}_{in}| \tag{4.3}$$

$$\frac{2\pi}{\Lambda_{gr}} = 2n_{eff,gr}\frac{2\pi}{\lambda} \tag{4.4}$$

$$\Lambda_{gr} = \frac{\lambda}{2n_{eff,gr}}. \tag{4.5}$$

For a second order reflector, the k-vector of the grating **K** is equal to the k-vector in the incident light $\mathbf{k}_{in}$. When two grating k-vectors **K** are then added to the incident light k-vector, we get a reflector, hence the name second-order reflector. There is also another solution. When only one grating k-vector **K** is added, light can couple out perpendicularly. This vertical out-coupling is however less efficient due to the second order reflection, therefore near-vertical coupling is used as shown in Figure 4.4. These are still called second-order gratings, of which the out-coupled light is the first-order diffracted light. These second-order gratings couple light out at an angle θ_x, given by the grating equation:

$$\sin\theta_x = \frac{\Lambda_{gr}n_{eff,gr} - \lambda}{n_{bg}\Lambda_{gr}}, \tag{4.6}$$

with $n_{eff,gr}$ the effective index of the grating area, n_{bg} the refractive index of the background material and Λ_{gr} the grating period.

While the Bragg condition dictates the direction of the diffracted light, is says nothing about the efficiency of these diffracted beams. This efficiency is determined by the refractive index profile. The downward component can for example be reduced by adding a silicon overlay on the grating [13]. Part of the downward component also reflects on the substrate back upwards and can interfere constructively or destructively with the upward diffracted beam, depending on the silica thickness.

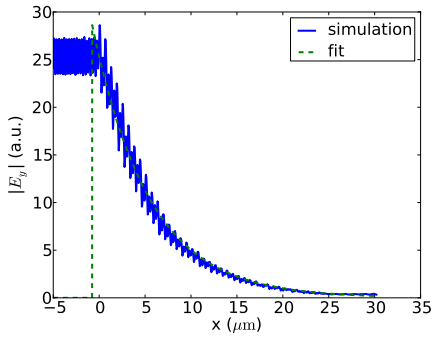

Figure 4.5: |E| field emitted by a grating coupler with a period of 630 nm, simulated with CAMFR. The dashed line shows an exponential fit. The decay length $1/\alpha = 6.2$ μm at 1550 nm.

Figure 4.3 also shows the typical behavior of the magnitude of the electric field that is coupled out. It can be well approximated by an exponential decay. In Figure 4.5, the electric field inside a grating has been simulated. The grating has a 70 nm etch depth, the period is 630 nm period and the fill factor is 0.5. These are the typical dimensions of the gratings to optimally couple 1550 nm light in an optical fiber at a 10° angle with the normal of the surface [19]. The simulation shows that there is indeed an exponential decay, with a decay length of approximately $1/\alpha = 6-7$ μm at a wavelength of 1550 nm. This decay length depends on the effective index difference of the grating elements. By having for example a very shallow etch, this difference will be small and the decay length $1/\alpha$ will be longer. As the size of the radiating aperture determines the beam width, this can be used to narrow the beam.

In the other dimension, the gratings can be modeled as a Gaussian of which the width depends on the mode width of the grating mode. This can be calculated using a mode solver such as Fimmwave [23]. For a typical 10 μm wide fiber grating coupler, the 1/e mode width is about 7.5 μm. The formalism of Chapter 3 can then be used to calculate the far-field characteristics. Figure 4.6(a) shows an SEM (Scanning Electron Microscope) image of a grating coupler array used as an OPA. More details can be found in Chapter 6.

When used as a fiber coupler, the gratings fabricated with the process flow described in Section 4.1 have an efficiency of -5.2 dB. These grating are used in this work to get light in or out of our fabricated OPA structures. Figure 4.6(b) shows an SEM image of a focusing grating coupler. Due to the focusing, there is no need for a large taper while the efficiency remains the same [24]. Using a silicon overlay to cancel the downward diffracted light, the fiber coupling effi-

ciency goes up to -1.6 dB [13]. The efficiencies of the gratings used as free-space antennas are typically higher and are discussed in Chapter 6 for the fabricated structures. They typically are of the order of -4 dB to -5 dB (30% to 40%) for a 70 nm etched grating because the modal overlap with a fiber is not needed. The efficiency drops when in Equation (4.6), the angle θ_x becomes zero. This would mean vertical out-coupling. However, for this period, the grating also acts as a second order reflector, reflecting the light back into the waveguide and decreasing the out-coupling efficiency as discussed above.

Inverted tapers are also used to transform the mode of an optical fiber to the one of an integrated waveguide. Coupling losses of less than 0.2 dB have been shown using this approach [2]. While tapers can offer low coupling loss and high bandwidth, the wafers need to be diced, polished and processed before any test can happen. Vertical grating couplers on the other hand allow wafer testing of the components and no dicing is needed. This is a major advantage when fabricating silicon chips in a commercial environment.

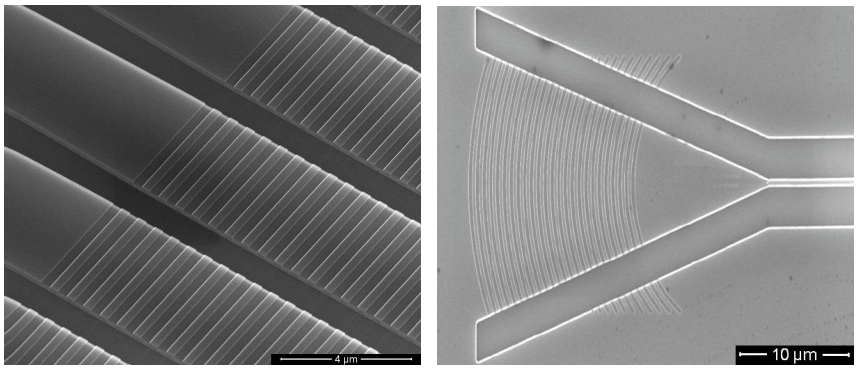

(a) (b)

Figure 4.6: SEM picture of grating couplers: (a) grating coupler array of 4 μm wide couplers spaced 5 μm with 630 nm grating period, (b) a focusing grating coupler with 630 nm grating period.

4.2.3 MMI splitter

To access the different light emitting elements, light from the input waveguide needs to be split. A 1 × 2 MMI (MultiMode Interference) splitter can symmetrically split the light into two contributions with the same phase. To split the light in N contributions, either a 1 × N-splitter can be designed or a splitter tree can be used. The latter approach was used in this work. One basic 1 × 2 splitter then needs to be used. Two types of splitters are available. A deep etched MMI that

only uses the 220 nm etch or a shallow etched MMI which uses a combination of the 220 nm deep and 70 nm shallow etch. The latter makes the MMI splitter somewhat larger, but increases the simulated efficiency from 86% to 95% due to better mode matching. Figure 4.7 shows an SEM picture of a shallow etched MMI.

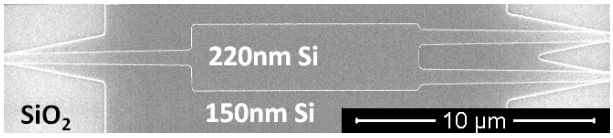

Figure 4.7: SEM picture of a shallow etched MMI.

4.2.4 Star coupler

A star coupler can be used as an alternative approach to split light into different branches. Light goes through a free propagation region to split it into different elements. The free propagation region imposes a natural Gaussian envelope over all the elements. Using a shallow tapering approach, the mode mismatch between the single mode waveguide and free propagation region can be made small to reduce the insertion loss of the star coupler. The insertion loss is typically around 1.1 dB [25, 26].

Figure 4.8 shows a 9×16 star coupler. The free propagation region, shallow etched and deep etched strip waveguides are indicated. The tapering between the shallow and deep etched waveguides is visible as well. When using the central (5th) input waveguide, light will be split in 16 elements with equal phase. By using a different input waveguide, a phase difference will be imposed on the elements. This is useful in beam steering applications as discussed in Chapter 6. The tiling indicated in Figure 4.8 has no influence on the star coupler behavior but is used for etch uniformity purposes.

4.2.5 Modulators

Modulators are dealt with in Chapter 5.

4.3 Conclusions

Silicon photonics offers several of the key functionalities needed in OPA technology. Very small, sub-micrometer size light radiating elements can be fabricated, light can be routed to these elements using integrated waveguides, and using phase tuners, the phase can be adjusted so adaptive steering is possible.

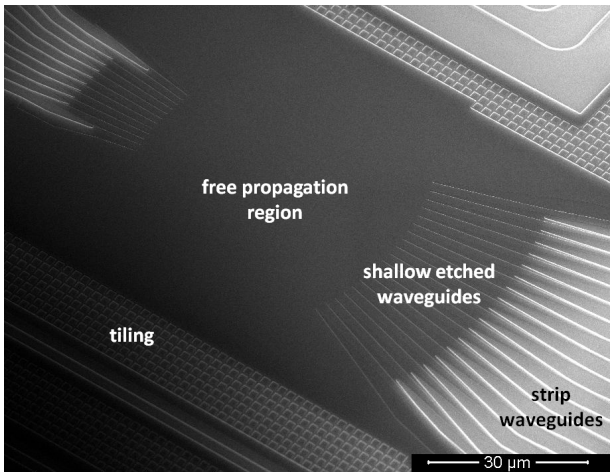

Figure 4.8: SEM picture of a star coupler.

Furthermore, the platform allows to use integrated detectors using Ge. The only problem is the light generation. Using a hybrid approach, lasers can be fabricated, or an external laser can be used, depending on the needed functionality. One major advantage of these integrated OPAs is that light is captured in a single mode waveguide. On-chip interferometry can then be used for sensing applications [27, 28], while coherent detection is possible to increase the sensitivity roughly by two orders of magnitude [16].

References

[1] Pieter Dumon, Wim Bogaerts, Roel Baets, J.-M. Fedeli, and L. Fulbert. *Towards foundry approach for silicon photonics: silicon photonics platform ePIXfab.* IEEE Electronics, 45(12), 2009.

[2] B. Jalali and S. Fathpour. *Silicon Photonics.* IEEE Journal of Lightwave Technology, 24(12):4600 –4615, 2006.

[3] Richard Soref. *The Past, Present, and Future of Silicon Photonics.* IEEE Journal of Selected Topics in Quantum Electronics, 12(6):1678 –1687, 2006.

[4] Lorenzo Pavesi and David J. Lockwood. *Silicon Photonics.* Springer, 2004.

[5] Graham T. Reed and Andrew P. Knight. *Silicon Photonics: an introduction.* John Wiley and Sons, 2004.

[6] Roel Baets, Pieter Dumon, Wim Bogaerts, Gunther Roelkens, Joris Van Campenhout, Dirk Taillaert, Joost Brouckaert, Katrien De Vos, Joris

Roels, Shankar Selvarja, Frederik Van Laere, Peter Bienstman, and Dries Van Thourhout. *Silicon photonics*. International Symposium on VLSI Technology, Systems and Applications, 2007. VLSI-TSA 2007., pages 1–3, 2007.

[7] R.R. Schaller. *Moore's law: past, present and future*. IEEE Spectrum, 34(6):52–59, 1997.

[8] Gordon E. Moore. *Cramming more components onto integrated circuits*. Electronics, 38(8):114, 1965.

[9] Luxtera. *Illuminating the path to terabit IC connectivity*. http://www.luxtera.com/, 2012.

[10] Jifeng Liu, Xiaochen Sun, Rodolfo Camacho-Aguilera, Lionel C. Kimerling, and Jurgen Michel. *Ge-on-Si laser operating at room temperature*. Optics Letters, 35(5):679–681, 2010.

[11] H. Rong, A. Liu, R. Jones, O. Cohen, D. Hak, R. Nicolaescu, A. Fang, and M. Paniccia. *An all-silicon Raman laser*. Nature, 433:292–294, 2005.

[12] ePIXfab. *The silicon photonics platform*. http://www.epixfab.eu/, 2011.

[13] D. Vermeulen, S. Selvaraja, G. Verheyen, P. Lepage, W. Bogaerts, and G. Roelkens. *High-efficiency Silicon-On-Insulator Fiber-to-Chip Grating Couplers Using a Silicon Overlay*. In 6th International Conference on Group IV Photonics (GFP 2009), page FPd1, San Fransisico, California, 2009.

[14] SOITEC. *SOITECs Unibond(R) process*. Microelectron. J, 27(4/5):R36, 1996.

[15] S. K. Selvaraja, P. Jaenen, W. Bogaerts, D. Van Thourhout, P. Dumon, and R. Baets. *Fabrication of Photonic Wire and Crystal Circuits in Silicon-on-Insulator Using 193-nm Optical Lithography*. Journal of Lightwave Technology, 27(18):4076–4083, 2009.

[16] P. G. Agrawal. *Fiber-Optic Communication Systems*. John Wiley and Sons, Inc, 2002.

[17] Shankar Kumar Selvaraja, Wim Bogaerts, Philippe Absil, Dries Van Thourhout, and Roel Baets. *Record Low-Loss Hybrid Rib/Wire Waveguides for Silicon Photonic Circuits*. In 7th International Conference on Group IV Photonics (GFP 2010), pages post–deadline, Beijing, China, 2010.

[18] Wim Bogaerts and S. K. Selvaraja. *Compact Single-Mode Silicon Hybrid Rib/Strip Waveguide With Adiabatic Bends*. IEEE Photonics Journal, 3(3):422–432, 2011.

[19] D. Taillaert. *Grating Couplers as Interface Between Optical Fibres and Nanophotonic Waveguides.* UGent, PhD Thesis, 2006.

[20] G. Roelkens, D. Van Thourhout, and R. Baets. *High efficiency grating coupler between silicon-on-insulator waveguides and perfectly vertical optical fibers.* Optics Letters, 32(11):1495–1497, 2007.

[21] G. Roelkens, D. Vermeulen, D. Van Thourhout, R. Baets, S. Brision, P. Lyan, P. Gautier, and J. M. Fedeli. *High efficiency diffractive grating couplers for interfacing a single mode optical fiber with a nanophotonic silicon-on-insulator waveguide circuit.* Applied Physics Letters, 92(13):131101, 2008.

[22] S. Scheerlinck. *Metal grating and polymer based coupling components for photonic integrated circuits.* UGent, PhD Thesis, 2008.

[23] Photon Design. *Fimmwave.* http://www.photond.com/products/fimmwave.htm/, 2011.

[24] F. Van Laere. *Fotonische geïntegreerde circuits en vezelkoppelaars gebaseerd op InP gebonde membranen, Photonic Integrated Circuits and Fibre Couplers Based on InP Bonded Membranes.* UGent, PhD Thesis, 2009.

[25] P. Dumon, W. Bogaerts, D. Van Thourhout, D. Taillaert, R. Baets, J. Wouters, S. Beckx, and P. Jaenen. *Compact wavelength router based on a silicon-on-insulator arrayed waveguide grating pigtailed to a fiber array.* Optics Express, 14(2), 2006.

[26] W. Bogaerts, S. Selvaraja, P. Dumon, J. Brouckaert, K. De Vos, D. Van Thourhout, and R. Baets. *Silicon-on-Insulator Spectral Filters Fabricated with CMOS Technology.* Journal of Selected Topics in Quantum Electronics, 16(1):33–44, 2010.

[27] G. Yurtsever, P. Dumon, W. Bogaerts, and R. Baets. *Integrated photonic circuit in silicon on insulator for Fourier domain optical coherence tomography.* In Proceedings of SPIE-The International Society for Optical Engineering, volume 7554, 2010.

[28] Y. Li, S. Meersman, and R. Baets. *Realization of fiber based laser Doppler vibrometer with serrodyne frequency shifting.* Applied Optics, 50(17):2809–2814, 2011.

5

Phase Tuning

One of the key elements for optical phased arrays is a way to selectively tune the phases of the different emitting elements. While in LC OPAs this is achieved through the propagation of light through a tunable birefringent material (i.e., the liquid crystal), silicon photonics offers us a multitude of possibilities to tune the phase of light. In this work, we have investigated the possibilities to fabricate OPAs on SOI. Therefore, we need to tune the phase of light in a silicon photonics integrated circuit. Typically an input waveguide is split into different waveguides (which are connected to the light emitting elements). The light in these different waveguides then needs to be tuned. Two different phase tuning approaches approaches are described in this chapter.

Depending on the needed speed and/or performance of the beam steering element, one can choose for a slow, but simple and low-cost solution such as the thermo-optic effect, which is discussed in Section 5.1. As there is a need for a continuous current flow and heat generation, such an effect is very power-hungry. A novel way to tune the phase using a Nano-Electro-Mechanical Systems (NEMS) approach has been investigated which is given in Section 5.2. The key argument here is that such a component is low-power (capacitive structure which uses only power when switching) and possibly fast (>MHz-range, depending on the mechanical relaxation constants). In Section 5.3, we touch upon other phase modulation/tuning techniques. Section 5.4 presents the main conclusions.

5.1 Thermo-optic effect

The thermo-optic (TO) effect is well-known in silicon as a simple, cheap and low-cost tuning mechanism. The refractive index of silicon has a large temperature dependent coefficient being

$$\frac{\partial n}{\partial T} = 1.86 \times 10^{-4} \mathrm{K}^{-1}, \tag{5.1}$$

making silicon photonics circuits very temperature sensitive. While this is advantageous as a tuning mechanism, the temperature stability of a silicon photonics circuit becomes an important issue. A way to reduce this temperature dependence is to add for example a polymer layer with a large — but opposite — temperature dependent coefficient [1]. In this work, we have investigated a basic heater design and characterized its speed and performance.

Next, the process flow of the heaters will be briefly explained. Afterward some simulation and experimental results on the speed and performance of the heater are given.

5.1.1 Process flow

The heaters are processed on standard SOI strip waveguides using contact-mask lithography. The process flow is summarized in Figure 5.1. The SOI sample is cleaned first by rinsing it with acetone, IPA (isopropyl alcohol or isopropanol) and DI (deionized) water, respectively (Figure 5.1(a)). Then we spin a primer (AP3000) followed by spinning a diluted BCB (benzocyclobutene) layer. The dilution and spinning speed will determine the thickness of the BCB layer. After spinning, the BCB is cured (Figure 5.1(b)). The photoresist (nLof2070, negative) is then spun, followed by a softbake (Figure 5.1(c)). An UV contact mask lithography step and postbake follows as shown in Figure 5.1(d). Figure 5.1(e) shows the structure after photoresist development; the heater pattern has been transferred to the photoresist. To increase the adhesion of the metal with the BCB, the structure is placed in an oxygen plasma etch for about one minute which roughens the BCB layer (Figure 5.1(f)). In the final two steps, metal is deposited (Figure 5.1(g)) followed by lift-off (Figure 5.1(h)). The metal consists of a 100 nm Ti layer and a 20 nm Au layer. This specific stack was chosen for two reasons. Firstly, the gold prevents oxidation of the Ti. Secondly, the resistivity, and thus the voltage-current relation, is changed by almost an order of magnitude in order to comply with the measurement hardware limitations (maximum current and voltage) discussed in Chapter 6.

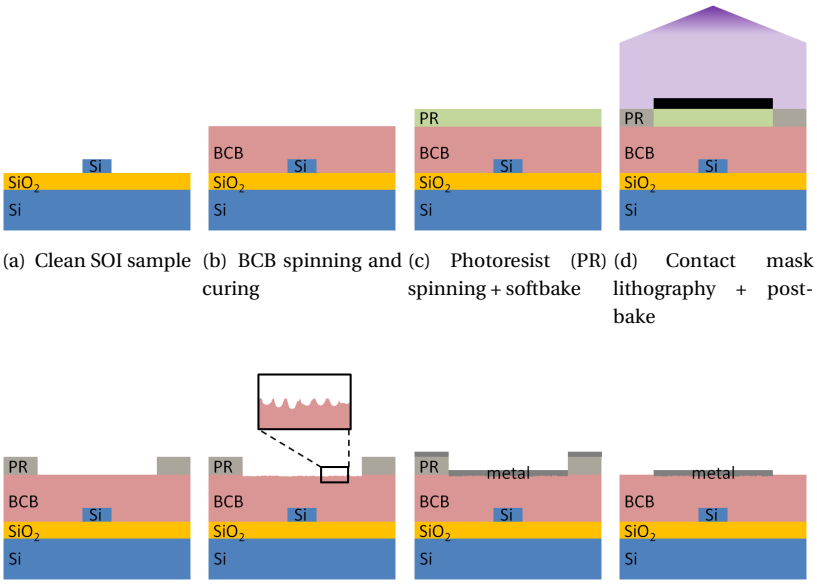

(a) Clean SOI sample (b) BCB spinning and curing (c) Photoresist (PR) spinning + softbake (d) Contact mask lithography + post-bake

(e) Photoresist development (f) Oxygen plasma etch (g) Metal deposition (h) Lift-off

Figure 5.1: Heater process flow.

Processing artifacts

Some processing artifacts arise resulting in a not nice rectangular cross section of the heater as shown schematically in Figure 5.2. After development of the photoresist, the profile is slightly slanted. Depending on the slope of the photoresist, the heater width will be larger than the designed width on the contact mask. This profile is needed for a successful lift-off. When metal is then deposited on the structure, the shadowed area will have a gradually decreasing thickness resulting in a non-uniform cross section. At the corner there is furthermore a build-up of metal which results in upstanding edges after photoresist removal. Optimizing the photoresist profile and the metal deposition process can remove these artifacts. The impact on the heater performance is however minimal.

5.1.2 Resistivity

To measure the resistance of the heaters, several test structures were fabricated. A large sweep of heater widths and lengths were measured using a four-probe measurement with a probe card setup. The main results are summarized in Fig-

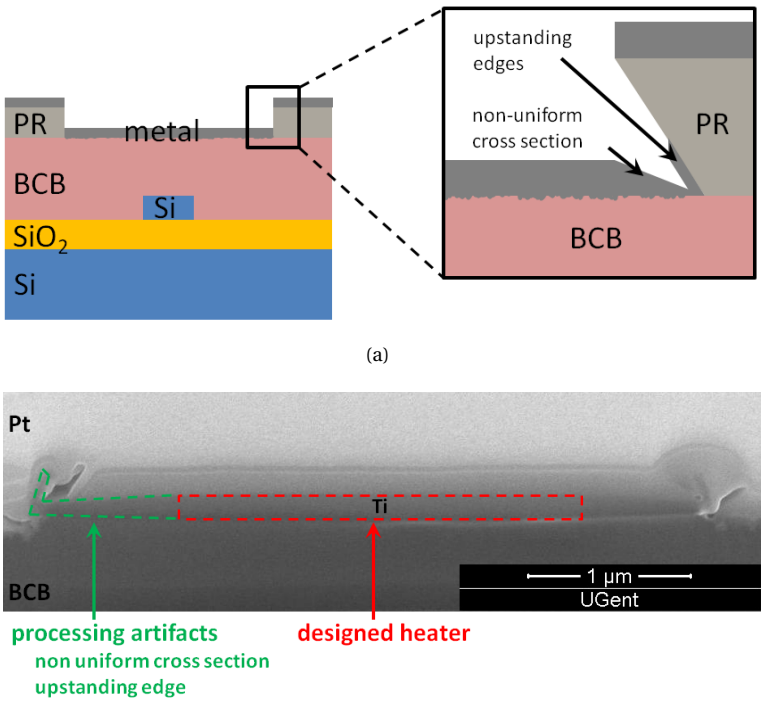

Figure 5.2: Heater processing artifacts: (a) Schematic picture, (b) SEM picture, a Pt layer is deposited on top to make a cross section.

ure 5.3, where the resistance per micrometer length of the heater is plotted as a function of the heater width. From this graph, one can immediately deduce a rough estimate for the resistance of a fabricated heater. Two different batches of samples were fabricated, one with a 120 nm Ti metal layer and one with a 100 nm Ti + 20 nm Au stack. The main result that should be noted here is that the small gold layer will reduce the resistance by almost an order of magnitude. A theoretical fit is also plotted for the 120 nm Ti layer (taking into account the non-uniform cross section) to determine the effective resistivity, which was determined to be about 1.64 $\mu\Omega$·m, about four times higher than the bulk resistivity of Ti being 0.4 $\mu\Omega$·m.

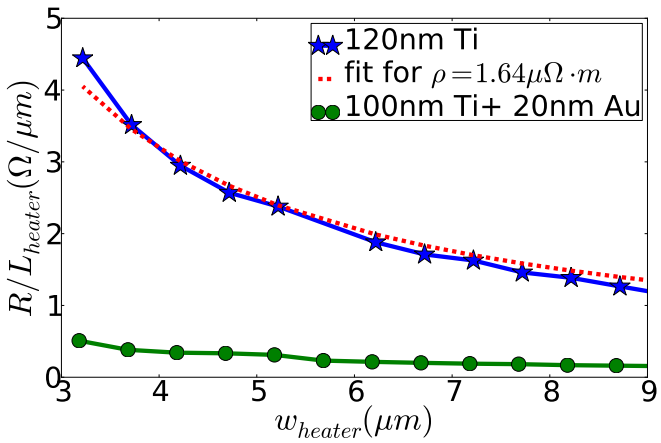

Figure 5.3: Heater resistivity for a 120 nm Ti stack layer compared to a 100 nm Ti + 20 nm Au stack. A fit to determine the resistivity of the Ti is shown as well.

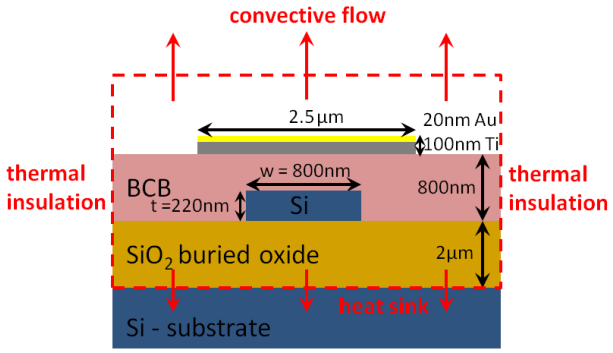

Figure 5.4: A typical heater cross section together with the thermal simulation domain indicated by the red dashed line.

5.1.3 Efficiency

Thermal simulations

The heater efficiency can be simulated using the Phoenix simulation software which consists of an optical mode solver with a thermo-optic module for thermo-optic simulations [2]. A typical heater cross section is shown in Figure 5.4, where the width of the heater is designed to be 2.5 μm but can be up to 3.5 μm due to the processing artifacts discussed in Section 5.1.1. The waveguide width is typically 800 nm. This is not the typical single mode waveguide width

of 450 nm as long delays have shown to be more tolerant to fabrication deviations and the corresponding phase errors when they are a bit wider. A width of 800 nm is therefore chosen as explained in Chapter 4.

Figure 5.4 also shows the thermal boundary conditions used. There is a convective flow to the air, the substrate acts as a heat sink and the two other sides are thermally insulated. Therefore, the simulation domain should be large enough in the horizontal direction for this boundary condition to accurately apply. Using the thermo-optic module of Phoenix, a simple thermal simulation can then be performed after which the overlap of the heat profile with the optical mode can be calculated giving us the effective index change. Then we can easily calculate the power needed for a π phase shift, denoted as P_π.

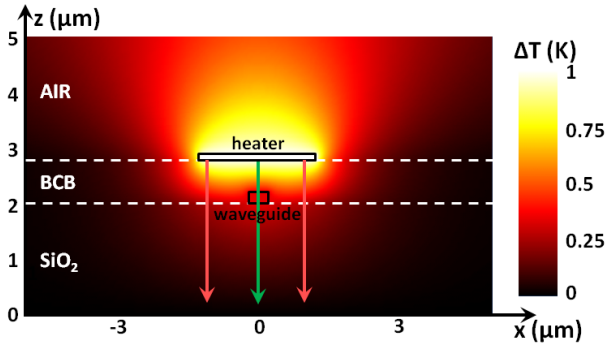

Figure 5.5: Thermal simulation of two heater designs: temperature profile (a) without insulating air trenches (P_π =11.8 mW), (b) with insulation air trenches (P_π =3.8 mW).

Figure 5.5 shows the thermal simulation for two types of heater structures with a heater width of 2.5 μm. In Figure 5.5(a), the simple cross section is used

as defined in Figure 5.4, while in Figure 5.5(b), two insulating air trenches are etched next to the heater. This increases the efficiency from P_π =11.8 mW to P_π =3.8 mW. As the heater width is not a very crucial parameter, it is more important to reduce the lateral heat spread, especially since this area is connected to the substrate which acts as a heat sink, indicated by the red arrows in Figure 5.5. It is important to reduce the thermal conductivity from the heater to the heat sink. As one might be tempted to use a better thermal conducting material than BCB (thermal conductivity = 0.3 W/mK) as intermediate layer between the heater and the waveguide, this will reduce the performance as the thermal conductivity to the substrate is then also increased. Increasing thermal conductivity and thus the heat spread of the structure will allow you to dissipate more power and thus will increase the tuning range of the heater [3], but not its efficiency. When heat is only transferred directly to the waveguide (as indicated by the green arrow in Figure 5.5), the efficiency will be improved. However, our in-house process flow does not allow to fabricate such narrow heaters. We conclude by saying that using an optimal design, the power needed for a π phase shift can be as low as a few mW.

Several heater designs have been explored in literature, where a lot of work has been done to tune microring resonators. Theoretical studies show that for a similar heater design as depicted in Figure 5.1, a power for a π phase shift of about P_π=15-20 mW is required [4, 5]. By using one lithography step to fabricate both heaters and silicon waveguides, studies show a power efficiency of P_π=4 mW due to the high confinement of the heat [6] as the heater is now as wide as the waveguide. These values correspond well to our thermal simulations.

Measurements

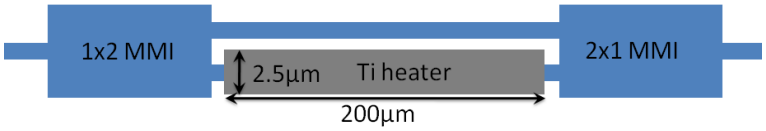

Figure 5.6: Mach-Zehnder interferometer with a heater on one arm.

The efficiency of the in-house heaters has been measured using a Mach-Zehnder Interferometer (MZI) structure. A balanced MZI structure with a heater on one arm was fabricated and measured as shown schematically in Figure 5.6. Figure 5.7 shows the optical output of the MZI as a function of the injected power in the heater. An offset is seen in the beginning, which can be attributed to the fact that the heater was slightly too close to the waveguide (BCB height ≈

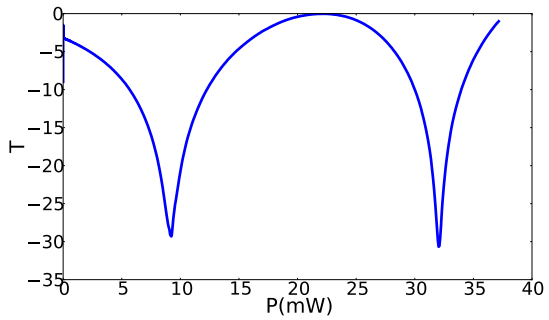

Figure 5.7: Optical output of the Mach-Zehnder interferometer as a function of the injected power into the heater on top of one arm.

800 nm). A power of about 30 mW is needed to reach again the starting point on the curve, which means we have induced a 2π phase shift bringing $P_\pi = 15$ mW. This value corresponds very well to values reported in literature as discussed below.

In [7], a CMOS compatible design is used with a ridge waveguide design, where the ridge slab is doped to form a resistor as shown in Figure 5.8(a). The power needed for a π phase shift is then about $P_\pi = 45$ mW, which is still relatively high. In [8], a similar heater design as our basic heater has been fabricated, but where silica voids were introduced to confine the heat as shown in Figure 5.8(b). The measured power for a π phase shift was $P_\pi = 12.4$ mW. Another approach taken in [9] is to integrate NiSi based heaters on the SOI structure shown in Figure 5.8(c). Power needed is about $P_\pi = 20$ mW. All these reported values agree well with our in-house fabricated heaters.

5.1.4 Speed

The switching speed of heaters is determined by the thermal constants of the structure, which are usually in the μs range. The speed of our in-house heater has been measured using the MZI structure (Figure 5.6). Figure 5.9 shows the output of the MZI when driven with a 20 kHz voltage signal where the peak voltage corresponds to a π phase shift. The 10%-90% rise and fall time were measured to be 12.7 μs and 7.2 μs, respectively. The speed is determined by the time the heat needs to spread out. So improving this heat spread will increase the speed, but reduce the efficiency. In [10], the rise and fall times could be reduced from around 30 μs to 700 ns using a differential control method.

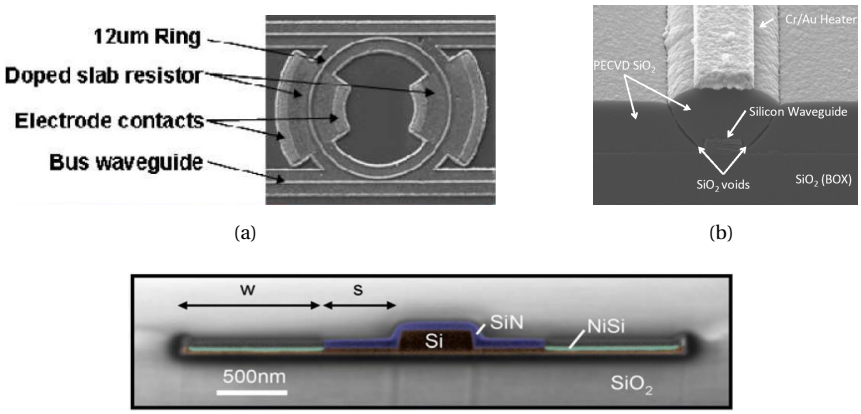

(a) (b)

(c)

Figure 5.8: Different heater designs: (a) doping slab of a ridge waveguide [7], (b) insulation trenches [8], (c) NiSi based heater [9].

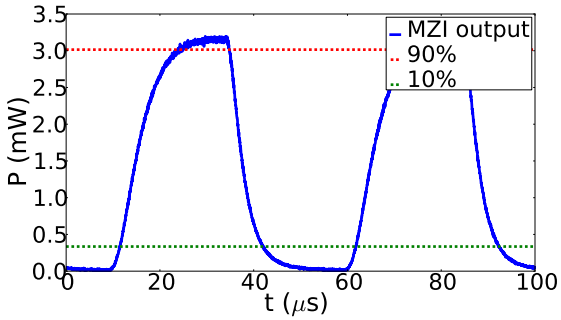

Figure 5.9: Dynamic behavior of the heater. The output of a balanced Mach-Zehnder interferometer is shown where one arm is heated. The heater is driven by a 20 kHz voltage signal which gives a π phase shift at the peak voltage.

5.1.5 Crosstalk

Crosstalk is of importance when several heaters are placed close to each other. Figure 5.10 shows the simulated power [2] needed for a π phase shift as a function of a lateral offset of the heater, where the heater width is 2.5 μm as shown in Figure 5.4. As soon as the heater is no longer above the waveguide (offset >1.25 μm) an exponential increase of the needed power can be seen where the fit shows an increase of 2.8 dB/μm offset. For a 10 μm offset, the needed power increases with 25 dB which is a figure for the crosstalk. This is the minimum

spacing used for the heaters in Chapter 6.

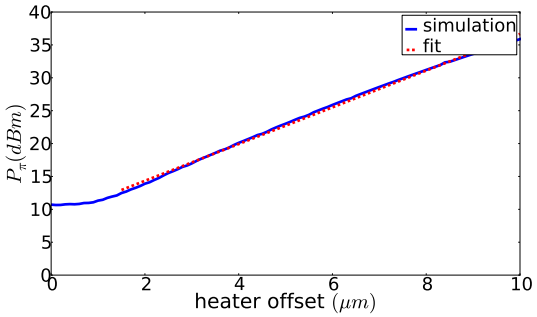

Figure 5.10: Heater crosstalk: the power needed for a π phase shift is shown as a function of a lateral offset of the heater. A linear fit is shown as well as the red dashed line.

5.2 Nano-Electro-Mechanical Systems approach

Apart from its attractive optical properties, crystalline silicon also has good mechanical properties. This stimulated a rapid development of the NEMS field in e.g., fabricating ultra sensitive sensors [11]. This platform furthermore allowed to observe and measure optical forces [12–14]. The principle of using a free-standing slot waveguide as phase modulator was already explained in [15], but here we present to our knowledge the first experimental demonstration.

As a mechanical motion can induce a very large effective index shift, compared to other techniques such as heating, carrier injection/depletion, electro-optic effect, ...we can have an ultra small phase tuner. The proposed structure works capacitively and thus only power will be consumed when switching. The speed will depend on the mechanical relaxation constants of the structure, which will be in the MHz range for a typical free-standing waveguide.

In the next section, the working principle of the slot waveguide is explained. Section 5.2.2 gives a mathematical description together with some simulation results. Section 5.2.3 presents the device layout, followed by the measurement setup and results in Section 5.2.4.

5.2.1 Principle

The principle of phase modulation is based on the fact that the effective index of a slot waveguide will change by changing the slot width. The effective index

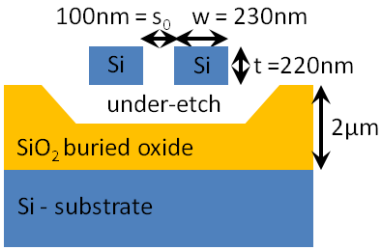

Figure 5.11: Cross section of an under-etched slot waveguide.

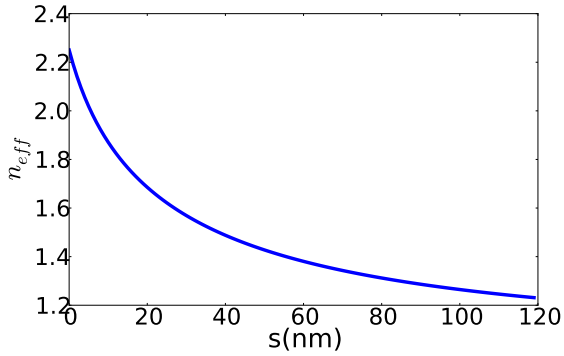

Figure 5.12: Effective index of the fundamental TE-like mode of the slot as a function of slot width at a wavelength of 1550 nm with an air cladding.

of the fundamental TE-like mode of the slot waveguide (Figure 5.11) as a function of the slot width *s* was calculated using the Fimmwave mode solver [16] and can be found in Figure 5.12. A large change in effective index occurs as the slot width becomes smaller. The slot width can be changed by under-etching the slot waveguide and applying a voltage over the slot. The structure can then be considered as a capacitor. By applying a voltage across the slot it is well known that the beams (plates of a charged capacitor) will attract each other. By increasing the voltage, the beams are attracted and the slot width becomes smaller. This increases the attractive force even more. At a certain point, the attractive force becomes too large for the slot to be countered by the elastic force and the system becomes unstable resulting in a collapse of the slot waveguide. This is known as the 'pull-in' effect in the MEMS (Micro-Electro-Mechanical Systems) world and occurs when the slot deviation is larger than one third of the nominal width. The slot waveguide is placed in a Fabry-Pérot cavity which allows us to measure the phase change by means of a spectral shift of the resonance

wavelengths of the cavity.

5.2.2 Mathematical description

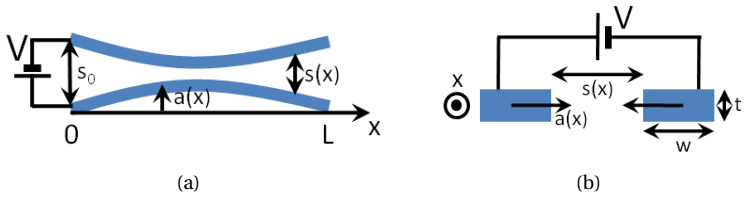

Figure 5.13: Mathematical description of the slot waveguide based phase modulator: (a) top view, (b) cross sectional view.

Figure 5.13 shows a top view and cross sectional view of the slot waveguide in which all the variables introduced below are denoted. The mathematical model described below is explained in greater detail in [17]. The movement $a(x)$ of the beams of the slot can be described by the Euler beam equation, where the residual axial stress is neglected in first instance:

$$EI\frac{\mathrm{d}^4 a}{\mathrm{d}x^4} = p(x), \tag{5.2}$$

where E is Young's modulus (= 169 GPa in Si for the crystallographic direction of interest), $p(x)$ is the force distribution along the beam and I is the beam's area moment of inertia. In the direction of interest I is defined as:

$$I = \frac{tw^3}{12}, \tag{5.3}$$

with w and t the width and thickness of the beam, respectively. When a voltage is applied across the slot, a force will be exerted on both beams which will depend on the width of the slot waveguide. The force distribution $p(x)$ (N/m) can be expressed as:

$$p(x) = \frac{1}{2}V^2\frac{\partial C[s(x)]}{\partial s(x)}, \tag{5.4}$$

where V is the applied voltage and $C[s(x)]$ is the capacitance distribution (F/m) across the slot, which is a function of $s(x)$, the slot width. The capacitance distribution is given by:

$$C[s(x)] = \epsilon_0\frac{t}{s(x)}. \tag{5.5}$$

The magnitude of the force distribution is then given by:

$$p(x) = \frac{1}{2}V^2\frac{\epsilon_0 t}{s(x)^2}, \tag{5.6}$$

with ϵ_0 the vacuum permittivity. There is a squared dependence on the applied voltage and inverse squared dependence on the slot width. This slot width is dependent on the beam excursion $a(x)$ as:

$$s(x) = s_0 - 2a(x), \tag{5.7}$$

where s_0 is the slot width when no voltage is applied. Inserting (5.7) in (5.6) and (5.6) in (5.2), we get the following nonlinear differential equation:

$$EI\frac{\mathrm{d}^4 a}{\mathrm{d}x^4} = \frac{1}{2}V^2\frac{\epsilon_0 t}{[s_0 - 2a(x)]^2}. \tag{5.8}$$

Different boundary conditions can be used. Fixed boundary conditions at the clamping points $x = 0$ and $x = L$ allow no displacement or rotation:

$$a = 0; \frac{\mathrm{d}a}{\mathrm{d}x} = 0. \tag{5.9}$$

Hinged boundary conditions allow no displacement, but do allow rotation at the clamping points. The boundary conditions become:

$$a = 0; \frac{\mathrm{d}^2 a}{\mathrm{d}x^2} = 0. \tag{5.10}$$

Equation (5.8) is solved numerically for fixed boundary conditions using the parameters given in Figure 5.11. In Figure 5.14, the beam excursion of one of the slot beams with a length of $L = 10$ μm is shown as a function of x for different voltages. When the voltage becomes larger than the 'pull-in' voltage, the system becomes unstable and no solution is found. For $L = 10$ μm, the pull-in voltage was determined to be around 11.5 V.

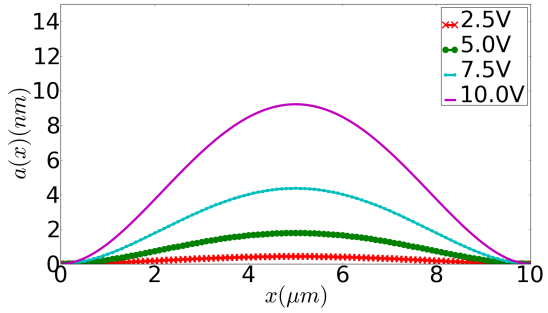

Figure 5.14: Beam excursion of one of the beams as a function of x for different applied voltages.

When the beam excursion is known, the phase change can be calculated as:

$$\Delta\phi = \frac{2\pi}{\lambda}\int_0^L n_{eff}[s_0 - 2a(x)]\mathrm{d}x, \tag{5.11}$$

with λ the wavelength of light and $n_{eff}[s(x)]$ is given by Figure 5.12. Figure 5.15 shows the phase change as a function of applied voltage for different lengths of the beams. The phase change increases more sharply for larger voltages up to the point where 'pull-in' occurs. One can see that for longer beams, the effect becomes large for a small voltage.

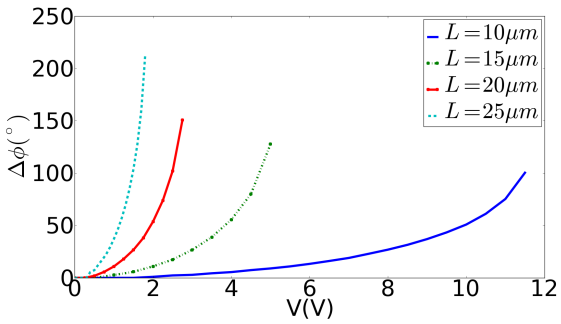

Figure 5.15: Theoretically predicted phase change as a function of applied voltage across the slot for different lengths L. The curves are drawn up to the point where 'pull-in' occurs.

While the effect becomes larger for longer beams, so does the mechanical relaxation time. The speed of the system is limited by the mechanical resonance frequency of the beams. The fundamental resonance frequency f_0 of such a beam is given by [17]:

$$f_0 = \frac{1}{2\pi}\frac{p^2}{L^2}\sqrt{\frac{EI}{\rho S}}, \tag{5.12}$$

with $p = 4.730$ for fixed boundary conditions and $p = \pi$ for hinged boundary conditions, L the length of the beam, I the moment of inertia given by (5.3), E Young's modulus, ρ the mass density of silicon ($\rho = 2.3290$ g·cm^{-3}) and S the beam cross section. Note the inverse L^2 dependence, meaning that using a shorter beam results in an increase of the resonance frequency. Figure 5.16 shows the fundamental resonance frequency as a function of beam length. High speed (>100MHz) can be obtained by using short free-standing structures. One way to get a large effects while keeping a high speed is to use a cascade of short under-etched structures as is discussed in Section 5.2.4.

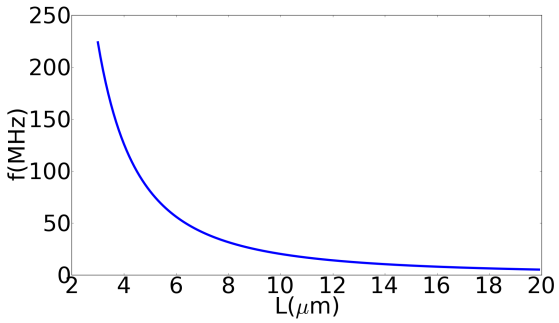

Figure 5.16: Fundamental resonance frequency of one of the slot beams as a function of length L with fixed boundary conditions.

5.2.3 Device layout

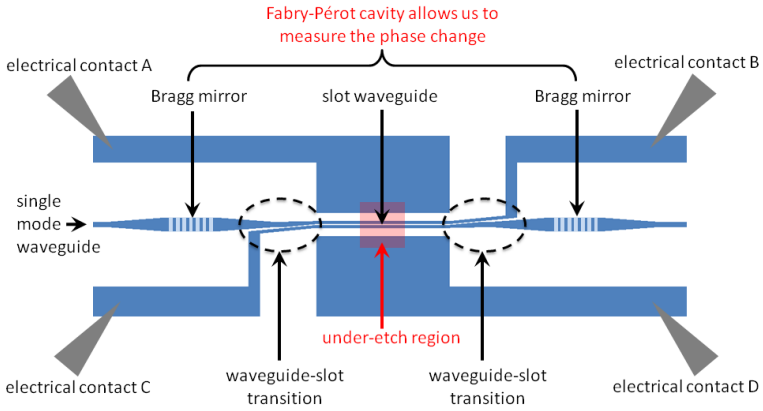

Figure 5.17: Schematic layout of the NEMS based phase modulator.

Figure 5.17 shows a schematic layout of the fabricated phase modulator. It was fabricated using the standard process flow described in Section 4.1. A cross section of the slot and all the designed dimensions is shown in Fig. 5.11. The slot width is 100 nm wide, while the beams are 230 nm wide.

Light enters through a single mode waveguide and is then guided to the slot waveguide through a specially designed transition [18]. The slot waveguide is under-etched so that part of the slot is free-standing. After passing through this under-etched slot, light is guided back to a single mode waveguide. The transitions are designed so that a voltage can be placed across the slot beams by using the electrical contacts B and C. Contacts A and D, together with B and C can be used to pull the slot open. The whole structure is placed between two shallow

etched Bragg reflectors that form the Fabry-Pérot cavity.

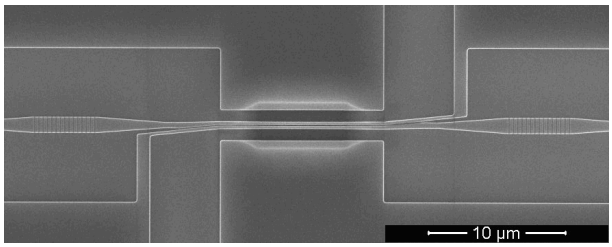

(a)

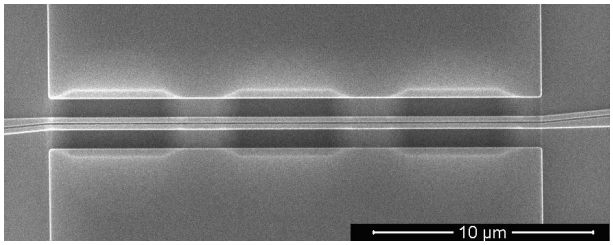

(b)

Figure 5.18: SEM pictures of the fabricated NEMS based phase modulator: (a) using a single under-etched region, (b) using a cascade of short under-etched regions.

The structure is under-etched by defining an etch region using contact-mask lithography and etching the buried oxide with buffered HF (hydrofluoric acid) for about 6 to 8 minutes. As the beams are relatively short, we were able to overcome the stiction problems that arise through capillary forces without the need of critical point drying. Figure 5.18 shows a SEM picture of two types of phase modulators: one with a single free-standing under-etched region of 9 μm and one with a cascade of three free-standing under-etched regions of 5.8 μm [19].

5.2.4 Measurements

Setup

Figure 5.19 shows a schematic of the measurement setup. The structure is excited through the broadband output light of an SLED (Superluminescent Light Emitting Diode). The light first goes through a polarization controller to rotate the light to the TE-like mode of the waveguide. The light is then coupled in an integrated waveguide using a standard grating coupler for near-vertical coupling (see Section 4.2.2) and passes through the Fabry-Pérot cavity in which the

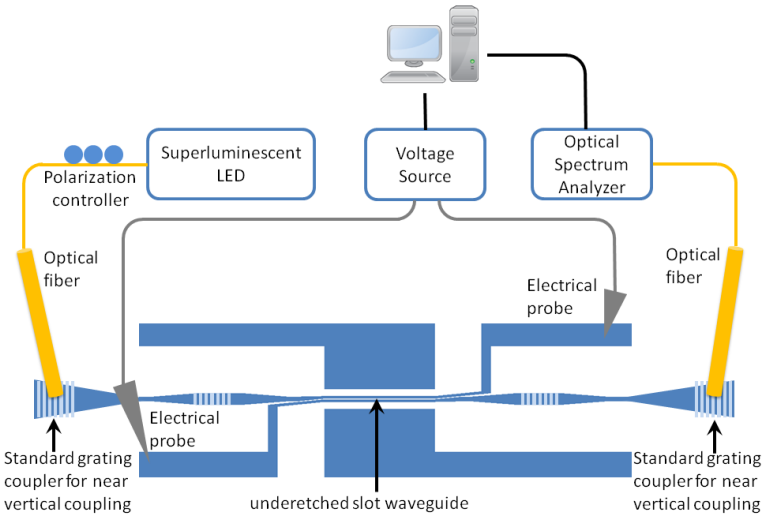

Figure 5.19: Measurement setup for the characterization of the NEMS based phase modulator: broadband light from an SLED goes through a polarization controller and is coupled into the photonic circuit using a grating coupler. The light at the output is sent to an OSA. A voltage source is connected to the Si-pads to apply a voltage over the slot.

slot waveguide is located. The output of the cavity is then sent to an Optical Spectrum Analyzer (OSA) to detect peak shifting as a result of the phase change in the cavity. A voltage source is connected to the silicon pads to contact the waveguides.

Results

The measured spectra for the modulator with one under-etched region of 9 μm are shown in Figure 5.20. The Bragg mirrors are relatively weak which results in broad resonances. The insertion loss at the Fabry-Pérot resonance near 1525 nm is about 5 dB. For longer wavelengths, the transmission decreases as the slot mode is reaching cut-off at the non under-etched region (there is no cut-off frequency when a slot is under-etched).

By measuring the peak shift for different voltages, the effective phase change inside the slot can be calculated. This is shown in Figure 5.21, where also the theoretical solution is shown. A good agreement can be seen. A phase change of 60° was observed for a voltage of 15 V. We note that the actual result is very dependent on the actual under-etch length (see Figure 5.15) and the initial slot width s_0. The discrepancy arising at larger voltages can be explained by the limitations of the simple model used where the residual axial stress, i.e., stress

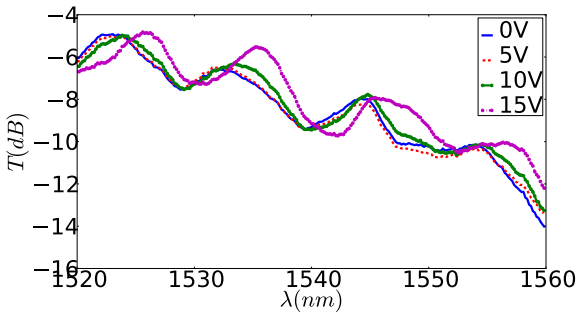

Figure 5.20: Measured Fabry-Pérot spectrum for different applied voltages for an under-etched region of 9 μm.

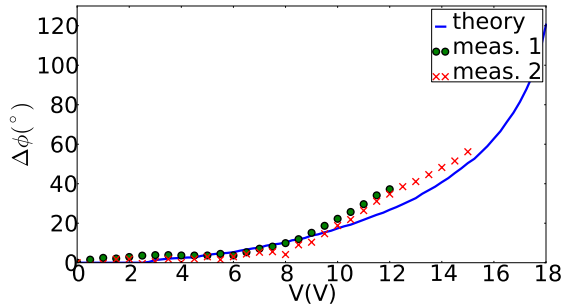

Figure 5.21: Theoretically predicted and measured phase change as a function of applied voltage across the 9 μm under-etched slot for two different measurements (meas. 1 and meas. 2).

arising from the movement of the beams, is neglected or by the used boundary conditions.

Figure 5.22 shows the result of a similar measurement for the cascaded structure of three under-etched regions. The phase change is higher than predicted by our model with fixed boundary conditions. A phase-change of about 40° was demonstrated for an applied voltage of 13 V. While small variations of the actual slot dimension can have a large influence as mentioned above, so do the boundary conditions used. For the cascaded structure, the fixed boundary conditions might not strictly apply, especially in the areas in between the under-etched regions. Figure 5.22 therefore also shows the simulation result when hinged boundary conditions are assumed. It can be seen that the measurement results lie in between these two extremes. Also note that the simulated pull-in voltage for hinged boundary conditions becomes much lower

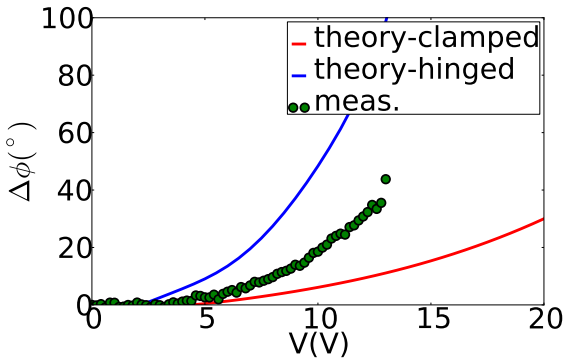

Figure 5.22: Theoretically predicted and measured phase change as a function of applied voltage across the cascade of 3 5.8 μm under-etched slots.

(15 V in this case) than in the case of fixed boundary conditions (30 V).

The speed of the cascade is predicted to be faster than of the longer single under-etched slot because of the higher fundamental mechanical resonance frequency given in Figure 5.16. The 9 μm slot has a theoretical fundamental frequency of around 25 MHz, while the for the 5.8 μm slots, this becomes 60 MHz when fixed boundary conditions are used.

To investigate the dynamic behavior, a square wave is applied across the cascade. We excite the modulator with a single wavelength and as the Fabry-Pérot resonance will shift (as seen in Figure 5.20), the measured optical power will vary. This signal is then amplified with and EDFA (Erbium Doped Fiber Amplifier), passes through a wavelength filter to filter out the broadband EDFA noise gain and is then measured with a high speed photodiode. Fifty spectra are then averaged to reduce the noise, as we are measuring small power variations.

Fig. 5.23 shows the measurement result. One of the beams is kept at ground while the other beam will have a square signal of 10 V and 100 μs period. The substrate is also grounded so that the beams are not only attracted to each other, but one beam is also attracted towards the substrate. This force is, however, an order of magnitude smaller as the distance to the substrate is 2 μm, compared to the 100 nm slot spacing. This asymmetric attraction can be overcome by using a bipolar source (one beam at +5 V and the other beam at -5 V) as both beams will then be attracted towards each other and also to the substrate.

The initial drop in power appears when the voltage is switched on at one beam from 0 to 10 V. The reaction of the beam can be described by a simple damped oscillator. The beam is excited with a step response when the square wave is applied and thus multiple mechanical resonance frequencies will be

excited. These will however be damped due to losses. There are three sources of losses that will damp the oscillations: intrinsic losses due to defects, clamping losses and gas damping. The gas damping will be the limiting loss factor which will limit the Q factor of the mechanical resonance and can be described by [20]:

$$Q_{gas} = \frac{m_{eff}\omega_0\sqrt{k_B T/m}}{pS}, \tag{5.13}$$

with m_{eff} the effective mass of the beam, ω_0 the angular frequency of oscillation, k_B Boltzmann's constant, T the temperature, m the individual molecule mass, p the gas pressure and S the surface area of the resonator. For air damping, this results in a Q_{gas} of only 7 for a 5.8 μm beam at atmospheric pressure for the fundamental resonance frequency using fixed boundary conditions. The damping time is then $2Q/\omega_0 = 37$ ns limiting the effect to a few tens of MHz.

The structure was, however, not optimized for high speed operation. There was no high-speed electrical pad layout, limiting the measurement speed to a few MHz. Furthermore, the complete structure (slot + silicon pad + access waveguides) also acts as a large distributed capacitance to the substrate and has a high distributed resistance. The complete resistance is of the order 20 MΩ while the complete capacitance is of the order 0.35 pF. The exact dynamic behavior is then difficult to predict. The RC constant is of the order 7 μs which explains the slow exponential effects visible in Figure 5.23. The initial response is however as fast as we were able to measure showing that the structure can operate in the MHz range.

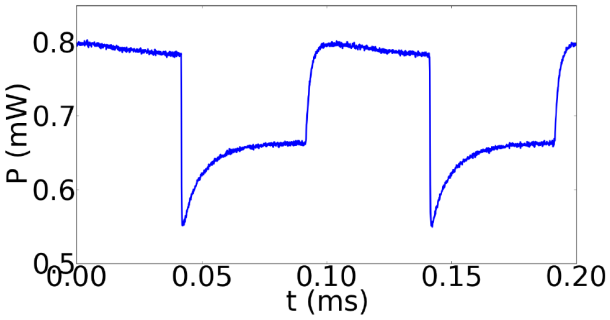

Figure 5.23: Measured dynamic behavior of the slot waveguide based phase modulator.

5.3 Other techniques

There exists a multitude of techniques for phase tuning and/or modulation apart from the ones described above, which are described briefly in this sec-

tion.

By doping the silicon, carrier-based modulators with speeds up to several ten of Gbps can be fabricated. These modulators have gained a lot of attention to address the interconnect problem, as they are one of the core components for an optical interconnect. Different types exist such as carrier accumulation, carrier injection and carrier depletion modulators. The latter is the weakest but fastest effect with experimental demonstrations up to 50 Gbps [21]. A more in-depth review about silicon modulators can be found in [22].

The electro-optic approach can deliver even faster data rates. Silicon has no second-order nonlinearity and thus hybrid materials need to be integrated on the silicon. While electro-optic (EO) modulators can work at speeds of more than 100 GHz, this has not yet been shown in a hybrid silicon approach. As the silicon of the slot in which the EO material is deposited, is used as electrode, care needs to be taken for impedance matching and velocity matching between both the electrical and optical mode. Simulations show that 20 GHz bandwidth is possible, limited by the RF attenuation of the silicon electrode [23]. In [24], a hybrid slot-based modulator was shown with a bandwidth of 3 GHz.

By introducing strain in silicon, the crystal symmetry is broken and a second-order nonlinearity arises. This has been proposed in [25] where a silicon nitride layer was deposited to induce strain in the silicon resulting in an induced nonlinear coefficient $\chi^{(2)} = 15$ pmV^{-1} and further optimized in [26] to $\chi^{(2)} = 122$ pmV^{-1} coming in reach of the efficiency of lithium-niobate based modulators ($\chi^{(2)} = 360$ pmV^{-1}).

A special type of an hybrid silicon EO modulator is a liquid crystal based modulator. By having a LC on top of an integrated waveguide and applying a voltage over the LC, the effective index of the mode changes with the orientation of the LC molecules. While it is a slow approach, limited by the molecular movement of the molecules, the tuning range can be very high [27].

5.4 Conclusions

In this chapter, two phase tuning techniques have been presented. The thermo-optic effect is a very simple approach which allows us to show the beam steering principle on SOI structures as will become clear in Chapter 6. As there is a continuous need for power dissipation, the effect is quite power-hungry. Optimized designs can bring the needed power down to the mW level or less.

A novel type of phase modulation was investigated using a NEMS-based approach. Applying a voltage over the two beams of an under-etched slot waveguide changes the beam position and thus its effective index. As this is a capacitive structure, power is only dissipated when switching. The speed is in the

MHz range, with several tens of MHz possible by using a cascade of short underetched slot waveguides.

Finally a short summary of some other phase tuning or modulation techniques were given.

References

[1] Jie Teng, Pieter Dumon, Wim Bogaerts, Hongbo Zhang, Xigao Jian, Xiuyou Han, Mingshan Zhao, Geert Morthier, and Roel Baets. *Athermal Silicon-on-insulator ring resonators by overlaying a polymer cladding on narrowed waveguides.* Optics Express, 17(17):14627–14633, 2009.

[2] Phoenix. *Solutions for Micro and Nano Technologies.* http://www.phoenixbv.com/, 2011.

[3] F. Gan, T. Barwicz, M. A. Popovic, M. S. Dahlem, C. W. Holzwarth, P. T. Rakich, H. I. Smith, E. P. Ippen, and F. X. Kartner. *Maximizing the Thermo-Optic Tuning Range of Silicon Photonic Structures.* pages 67–68, 2007.

[4] V. M. N. Passaro and F. Magno. *Investigation of thermo-optic effect and multireflector tunable filter/multiplexer in SOI waveguides.* Optics Express, 13(9):3429–3437, 2005.

[5] F. De Leonardis, A. V. Tsarev, and V. M. N. Passaro. *Optical properties of new wide heterogeneous waveguides with thermo optical shifters.* Optics Express, 16(26):21333–21338, 2008.

[6] Dai Daoxin, Yang Liu, and He Sailing. *Ultrasmall thermally tunable microring resonator with a submicrometer heater on Si nanowires.* Journal of Lightwave Technology, 26(6), 2008.

[7] Xuezhe Zheng, Ivan Shubin, Guoliang Li, Thierry Pinguet, Attila Mekis, Jin Yao, Hiren Thacker, Ying Luo, Joey Costa, Kannan Raj, John E. Cunningham, and Ashok V. Krishnamoorthy. *A tunable 1x4 silicon CMOS photonic wavelength multiplexer/demultiplexer for dense optical interconnects.* Optics Express, 18(5):5151–5160, 2010.

[8] D. N. Kwong, Zhang Yang, A. Hosseini, and R. T. Chen. *Integrated optical phased array based large angle beam steering system fabricated on silicon-on-insulator.* Proceedings of the SPIE - The International Society for Optical Engineering, 7943:79430Y–1 – 79430Y–6, 2011.

[9] J. Van Campenhout, W. M. J. Green, S. Assefa, and Y. A. Vlasov. *Integrated NiSi waveguide heaters for CMOS-compatible silicon thermo-optic devices.* Optics Letters, 35(7):1013–1015, 2010.

[10] Harjanne M., M. Kapulainen, T. Aalto, and P. Heimala. *Sub-mu s switching time in silicon-on-insulator Mach-Zehnder thermooptic switch.* IEEE Photonics Technology Letters, 16(9):2039–2041, 2004.

[11] I. De Vlaminck, J. Roels, D. Taillaert, D. Van Thourhout, R. Baets, L. Lagae, and G. Borghs. *Detection of nanomechanical motion by evanescent light wave coupling.* Applied Physics Letters, 90(23):3, 2007.

[12] J. Roels, I. De Vlaminck, L. Lagae, B. Maes, D. Van Thourhout, and R. Baets. *Tunable optical forces between nanophotonic waveguides.* Nature Nanotechnology, 4(8):510–513, 2009.

[13] D. Van Thourhout and J. Roels. *Optomechanical device actuation through the optical gradient force.* Nature Photonics, 4(4):211–217, 2010.

[14] Mo Li, W. H. P. Pernice, C. Xiong, T. Baehr-Jones, M. Hochberg, and H. X. Tang. *Harnessing optical forces in integrated photonic circuits.* Nature, 456:480–485, 2008.

[15] V. R. Almeida and R. R. Panepucci. *NOEMS devices based on Slot-Waveguides.* In 2007 Conference on Lasers & Electro-Optics/Quantum Electronics and Laser Science Conference, Baltimore, 2007.

[16] Photon Design. *Fimmwave.* http://www.photond.com/products/fimmwave.htm/, 2011.

[17] Joris Roels. *Actuation of Integrated Nanophotonic Devices through the Optical Gradient Force.* UGent, PhD Thesis, 2011.

[18] J Blasco and C. A. Barrios. *Compact slot-waveguide/channel-waveguide mode converter.* 2005 Conference on Lasers and Electro-Optics Europe, page 607, 2005.

[19] K. Van Acoleyen, J. Roels, T. Claes, D. Van Thourhout, and R. Baets. *NEMS-based optical phase modulator fabricated on Silicon-On-Insulator.* In 8th International Conference on Group IV Photonics (GFP 2011), pages 371–373 (FC6), Londen, UK, 2011.

[20] F. R. Blom, S. Bouwstra, M. Elwenspoek, and J. H. J. Fluitman. *Dependence of the quality factor of micromachined silicon beam resonators on pressure and geometry.* Journal of Vacuum Science and Technology B, 10(1):19–26, 1992.

[21] David J. Thomson, Frederic Y. Gardes, J.-M. Fedeli, Sanja Zlatanovic, Youfang Hu, Bill Ping Piu Kuo, Evgeny Myslivets, Nikola Alic, Stojan Radic, Goran Z. Mashanovich, and Graham T. Reed. *50-Gb/s Silicon Optical Modulator.* IEEE Photonics Technology Letters, 24(4):234–236, 2012.

[22] G. T. Reed, G. Mashanovich, F. J. Gardes, and D. J. Thomson. *Silicon optical modulators*. Nature Photonics, 4:518–526, 2010.

[23] Antao Chen, Haishan Sun, Attila Szep, Shouyuan Shi, Dennis Prather, Zhou Lin, Richard S. Kim, and Don Abeysinghe. *Achieving Higher Modulation Efficiency in Electrooptic Polymer Modulator With Slotted Silicon Waveguide*. Journal of Lightwave Technology, 29(21):3310–3318, 2011.

[24] R. Ding, T. Baehr-Jones, Y. Liu, R. Bojko, J. Witzens, S. Huang, J. Luo, S. Benight, P. Sullivan, J.-M. Fedeli, M. Fourier, L. Dalton, A Jen, and M. Hochberg. *Demonstration of a low Vpi x L modulator with GHz bandwidth based on electro-optic polymer-clad silicon slot waveguides*. Optics Express, 18(15):15618–15623, 2010.

[25] Rune S. Jacobsen, Karin N. Andersen, Peter I Borel, Jacob Fage-Pedersen, Lars H. Frandsen, Ole Hansen, Martin Kristensen, Andrei V. Lavrinenko, Gaid Moulin, Haiyan Ou, Christophe Peucheret, Zsigri Beata, and Anders Bjarklev. *Strained silicon as a new electro-optic material*. Nature, 441:199–202, 2006.

[26] Bartos Chmielak, Michael Waldow, Christopher Matheisen, Christian Ripperda, Jens Bolten, Thorsten Wahlbrink, Michael Nagel, Florian Merget, and Heinrich Kurz. *Pockels effect based fully integrated, strained silicon electro-optic modulator*. Optics Express, 19(18):17212–17219, 2011.

[27] W. De Cort. *Wavelength tunability of Silicon-On-Insulator Ring Resonators with a Cladding Layer of Liquid Crystals*. UGent, PhD Thesis, 2012.

6

Beam steering elements on SOI

In this chapter, the fabricated and measured beam steering elements are presented. Figure 1.2 in Section 1.1 shows a schematic view of the beam steering elements that will be presented here. All these basic elements have now been discussed in Chapter 4: guiding light, splitting light and coupling light off-chip and in Chapter 5: phase tuning.

In Section 6.1, the main elements of the measurement setup are discussed. Both Fourier imaging and motorized scanning were used to characterize the components, together with electrical probing to drive the different phase tuners. Next, the fabricated components are discussed. Section 6.2 discusses one-dimensional OPAs with active phase control, together with their applications such as one-dimensional steering, focusing and efficient light collection. Section 6.3 deals with two-dimensional OPAs on SOI. Main problems are the low fill-factor and high element spacing of these OPAs.

Next, we discuss two other types of components. While these structures still consist of arrays of radiating apertures and can thus still be considered as an OPA, there is no active phase control to steer the beam. Section 6.4 deals with a wavelength dispersive beam scanner, where a beam is scanned over a two-dimensional space by changing wavelength only. Section 6.5 presents a retroreflective integrated structure on SOI consisting of an array of apertures that will send an incident beam back to its direction of incidence. The main conclusions are finally summarized in Section 6.6.

6.1 Characterization setup

To investigate the far-field patterns of the fabricated components, a Fourier imaging setup is used which is discussed in Section 6.1.1. To test the components in a real space link, a motorized setup has been developed that allows to choose the direction of incidence by rotating and tilting the sample and which is discussed in Section 6.1.2. Section 6.1.3 deals with the electrical probing that is used for driving the integrated phase tuners. This is done using a National Instruments (NI) PXI (PCI EXtensions for Instrumentation) chassis with an analog output card and a probe card.

6.1.1 Fourier space imaging

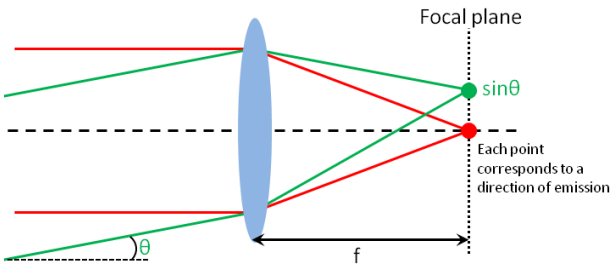

Figure 6.1: Fourier imaging basics.

To image the far-field, one can go and look in the far-field to do a step-by-step measurement and look at each direction of emission. Fourier space imaging provides a much more flexible and faster method for far-field imaging. It is a convenient, accurate, and fast approach that consists of imaging the far-field of a component directly on the backfocal plane of a high-NA (Numerical Aperture) microscope objective (MO). The NA of the lens determines the maximal angle of emission θ_{max} that is imaged by the lens:

$$\sin\theta_{max} = \text{NA}. \tag{6.1}$$

The basics of Fourier optics lies in the fact that a simple lens performs a Fourier transformation. Let us look at the case of a simple convex lens as shown in Figure 6.1. Each direction of emission corresponds to a different point in the focal plane, which is also referred to as the Fourier plane of the lens. A lens actually brings the far-field, which is at infinity, back to the focal plane of the lens. In this plane, one point corresponds to a unique direction of off-chip emission and can be parameterized by $\sin\theta$, with θ being the direction of emission [1, 2].

As a high NA is needed to image a large part of the far-field, either a very big, or very strong lens is needed. Usually one uses a high-NA MO. Problem then lies

in the fact that the focal distance is very small and thus we can not access the focal plane as it lies inside the MO. By using two extra lenses, this focal plane is imaged on a camera. By introducing an extra lens inside the setup, an extra Fourier transform is introduced resulting in real space imaging.

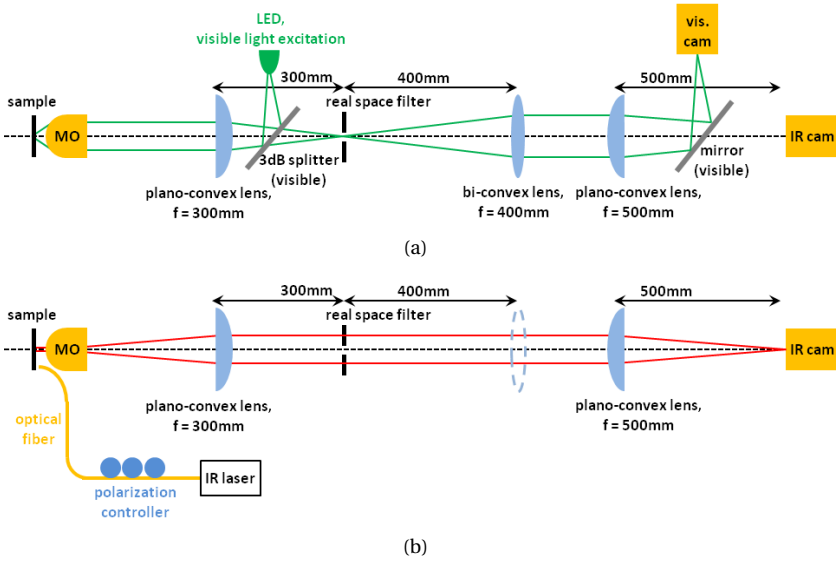

Figure 6.2: Fourier imaging setup. (a) Using an LED and a visible camera, the sample is aligned in the setup using real space imaging, in (b) the visible elements and the corresponding lens is removed for the IR Fourier imaging in which the sample is excited using an IR laser.

Figure 6.2 shows the measurement setup. The configuration of Figure 6.2(a) is used to align the sample. Real space imaging is done here for which visible light is introduced in the setup using a visible LED (Light Emitting Diode) and a 3 dB splitter. A real space filter is used to only select light that comes from the structure of interest. Other stray light and/or reflections will then not interfere with the far-field measurement. The (visible) light that is reflected from the sample is directed to a visible camera using a mirror.

The configuration of Figure 6.2(b) shows the IR (infrared) Fourier space imaging. An IR laser excites the structure. The 3 dB splitter, bi-convex lens and mirror are removed and the Fourier image is captured by the IR camera. The focal distances of the lenses were chosen such that the complete far-field of the MO (NA=0.5) was imaged on the camera. In Appendix A, the practical realization of this setup is discussed.

6.1.2 Motorized scanning

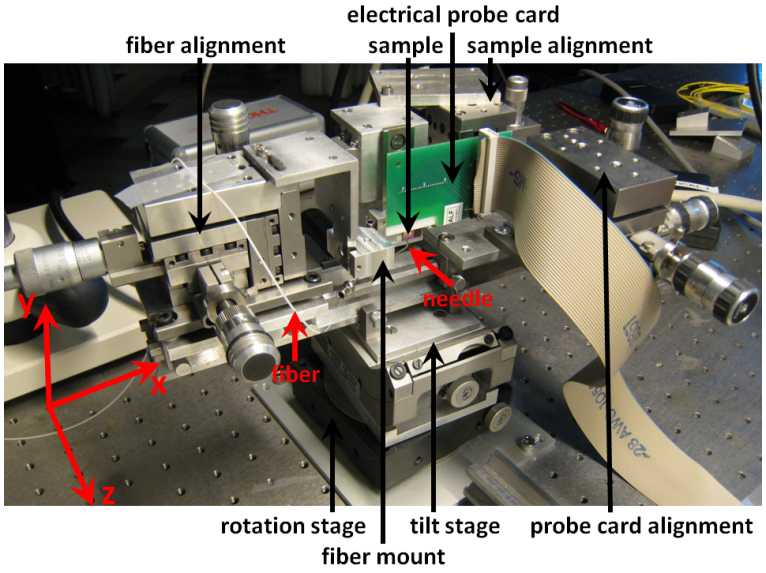

Figure 6.3: Motorized scanning setup: light travels along the z-direction while the sample can be rotated and tilted using motorized stages. An electrical probe card is also mounted for driving the phase modulators.

The Fourier imaging setup discussed in Section 6.1.1 is a very interesting tool to characterize the far-field pattern of the fabricated structures. However, for measuring retroreflective structures or using the structures in receiver mode, with real links being set up, we need to be able to choose the direction of incidence on the chip. An efficient way to do this in an experimental environment, is by rotating and tilting the sample while the direction of incidence of the IR light remains constant.

Figure 6.3 shows the sample mounted on a rotation and tilt stage. The sample mount is connected to a translation stage for alignment. Another translation stage holds the fiber which is used to excite the structure. This fiber is placed in a bent needle so that the fiber angle can be chosen to match the grating coupler angle. Light comes in or out of the structure along the z-direction.

When looking at the definition of angles discussed in Section 3.1.2, one might be tempted to say that $\theta_x = \theta_{rot}$ and $\theta_y = \theta_{tilt}$, with θ_{rot} and θ_{tilt} the angle of the rotation and tilt stage, respectively. This is, however, not exactly correct as the reference system of the sample moves when the stages move.

When doing the exact transformations, we get:

$$\sin\theta_x = \sin\theta_{rot}\cos\theta_{tilt} \quad (6.2)$$

$$\sin\theta_y = \sin\theta_{tilt}. \quad (6.3)$$

When the tilt angle is small, $\cos\theta_{tilt} \approx 1$ and the introduced error is small.

6.1.3 Electrical probing

To be able to drive the different phase modulators of the photonic circuit, while maintaining the motorized movement, a probe card was mounted on the motorized stages as shown in Figure 6.3. This probe card consists of an array of 20 probes, spaced 90 μm. The routing was kept fixed: two common grounds at either side while the 16 inner probes were signal probes. These signal probes were driven by a NI-PXI analog output card (NI-PXI 6704) which was fitted in a PXI chassis (NI-PXI 1033) as shown in Figure 6.4. The analog output card contains 16 voltages sources and 16 current sources which are able to give ±10V and up to 20mA current. Taking these boundary conditions into account, proper heaters for phase tuning can be designed as discussed in Chapter 5.

(a) (b)

Figure 6.4: PXI driver equipment: (a) PXI 6704 analog output card, (b) PXI 1033 low power chassis.

6.2 One-dimensional OPAs

One-dimensional OPAs have the advantage that high fill-factors can be reached since we do not need to worry much about routing issues. It is mainly the accessing of all the elements in a planar circuit that makes the fabrication of two-dimensional OPAs less trivial as discussed in Section 6.3. One-dimensional OPAs have the disadvantage of only allowing steering in 1D. Another external steering element would be needed for full 2D coverage. However, for scanning applications, one might be interested in a very fast 1D scanning, while scanning in the other dimension can be slower as a line-by-line scan is executed. One of the approaches discussed in Section 3.2 can then be used as a slower steering mechanism. Steering in the other — not phased array — dimension is still possible by wavelength tuning as the radiating aperture itself consists of a grating which is wavelength dependent.

In this section, two fabricated 1D OPAs with active phase control are discussed. The aperture width and spacing can be chosen freely between certain bounds to obtain the needed steering functionality. For 450 nm wide integrated waveguides on SOI operating at a wavelength of 1.55 μm, the minimal center-to-center spacing is about 1.3 μm to avoid optical coupling between the waveguides. These small waveguides have a very large FOV, which can be higher than 120°. Increasing the waveguide width will result in a narrower FOV (Equation (3.40)) while increasing the spacing results in a narrower beam (Equation (3.34)) and smaller higher order spacing (Equation (3.33)). As a rule of thumb, the number of addressable spots in the far-field is proportional to the number of elements N (see Equation (3.36)).

There is one main difference between the two OPAs presented here. The first OPA can only steer a beam to a limited extent as there is only one heater electrode available which can dissipate a limited amount of power. The second OPA has independent heaters for each radiating element allowing beam steering over the complete FOV. By having full control over all the phases, some extra applications come into play such as beam focusing, efficient light collection and direction-of-arrival (DOA) estimation.

First we will discuss the design, fabrication and measurements of an OPA with only one heater electrode. Afterward, we will go into the design with multiple electrodes. In Section 6.2.3, several applications of the OPA with full phase control are given.

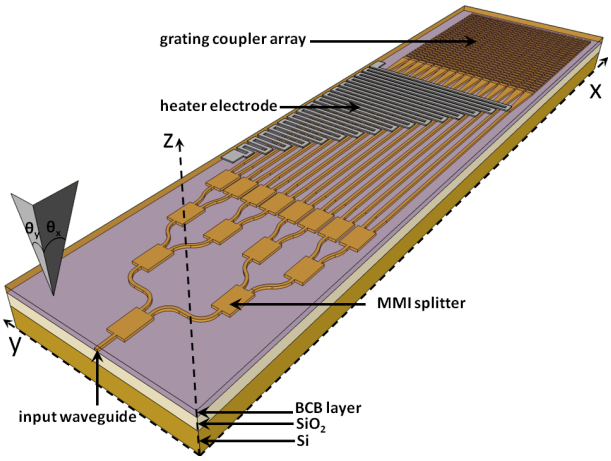

Figure 6.5: One-dimensional OPA with one addressing electrode: the heater layout imposes a linear phase ramp on the array of waveguides, resulting in beam steering.

6.2.1 One steering electrode

Design and Fabrication

Figure 6.5 shows a schematic of a one-dimensional OPA with one heater electrode and was fabricated using the standard process flow described in Section 4.1. Light entering through the input waveguide is split with an MMI-splitter tree into sixteen 450 nm-wide parallel waveguides, spaced 2 μm apart. These waveguides then taper to a 800 nm wide waveguide on which a grating is etched with a period of 630 nm and a fill factor of 0.5. A triangular shaped 100 nm thick Ti heater spiral is processed on top of the waveguide array with the process flow discussed in Section 5.1.1. When a current flows through the spiral, a triangular heating profile will result in a linear phase ramp over the waveguides [3].

Far-field measurements

Far-field measurements on this OPA have been done at EPFL (École Polytechnique Fédérale de Lausanne) using a similar Fourier imaging setup as discussed in Section 6.1.1 [1]. A high-NA MO was used with NA=0.9, resulting in far-field measurements up to angles of 64°, given by Equation (6.1). A typical measured far-field pattern can be found in Figure 6.6. Next, the different cuts along the θ_x- and θ_y-direction will be discussed.

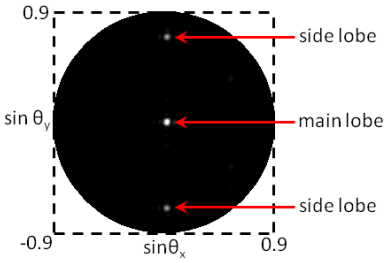

Figure 6.6: Far-field measurement of the radiated field at a wavelength of 1550 nm.

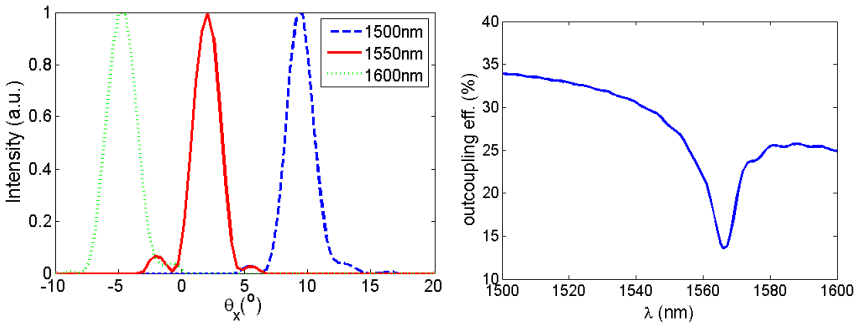

(a) (b)

Figure 6.7: (a) Normalized far-field pattern along the θ_x-angle for a wavelength of 1500 nm, 1550 nm and 1600 nm, (b) 3D-FDTD simulated out-coupling efficiency of a 800 nm wide grating coupler with a grating period of 630 nm as a function of wavelength.

I. Wavelength steering First steering along the θ_x-angle by wavelength tuning is examined. The out-coupling angle θ_x is governed by the grating equation (4.6):

$$\sin\theta_x = \frac{\Lambda_{gr} n_{eff,gr} - \lambda}{n_{bg}\Lambda_{gr}}, \tag{6.4}$$

with Λ_{gr} the period of the grating, λ the free-space wavelength, n_{eff} the effective index of the guided mode and n_{bg} the refractive index of the background. With n_{eff} being a function of temperature and the wavelength, there are two ways of steering the beam along the θ_x-angle: wavelength tuning or temperature tuning. The result of wavelength tuning can be seen in Figure 6.7(a). In this figure, normalized far-field patterns along the θ_x-angle are shown for three different wavelengths.

However, the out-coupling efficiency of the grating couplers changes with wavelength, making large angle steering in this way not very attractive. The

out-coupling efficiency of these gratings were simulated using 3D-FDTD simulations [4] shown in Figure 6.7(b), where the out-coupling efficiency versus wavelength of one grating coupler is plotted. The efficiency drops from 34% at 1500 nm to 25% at 1600 nm with a dip of 14% near $\lambda = 1565$ nm which corresponds to the vertical out-coupling angle $\theta_x = 0°$. Strictly vertical out-coupling is thus not desired since in that case the second-order reflection back into the waveguide reduces the out-coupling efficiency. By changing the grating coupler period, this dip can be shifted out of the region of interest. For a wavelength of 1500 nm, 1550 nm and 1600 nm a steering angle of 9.4°, 2.0° and −4.7° with a FWHM beam width of 2.4°, 2.5° and 2.8°, respectively, were observed. This beam width is determined by the out-coupling strength of the grating. The wavelength dependent steering can simply be removed by cleaving the chip and using the end facet of the waveguides as radiating elements which is the approach taken in [5].

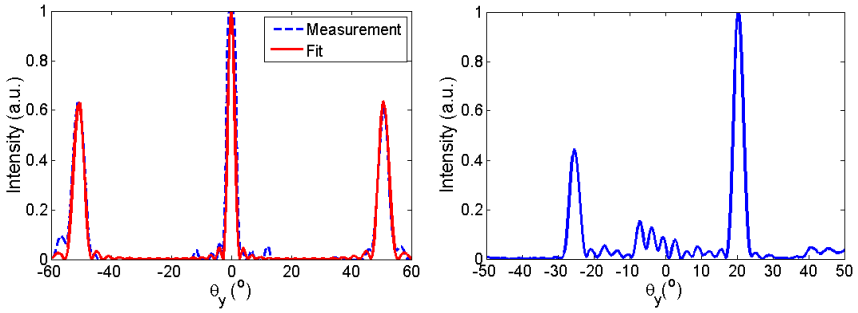

Figure 6.8: Normalized far-field pattern along the θ_y-angle of an array of 16 grating couplers at 1550 nm: (a) without the heater electrode region, (b) with a fixed effective index difference between the waveguides and the heater electrode.

II. Phased array steering Figure 6.8(a) shows the far-field in the θ_y-direction of a reference structure without heater region. The measurement result is fit to a simulation of an array of Gaussian beams in 1D. When the individual Gaussians are modeled with a 1/e mode width of 680 nm, we can see a good agreement with the measurement. The measured FWHM beam width (Equation (3.34)) of the main lobe is 2.7° compared to a simulated FWHM of 2.4°. The second-order peaks of the grating can be found at an angle of $\theta_y = \arcsin(\lambda/\Lambda_y) = 50.8°$. This angle can be increased by reducing the separation between the individual grating couplers. The FOV is 120°, which compares well to the Gaussian aperture

array example given in Section 3.1.6.

In a next stage, long waveguide regions were introduced between which a uniform effective index difference was introduced by changing the waveguide width. Such a fixed effective index difference results in a fixed phase difference and thus fixed beam steering. The far-field measurement of one of these structures is shown in Figure 6.8(b). The far-field is, however, degraded due to the phase errors introduced by the long 450 nm waveguide lines which was solved in the OPAs discussed in Section 6.2.2. On top of these long waveguide regions the heater electrode was processed.

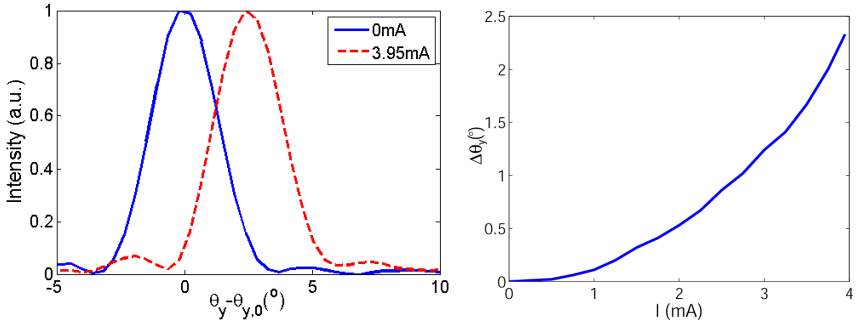

(a) (b)

Figure 6.9: (a) Detail of the peak of Figure 6.8(b) at $\theta_y = 20°$ for two different currents in the heater. (b) Steering $\Delta\theta_y$ of the peak in (a) as a function of the injected current.

When a current is flowing through the heater electrode, a linear phase ramp is imposed on the array of waveguides due to the Joule heating and the specific shape of the electrode. Figure 6.9(a) shows a detail of a main peak (at position $\theta_{y,0} = 20°$) of Figure 6.8(b). The beam shifts with a linear dependence on the power and thus in a simple model with a quadratic dependence on the current as shown in Figure 6.9(b). For a current of 3.95 mA, a shift of 2.3° was observed. Following Equation (3.31), this implies a phase difference of $\Delta\varphi_y = 0.105\pi$ between the grating couplers. The electrode thus imposes this phase shift at the first waveguide, twice this phase shift at the second waveguide, etc. The total phase shift induced by the electrode is $\Phi_{tot} = (1+2+\ldots+16)\times 0.105\pi = 14.28\pi$. The measured resistance of the electrode was approximately 15 kΩ. Approximately half of this resistor was used for the phase shift such that the power needed for a π phase shift is given by $P_\pi = 8.2$ mW. Using this approach, 2π resets can be avoided at the cost of large power consumption. As there is only one single electrode only a limited amount of power can be dissipated without burning the electrode which limits the steering range. By placing a mirrored elec-

trode, steering could be achieved in both directions with only two electrodes.

6.2.2 Multiple steering electrodes

Design and Fabrication

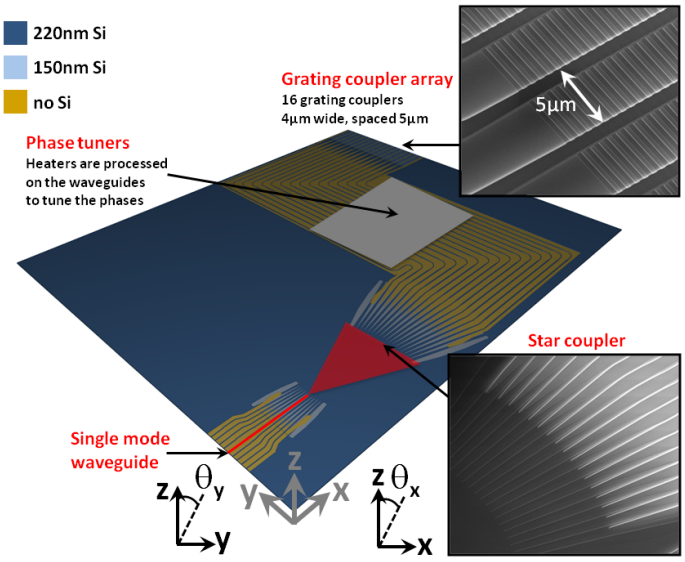

Figure 6.10: One-dimensional OPA with 16 addressing electrodes: the heaters can be tuned to impose a random phase front.

Figure 6.10 shows the schematic of a one-dimensional OPA with multiple heater electrodes. The component was fabricated using the standard process flow described in Section 4.1. Light entering through the input waveguide is not split with an MMI-splitter tree, but with a star coupler into sixteen waveguides. The waveguides then take an S-turn to be able to convert the circular phase profile of the star coupler into a linear phase profile at the grating coupler array. All the elements are then in phase when the heaters are not driven. At the grating coupler array, the waveguides taper to a 4 μm wide waveguide, spaced 5 μm, on which a grating is etched with a 630 nm period and fill factor of 0.5. To reduce the phase errors introduced by the long delay lines on which the heaters are processed, the waveguide width tapers from 450 nm to 800 nm as wider waveguides are more tolerant to fabrication deviations and surface roughness.

By making use of a star coupler to split the light, a natural apodization of the field over the OPA is obtained through the free propagation region of the star coupler. This reduces the sidelobe level of the far-field. The simulation shows a sidelobe level decrease of 13 dB as can be seen in Figure 6.11. In this figure

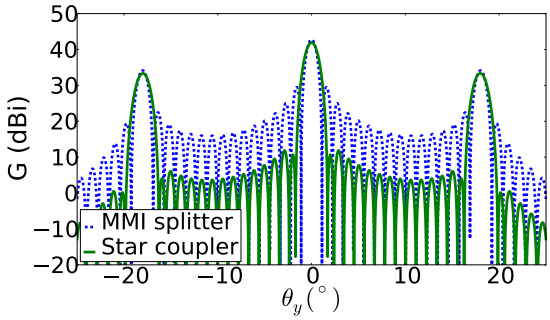

Figure 6.11: Simulated far-field of a 16 element 1D OPA with equal amount of power in each element (MMI splitter tree) or with apodization (star coupler). A sidelobe reduction of 13 dB can be seen.

the simulated far-field of the beam steering component in the θ_y-direction is shown for the two different cases at a wavelength of 1550 nm. The FWHM beam width becomes a bit larger and increases from 0.98° to 1.26°, as the total effective radiating aperture becomes smaller due to the apodization.

Instead of one heater electrode, 16 different addressable electrodes were processed using the process flow described in Section 5.1.1. The heaters are 2.5 μm wide, 450 μm long and consist of a 100 nm Ti and 20 nm Au stack, sufficient to ensure a 2π phase shift [6].

Far-field measurements

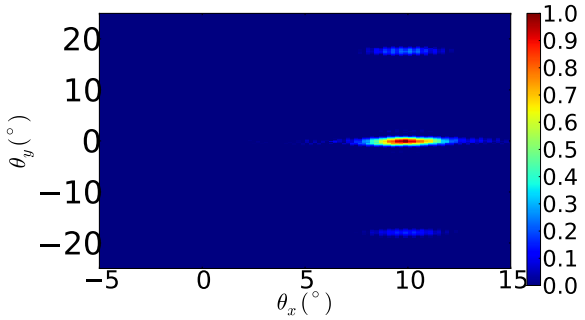

Figure 6.12: Far-field measurement of the radiated field at a wavelength of 1550 nm.

Far-field characterization of the OPA was performed with the Fourier imaging setup discussed in Section 6.1.1. A MO with NA=0.5 was used so that the

maximum angle of emission that is measured equals 30°. Figure 6.12 shows the far-field. A broad beam in the θ_x-direction can be seen, which is determined by the out-coupling grating and centered around $\theta_x = 10°$ being the out-coupling angle of the grating given by the grating equation (4.6). In the θ_y-direction, a typical OPA far-field pattern can be seen. The beam is narrow and the different output orders are visible with a spacing of 18°. Next, the different cuts will be discussed.

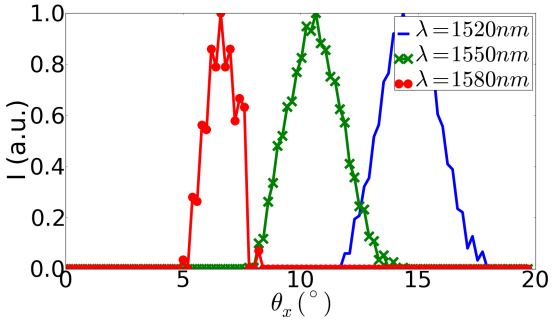

Figure 6.13: Normalized far-field pattern along the θ_x-angle for a wavelength of 1520 nm, 1550 nm and 1580 nm.

I. Wavelength steering Wavelength steering shows a similar behavior as the wavelength steering discussed above in Section 6.2.1. The FWHM beam width is measured to be 3.0°, 2.8° and 1.6° for a wavelength of 1520 nm, 1550 nm and 1580 nm, respectively and the beam is steered over a 8.0° range for a 60 nm wavelength shift. Note that vertical coupling was avoided here as compared to the OPA described above by shifting this dip out of the measurement range. The simulated out-coupling in the measurement range does not vary much and is around 38%.

The smaller beam width for increasing wavelength can be explained due to the fact that the grating couples the light out less efficiently, so that the exponential tail becomes larger and the far-field beam width will decrease.

II. Phased array steering Two types of phased array steering were observed. By using a different input waveguide of the star coupler as shown in Figure 6.10, fixed steering of the beam in the θ_y-direction is observed. The free spectral range of the far-field in the θ_y-direction is equal to $\arcsin(\lambda/\Lambda_y)$ with λ the wavelength and Λ_y the spacing of the grating couplers (Λ_y=5 μm). At λ = 1.55 μm, this corresponds to 18°. We have chosen 9 access waveguides and each waveguide was designed to result in a shift of 2° so that the complete FOV

is covered. A cross-sectional view of the far-field in the θ_y-direction for different access waveguides is shown in Figure 6.14. In this figure, only the far-fields for 5 input waveguides are plotted in order not to overload the figure. The envelope of the far-field pattern is shown as well and has a FWHM of 23° which is determined by the width of the grating couplers. The beam width is 1.27° which compares well to the simulated value of 1.26°. The different output orders at a spacing of 18° are visible as well.

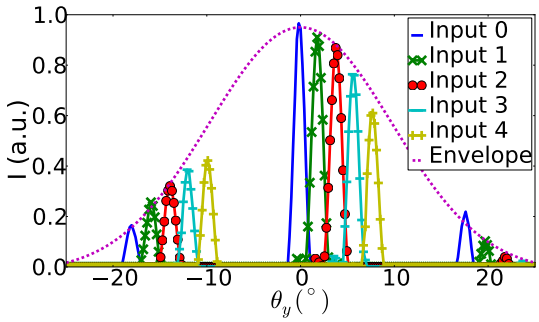

Figure 6.14: Measured far-field in the θ_y-direction for different input waveguides (Figure 6.10) at 1550 nm. The dashed line shows the envelope of the far-field pattern.

By using the thermo-optic phase tuners, we can now steer the beam over the complete FOV in the θ_y-direction. As the phase change φ_y is directly proportional to the dissipated power in the heater, and the latter is proportional to the applied voltage V squared, we use the simple model:

$$\varphi_y = \beta V^2, \tag{6.5}$$

where β is a fixed parameter. Using this simple model, the 2π phase resets can be taken into account. To steer the beam at an angle θ_y, the phase difference $\Delta\varphi_y$ between each waveguide is equal to (Equation (3.31)):

$$\Delta\varphi_y = \frac{2\pi\Lambda_y}{\lambda}\sin\theta_y. \tag{6.6}$$

In Figure 6.15, a cross-sectional view of the far-field in the θ_y-direction is shown when the beam is steered at different angles. When steering at an θ_y-angle of 18°, the far-field coincides with the original far-field at 0° which proves the validity of our simple model.

We have designed a similar OPA using carrier depletion modulators. The phase tuning effect of these modulators is small but fast. In the S-shape, instead of 16 heaters, we introduced 16 carrier depletion modulators with a length of

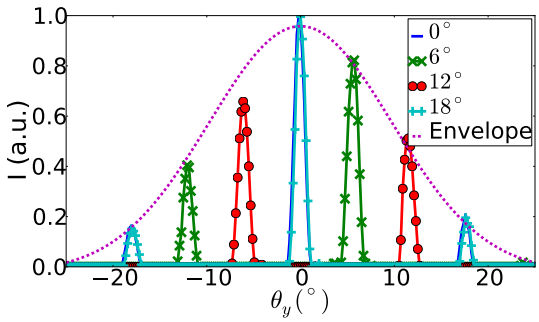

Figure 6.15: Measured far-field in the θ_y-direction using thermo-optic steering at 1550 nm. The beam is steered to the angles 0°, 6°, 12° and 18°. The dashed line shows the envelope of the far-field pattern.

2.5 mm. Apart from the phase change, the carriers will also induce an amplitude modulation of a few dB. These components are currently under fabrication but were not ready in time to be measured in the scope of this work.

6.2.3 Applications

Next, some applications and measurement results are given of the OPA discussed above in Section 6.2.2. Beam focusing will be discussed first, which has applications in sensing. Afterward efficient light collection of scattered light and DOA measurements are discussed.

Beam focusing

As an OPA is actually a one-dimensional programmable lens, light can be focused above chip in one dimension. This becomes increasingly interesting when one wants to use a photonic integrated circuit (PIC) for sensing applications, such as in on-chip laser Doppler velocimetry [7] or Optical Coherence Tomography (OCT) [8]. Light is for example focused on the skin and reflected back in the PIC for further processing. The beam can then be shaped to optimize the link losses. Such beam focusing on an integrated platform has been studied in [9], where an AWG is used to focus the light onto a biological medium and measure the scattered light. The approach here with active phase control allows for a dynamic focus of the light as well as a movable focus spot.

The focusing capabilities of the component are studied with the setup shown in Figure 6.16. The structure is excited using a tunable laser and a polarization controller. At a certain distance f, a single mode optical fiber is placed to capture the light radiated from the structure. The component is positioned

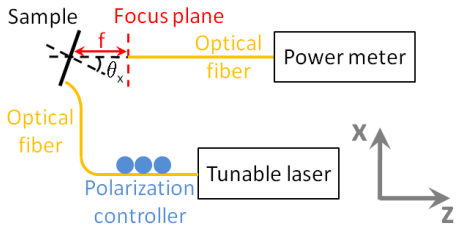

Figure 6.16: Using a fiber at a distance f of the sample, the focusing capability of the structure is investigated.

at a certain angle θ_x which is the out-coupling angle of the grating. The light is then focused in the yz-plane on the tip of the fiber in one-dimension and the received power is measured.

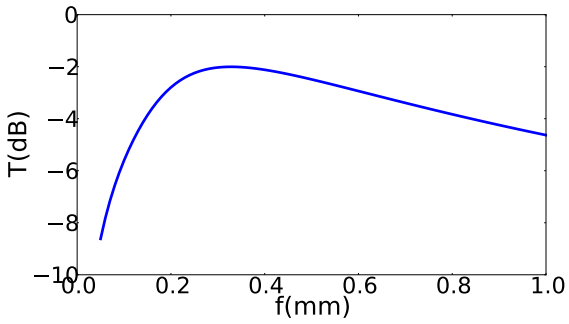

Figure 6.17: One-dimensional simulated coupling efficiency of the 16 element OPA to an optical fiber as a function of distance between the OPA and the fiber at a wavelength of 1550 nm. For each point, the phases are set to focus the light onto the fiber.

By programming the phase tuners to act as a spherical lens, light is focused above the chip in one-dimension. Figure 6.17 shows the simulated coupling efficiency from the OPA to the fiber as a function of distance f between the chip and the fiber (Figure 6.16). For very small f, the NA of the fiber is too small to capture this light and a low efficiency is seen. At a distance of 0.33 mm, an optimum is found, when the NA of the component matches the one of the optical fiber. Note that this loss of 2 dB is only the loss in one dimension and is due to the fill-factor of the OPA.

In Figure 6.18 the measured power into the fiber is given for the case when the light is focused onto the fiber and when no focusing is used at a wavelength of 1550 nm. The power shown is relative to the power received when the fiber is exactly on top of the structure (f = 0 mm) and no focusing is used. At first in-

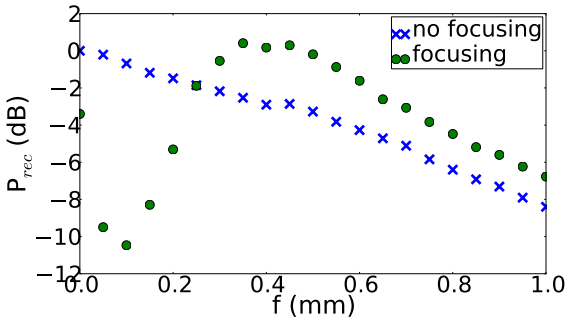

Figure 6.18: Measured relative received power into an optical fiber at a distance f of the 16 element OPA at a wavelength of 1550 nm. For each point, the phases are set to focus the light onto the fiber. The power is relative to the power received at $f = 0$ mm when no focusing is used.

stance, a simple model is used to focus the light, as explained above. Afterward a rough optimization run did not show any significant improvement. There is an optimum focus point at $f = 0.4$ mm, which shows the focusing capabilities of the 1D OPA. An increase of 3 dB in received power is observed. By using an apodized grating, light can also be focused in the other dimension at a fixed point.

Efficient light collection

When one wants to couple through free-space into an integrated circuit, one needs to efficiently guide light into a photonic waveguide. By using an OPA with individually addressable phase tuners, the phases can be set to efficiently combine all the contributions into a single mode waveguide, even when the phase front is distorted. This allows to efficiently collect light from scattering media [10] which is especially useful in biological applications and Raman spectroscopy [11]. Also propagation through the atmosphere imposes phase errors which can be countered by a coherent beam combining approach [12].

The OPA is now used as a receiver. Light falls onto the 16 waveguides and when all the phases are set right, they will be combined efficiently into a single mode waveguide. As scattered light has a random phase distribution, the problem now consists of optimizing 16 random phases. Using a gradient based algorithm, this can happen in about 100 iterations as shown in Figure 6.19. In an experimental environment, such an algorithm is not very robust against measurement fluctuations that are present due to small vibrations. Therefore we chose to use a robust annealing algorithm available in Python SciPy pack-

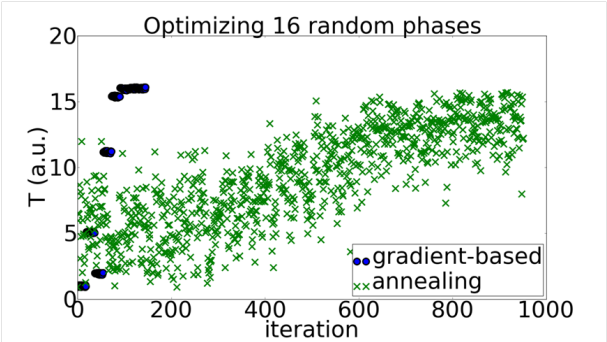

Figure 6.19: Simulated optimization of 16 random phases using a gradient based and annealing algorithm.

age [13]. The number of iterations needed now increases with a factor 10, shown in Figure 6.19.

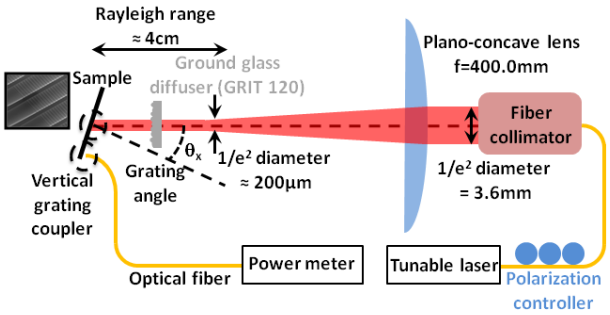

Figure 6.20: Experimental setup for efficient light collection of scattered light.

Figure 6.20 shows a schematic of the measurement setup used to capture scattered light. Infrared light from a tunable laser goes through a polarization controller and is focused with a plano-convex lens just above the sample, so no direct light hits the structure. A diffuser is then placed in the Rayleigh range of the focused light which will scatter the light. This scattered light falls on the structure and is, after passing through the structure, coupled in an optical fiber which is connected to an optical power meter. The heaters are electrically probed using a probe card to individually address the heaters.

Figure 6.21 shows a typical optimization run. As the scattering is wavelength dependent, we have performed this optimization for different wavelengths as shown in Figure 6.22. For the 16 element structure, a general increase of more than 10 dB can be seen. The speed of the heaters was measured to be 20 kHz so

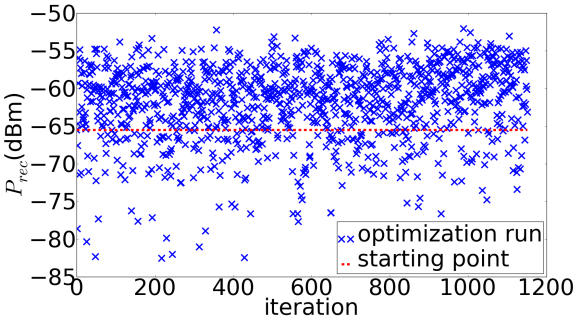

Figure 6.21: Optimization of the random phases at λ = 1550 nm. The red dashed line shows the starting point.

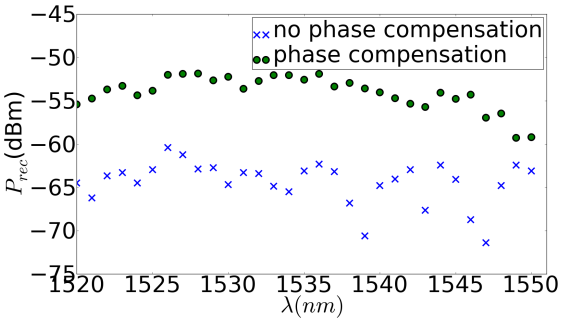

Figure 6.22: Optimization of the random phases for different wavelengths. A general increase of 10 dB can be seen.

that 1000 iterations can happen in 50 ms. We believe that this can be increased by an order of magnitude by developing dedicated optimization algorithms and optimizing the heater speed.

The process of phase recombination becomes clear when looking at the example of a $N \times 1$ combiner. On average, each arm holds a power of P/N. When there is a random phase of each element, there is a $1/N$ loss factor, so the total average loss is $N \times 1/N \times P/N = P/N$. Note that this is an average loss. If for example the phases are set to destructively interfere, there will be almost no power combined (explaining the dips in Figure 6.22). However, by efficient phase recombination, all the power in the arms can be added coherently and the $1/N$ loss factor disappears. The improvement is thus a factor N or, for a 16 element array, 12 dB. For the 16 element structure, a general increase of more than 10 dB was measured, while also the large dips have disappeared due to the efficient phase recombination. This compares well to the theoretical expected value.

DOA estimation

Using a simple sweeping algorithm a Direction-Of-Arrival (DOA) measurement can be done. This can find applications in wireless link setup schemes and wavefront sensing.

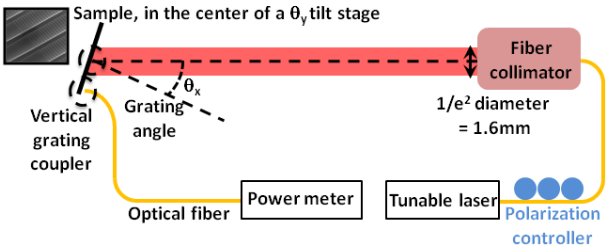

Figure 6.23: Experimental setup for DOA estimation.

Figure 6.23 shows the measurement setup used for DOA estimation. The sample is mounted in the center of a motorized tilt stage so that the θ_y-angle of incidence can be tuned (see Section 6.1.2). Light thus falls onto the structure from a certain θ_y-angle and by imposing a linear phase sweep over the waveguides, the DOA can be estimated. When there is a uniform phase difference $\Delta\varphi_y$ between each element, the structure will efficiently couple light in from an angle θ_y (Equation (3.31)):

$$\sin\theta_y = \frac{\lambda}{2\pi\Lambda_y}\Delta\varphi_y, \tag{6.7}$$

with Λ_y the spacing of the elements. Due to the spacing, there will be ambiguity because of the higher orders of the array. Only within the free spectral range ($\Delta\theta_{FSR} \approx \arcsin\lambda/\Lambda_y$) of the array, the direction can be determined without ambiguity, which is 18° for the structure with 5 μm spacing. This can easily be increased by decreasing the spacing. While this increases the range over which the beam direction can unambiguously be determined, the collection and resolution will decrease as the number of resolvable directions scales with the number of elements N(=16). A trade-off thus needs to be made between complexity, efficiency and performance of the system. When the light now hits the structure, the phases over the heaters are swept to determine the direction of arrival.

Figure 6.24 shows the sweeping result for an angle of incidence of $\theta_y = 5°$. There is a clear peak visible at this angle, but also at the $\theta_y = -13°$ angle due to the FSR of the array. The width of the peak is determined by the spatial distribution of the incoming field and the number of light capturing elements. As this number is limited to 16 the peak is quite wide with a FWHM of 1.24°.

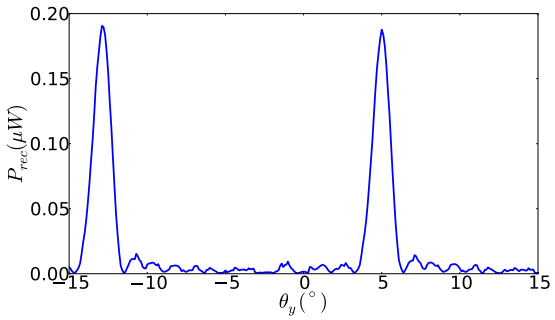

Figure 6.24: DOA measurement when light impinges at a 5° angle.

Optical links

To determine the possibilities to use these OPAs in an optical link, one can use the formalism described in Section 3.1.3. The main parameter that is needed is the OPA directivity. The directivity of the OPAs can be calculated using Equation (3.14):

$$D(\theta_x,\theta_y) = 4\pi \frac{I(\theta_x,\theta_y)}{P_{rad}}, \tag{6.8}$$

with P_{rad} the total power radiated by the OPA. For the OPA discussed in Section 6.2.1, the theoretical directivity is 32.8 dBi compared to a measured directivity of 32.7 dBi. For the OPA in Section 6.2.2, the radiating aperture is larger due to the wider grating couplers, but the FOV is limited. Simulated directivity was 41.2 dBi while the measured directivity was 42.4 dBi.

Knowing these directivities, some basic link budgets can be calculated using the formalism of Section 3.1.3. Let us take for example a directivity of 42 dBi and we try to establish a reciprocal link. The path loss (PL) at 1 m is equal to -138.2 dB. The efficiency of our antennas is given by the grating coupler efficiency and can be higher than $\eta = -1.6$ dB using a silicon overlay. To avoid the fact that polarization mismatch kills the signal completely, two OPAs with orthogonal orientation on-chip can be used or we can change to polarization at the transmitter side to a circular polarization using a bulk polarization plate. We thus assume a polarization mismatch loss of $Q_{rt} = 3.0$ dB. The transmit power is assumed to be 10.0 dBm. A typical link budget is then given in Table 6.1.

The received power is quite low allowing only a few 10 Mbps links. To reach a 10 Gbps link, the received power should typically be in the range of -25 dBm [14], meaning the link would have to operate at the cm-distance range.

	value	unit
P_t	10.0	dBm
η_t	-1.6	dB
D_t	42.0	dBi
PL@1m	-138.2	dB
Q_{rt}	-3.0	dB
η_r	-1.6	dB
D_r	42.0	dBi
P_r	-50.4	dBm

Table 6.1: A typical link budget calculation.

6.3 Two-dimensional OPAs

Two-dimensional OPAs in the planar silicon photonics technology are much more challenging to fabricate. Due to the necessary routing, the element spacing is large and the fill factor is low. When choosing a large element spacing, multiple higher-order grating lobes in the far-field will be present. There is still a redistribution of the complete radiation pattern of one element into several more directive lobes. This can find applications in multipath optical links [15], being an intermediate between directive and diffuse links, discussed in Section 2.2. In the design presented below, beam steering is possible by integrating heaters as discussed earlier. Due to a fixed delay present between different elements, steering is also possible using wavelength steering.

Next, the design and fabrication of the two-dimensional OPA is discussed. Section 6.3.2 deals with the far-field characterization, wavelength steering capability and directivity of the fabricated OPA.

6.3.1 Design and Fabrication

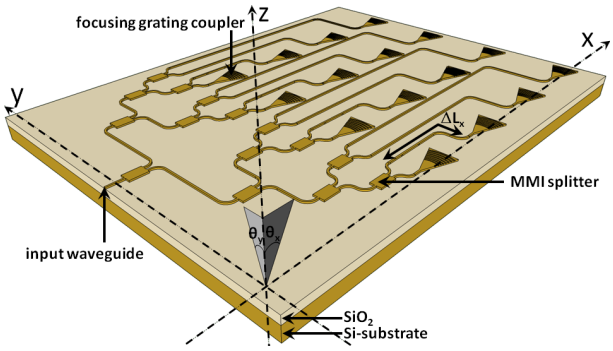

Figure 6.25: Schematic view of a two-dimensional OPA on SOI. Light is split through an MMI splitter tree and radiated off-chip using a focusing grating coupler.

Figure 6.25 shows a schematic view of the fabricated two-dimensional OPA fabricated using the process flow described in Section 4.1. The input waveguide is split by a MMI tree into $N_x \times N_y$ output waveguides, being 4 for a 2 by 2 array and 16 for a 4 by 4 array. The radiating elements consist of a focusing grating coupler that couples light out in a near vertical direction [16]. The period of the focusing grating coupler was 625 nm. First the radiation pattern of one of these focusing grating couplers is examined as this determines the FOV of the component. Next, the phased array measurements are presented. The radiation pat-

terns were measured using the Fourier imaging setup described in Section 6.1.1 with an MO with NA of 0.5 [17].

6.3.2 Measurements

Far-field patterns

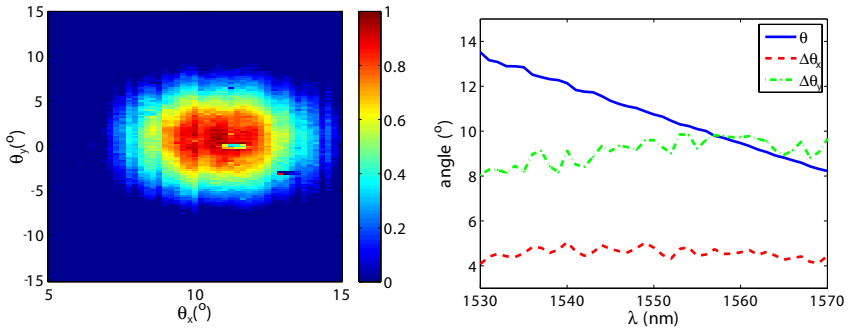

Figure 6.26: (a) Far-field pattern of the focusing grating coupler at a wavelength of 1550 nm. The FWHM width in the θ_x-direction is 4.8° and in the θ_y-direction is 9.6°. (b) Out-coupling angle θ_x (blue), FWHM $\Delta\theta_x$ (red) and FWHM $\Delta\theta_y$ (green) of the focusing grating coupler as a function of wavelength.

Figure 6.26(a) shows the measured far-field of the focusing grating coupler. The far-field will shift in the θ_x-direction due to the grating equation (4.6). The shift in θ_x-direction as well as the change in beam width can be found in Figure 6.26(b). While the beam shifts in the negative θ_x-direction for increasing wavelength, the beam width does not vary much.

Figure 6.27 shows the measured far-field pattern of a 2×2 OPA together with the theoretical far-field. Figure 6.28 shows a cross-section of the far-field along the θ_x-direction for a 2×2 and 4×4 OPA. A good agreement can be seen. The parameters of these OPAs are found in Table 6.2.

Wavelength steering capability

As can be seen in Figure 6.25, there is a fixed delay length difference ΔL_x between the elements in the x-direction, this results in a phase difference of:

$$\Delta\varphi_x = n_{eff}\frac{2\pi}{\lambda}\Delta L_x \tag{6.9}$$

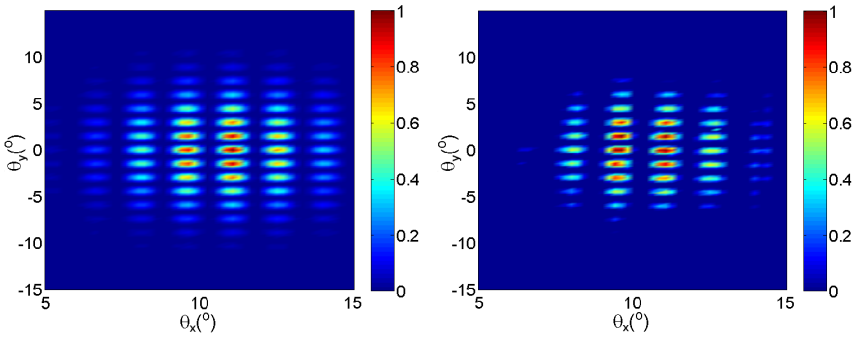

Figure 6.27: Theoretical (a) and measured (b) far-field pattern of a 2 × 2 OPA at a wavelength of 1550 nm, the parameters are found in Table 6.2.

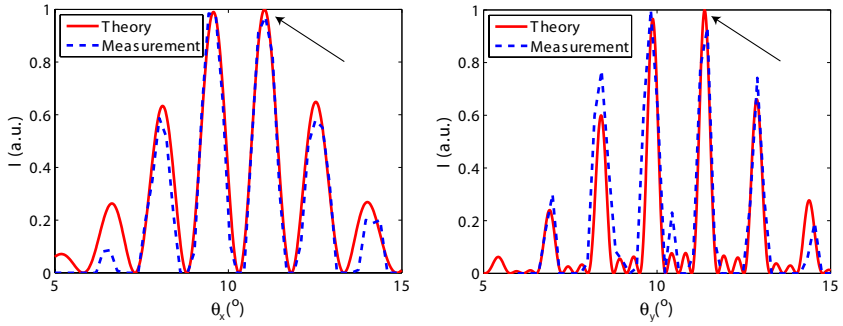

Figure 6.28: Cross-section at $\theta_y = 0°$ of the far-field pattern of a (a) 2 × 2 and (b) 4 × 4 OPA at a wavelength of 1550 nm, the parameters of the OPA are found in Table 6.2. The indicated peak has a width of (a) 0.66° and (b) 0.36°.

Using Equation (3.31), we know that the array peaks are found at:

$$\sin\theta_x = q\frac{\lambda}{\Lambda_x} + \frac{n_{eff}\Delta L_x}{\Lambda_x}, \tag{6.10}$$

for integer q, with n_{eff} the effective index of the delay line. Due to the delay lines, the absolute value of q will be large. The beams will shift at a rate of

$$\frac{d\theta_x}{d\lambda} \approx \frac{d\sin\theta_x}{d\lambda} = \frac{q}{\Lambda_x} + \frac{dn_{eff}}{d\lambda}\frac{\Delta L_x}{\Lambda_x}, \tag{6.11}$$

where the angle θ_x is assumed to be relatively small. Note that q is negative so that the beam will shift in the negative θ_x-direction for increasing wavelength. The effect of dispersion cannot be neglected in this high index contrast platform. There are two main contributions to dispersion: material dispersion and waveguide dispersion. Whereas the former is relatively weak for the small wavelength range considered here, the latter has a significant influence due to the extremely high confinement in the small photonic waveguides. The change of n_{eff} as a function of wavelength is negative as well, being about -0.013/nm around $\lambda = 1.55$ μm.

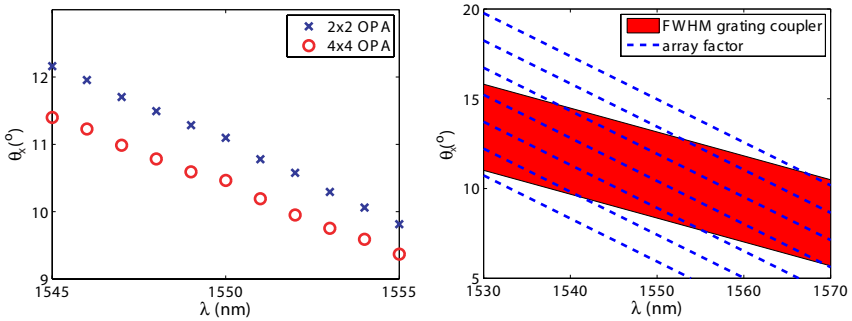

(a) (b)

Figure 6.29: (a) Shift of the peak shown in Figure 6.28 by changing the wavelength. (b) Schematic view of wavelength steering capability. The red region represents the shift of the FWHM of the envelope of the far-field pattern (the far-field pattern of one grating coupler), while the blue dashed lines represents the shift of the individual emission lobes with wavelength.

By changing the wavelength, the envelope of the far-field will shift (Figure 6.26(b)), but also the array factor will shift due to the delay lines. Figure 6.29(a) shows the shift of the peak indicated in Figure 6.28 by an arrow. For the 2×2 OPA this shift is about $-0.24°$/nm whereas for the 4×4 OPA it is $-0.20°$/nm. The latter is smaller since the ratio $\Delta L_x/\Lambda_x$ is smaller. The contribution of dispersion is about $-0.11°$/nm for the 2×2 OPA and $-0.09°$/nm for the 4×4 OPA.

Figure 6.29(b) shows the coverage range as a function of wavelength. Steering could be performed by first steering the envelope while fine tuning is done by steering the array factor. As the envelope shifts, the array factor peaks will shift out of the envelope while new peaks will shift in. Since the peaks are spaced about $\arcsin(\lambda/\Lambda_x) = 1.48°$ (at 1550 nm for a 60 μm spacing), the required wavelength shift for fine tuning is not more than 7 nm. By making the delay lines

$N = M$	$\Lambda_x = \Lambda_y$ (μm)	ΔL_x (μm)	D_{th} (dBi)	D_{meas} (dBi)
2	60	87.2	34.9	37.0
4	60	72.2	40.0	38.4

Table 6.2: Parameters of the measured 2D OPAs.

longer, we actually create a higher order AWG which is more wavelength sensitive, and the required wavelength shift can be decreased.

Steering in the θ_y-direction can be done by incorporating phase tuners. To steer the beam of an $N \times N$ array in the θ_y-direction, N phase tuners are needed where in principle we only need to define the phase difference between each arm.

Link directivity

For the peak indicated by an arrow in Figure 6.28, the antenna directivity is given in Table 6.2. A good agreement with the theory can be seen. For the 2×2 OPA, the gain is even higher because the lower intensity levels are not measured very accurately. A similar link budget can then be calculated as in Section 6.2.3.

6.4 Two-dimensional dispersive beam scanners

While general OPA approaches need active steering of the phases of all the elements, beam steering can also be done by wavelength tuning using diffractive elements. With the use of two dispersive elements one can then scan a two-dimensional space as has been shown in [18].

In this section, we present a fully integrated approach to perform two-dimensional off-chip wavelength scanning using the silicon photonics platform. The steering principle is based on scanning a beam slowly in one direction while it is steered very fast in the other direction using a low and high order grating, respectively. The high order grating consists of an Arrayed Waveguide Grating (AWG). The low order grating is a standard second-order out-coupling grating which performs two tasks: coupling the light off-chip and steering the beam slowly in one direction. The latter steering principle has already been discussed in the 1D and 2D OPAs. The steering speed of such a dispersive OPA is determined by the wavelength sweeping speed, which can happen very fast. These dispersive beam steering elements can find applications in laser scanning, spectroscopy, demultiplexing [19] and spectral pulse shaping applications [20].

Section 6.4.1 deals with the design and fabrication of the dispersive beam scanners. Next, the beam steering measurements and beam steering efficiency are presented.

6.4.1 Design and Fabrication

The two-dimensional dispersive beam scanner is shown schematically in Figure 6.30 and was fabricated using the standard process flow described in Section 4.1. Light coming from the input waveguide is split through a star coupler into 16 waveguides which are spaced at a distance of 2 μm. The delay lines have a width of 800 nm to reduce the phase error due to fabrication errors, apart from the bends, where a tapering to 450 nm occurs to allow very sharp bends. There is a fixed delay length ΔL_y between each waveguide, which forms the AWG. The end of each waveguide tapers to an 800 nm width on which a grating is etched. The period of the grating is 670 nm with a fill factor of 0.5 [21, 22]. The period was changed from 630 nm in the 1D OPA to 670 nm in order to shift the efficiency dip corresponding with vertical out-coupling away from the 1550 nm wavelength region in these 800 nm wide grating couplers (see Figure 6.7(b)).

The grating coupler consists of a second-order grating and will perform two functions here: coupling light out-of-plane and steering the light slowly in the θ_x-direction. The steering in the θ_x-direction is given by the grating

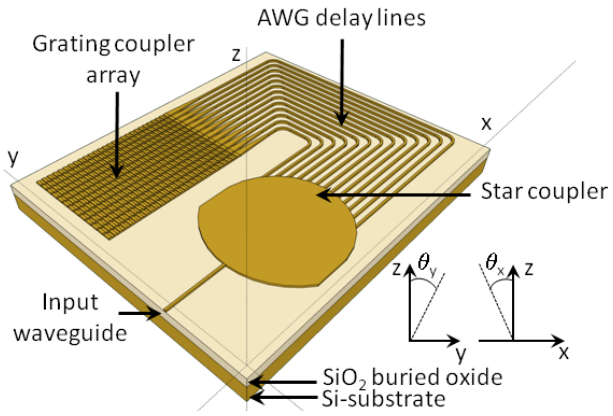

Figure 6.30: Two-dimensional dispersive beam scanner on SOI.

equation (4.6):

$$\sin\theta_x = \frac{\Lambda_{gr} n_{eff,gr} - \lambda}{n_{bg}\Lambda_{gr}}, \tag{6.12}$$

with Λ_{gr} the period of the grating ($\Lambda_{gr} = 670$ nm), λ the free-space wavelength, $n_{eff,gr}$ the effective index of the guided mode in the grating area and n_{bg} the refractive index of the background which is air ($n_{bg} = 1$) in this case. The steering speed is given by

$$\frac{\mathrm{d}\theta_x}{\mathrm{d}\lambda} \approx \frac{\mathrm{d}\sin\theta_x}{\mathrm{d}\lambda} = \frac{\mathrm{d}n_{eff,gr}}{\mathrm{d}\lambda} - \frac{1}{\Lambda_{gr}}, \tag{6.13}$$

where the approximation is valid when the angle θ_x is relatively small. There is also an important dispersion factor $\mathrm{d}n_{eff,gr}/\mathrm{d}\lambda$. Whereas material dispersion is weak for the wavelength range of interest, the waveguide dispersion has a significant influence due to the extremely high confinement in the small photonic waveguides. This dispersion factor is about -8.9×10^{-4}/nm for a 70 nm deep etched grating in a 800 nm wide waveguide.

While the beam is scanned slowly in the θ_x-direction by changing the wavelength, a fast steering is performed in the θ_y-direction due to the AWG. The grating couplers are placed in a N-array configuration with positions $\mathbf{s}_y = n_y\Lambda_y\mathbf{u}_y$, with Λ_y the spacing of the elements in the y-direction and $n = 0\ldots N_y - 1$. Using the formalism discussed in Section 3.1.5, the array factor is given by:

$$T = \frac{\sin[\frac{N_y}{2}(k_0\Lambda_y\sin\theta_y - k_0 n_{eff}\Delta L_y)]}{\sin[\frac{1}{2}(k_0\Lambda_y\sin\theta_y - k_0 n_{eff}\Delta L_y)]}. \tag{6.14}$$

Following Equation (3.31), the array factor is maximum in the θ_y-direction for

$$\sin\theta_y = q\frac{\lambda}{\Lambda_y} + \frac{n_{eff}\Delta L_y}{\Lambda_y}, \tag{6.15}$$

with q an integer, being the order of the AWG. Due to the delay lines, the absolute value of q will be large. The beams will shift at a rate of

$$\frac{\mathrm{d}\theta_y}{\mathrm{d}\lambda} \approx \frac{\mathrm{d}\sin\theta_y}{\mathrm{d}\lambda} = \frac{q}{\Lambda_y} + \frac{\mathrm{d}n_{eff}}{\mathrm{d}\lambda}\frac{\Delta L_y}{\Lambda_y}, \tag{6.16}$$

where the angle θ_y is assumed to be relatively small. Note that q will be negative so that the beam will shift in the negative θ_y-direction for increasing wavelength. The effective index at $\lambda = 1550$ nm for this waveguide is $n_{eff} \approx 2.65$. The change of n_{eff} with wavelength for a 800 nm wide waveguide is negative as well and is about -8.2×10^{-4}/nm around $\lambda = 1550$ nm. The waveguide dispersion is smaller in a wider waveguide. For comparison, the dispersion value is about -0.013/nm in a 450 nm wide waveguide. However, the factor $\Delta L_y/\Lambda_y$ can become large so that the influence of dispersion cannot be neglected.

6.4.2 Measurements

Beam steering

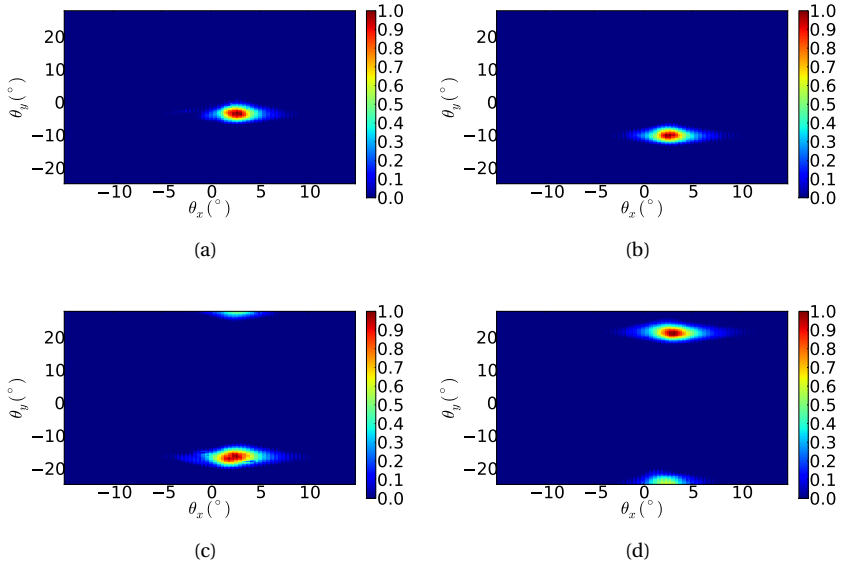

Figure 6.31: Far-field pattern of a beam steering component with an AWG of order $q = -150$ at different wavelengths: (a) 1549 nm, (b) 1550 nm, (a) 1551 nm, (b) 1552 nm.

Different wavelength scanners were fabricated and measured for a wavelength range of 100 nm. The only difference between the components is the

order q of the AWG, which determines the steering speed in the θ_y-direction given by Equation (6.16). Figure 6.31 shows the far field of a beam steering component with an AWG of order $q = -150$ at different wavelengths.

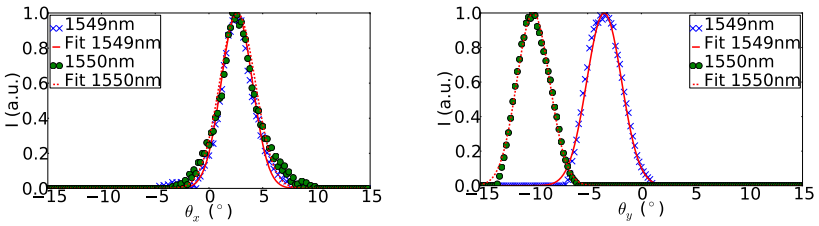

(a) (b)

Figure 6.32: Cross-sectional plots of a beam steerer with an AWG of order $q = -150$ at a wavelength of 1549 nm and 1550 nm: (a) along θ_x, the shift is smaller than the measurement capabilities, (b) along θ_y, a shift of approximately 6.5° can be seen.

In Figure 6.32 a cross-sectional plot of the measured far-fields is given. The mean out-coupling angle is measured to be $\theta_{x,0} = 2.9°$ at $\lambda = 1550$ nm. The FWHM beam width is $3.5° - 4.0°$ in both the θ_x- and θ_y-direction. We can clearly see a very small shift in the θ_x-direction (smaller than the measurement capabilities), while the beam shifts about 6.5° in the θ_y-direction. The position of

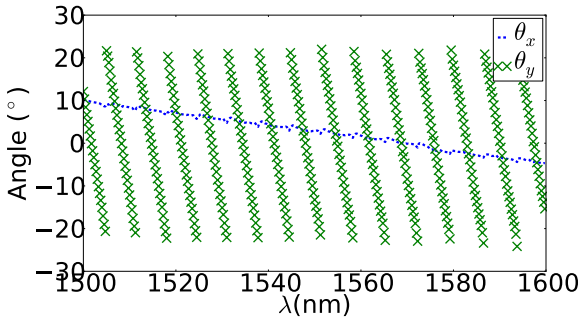

Figure 6.33: θ_x and θ_y position of the beam of a beam steerer with an AWG of order $q = -150$ as a function of wavelength.

the beam for one of the fabricated components with an AWG of order $q = -150$ can be found in Figure 6.33. The θ_x-angle varies slowly while the θ_y-angle varies quickly when changing the wavelength. A total coverage range of $15° \times 50°$ is obtained for a 100 nm wavelength shift. At each jump, we focus on a different lobe emitted by the grating array. This lobe then shifts out of the measurement range

until a new lobe appears. The steering speed given by Equation (6.13) is measured to be $d\theta_x/d\lambda \approx 0.148°/nm$. The steering speed in the θ_y-direction given by Equation (6.16) depends mainly on the order of the AWG and thus on the length difference ΔL_y. The results are summarized in Table 6.3 for the fabricated components. A good agreement with the theoretical expected values can be seen.

ΔL_y (μm)	q	$d\theta_y/d\lambda$ (°/nm) (theory)	$d\theta_y/d\lambda$ (°/nm) (meas.)	FSR (nm)
29.2	-50	-2.1	-2.2	22.7
58.5	-100	-4.2	-4.4	11.4
87.7	-150	-6.4	-6.5	7.7
117.0	-200	-8.5	-8.7	5.7
146.2	-250	-10.6	-10.7	4.7

Table 6.3: Theoretical and measured results of the beam steerers. The last column gives the AWG Free Spectral Range (FSR).

In order to scan the complete 2D space, the beam should shift about 50° in the θ_y-direction when it has shifted 4° in the θ_x-direction (as the FWHM beam width is around 4°). The latter happens over a wavelength range of about 27 nm. The minimum steering speed in the θ_y-direction should thus be around 1.85°/nm. This results in a wavelength resolution of around 2 nm over a 100 nm wavelength range, or 50 resolvable spots in the 2D angular space. The main limitation on this performance is due to the beam width.

The beam width can be decreased in the θ_y-direction by having more waveguides. However, when the delay lines become too long, phase errors due to sidewall roughness will broaden the beam, which was already the case for the higher order AWG ($q = -250$). This can be overcome by optimizing the fabrication process to reduce the sidewall roughness of the delay lines. The beam width in the θ_x-direction depends on the strength of the grating. The strength is strongly dependent on the grating etch depth. Having an etch of less than 70 nm would result in a weaker grating with a longer out-coupling length and thus a narrower beam. This would increase the sensitivity of the component.

Efficiency

There are two main loss factors reducing the steering efficiency. As the spacing of the elements is larger than half a wavelength and the fill-factor is non-unity, there will be a loss of power to the higher orders of emission of the OPA. To quantify the power lost in this way, the simulated far-field in the θ_y-direction is shown in Figure 6.34 for the two extreme cases of steering in the θ_y-direction.

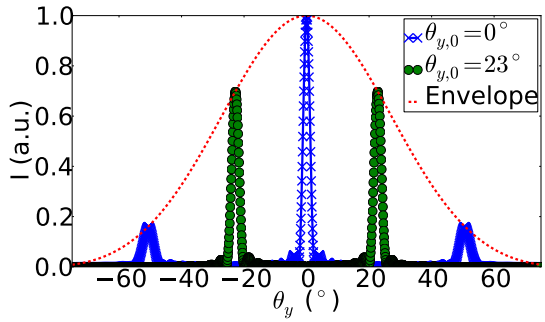

Figure 6.34: Simulated far-field of the wavelength scanner for the two extreme cases of steering in the θ_y-direction: $\theta_y = 0°$ and $\theta_y = 23°$. The red dashed line shows the far-field of one grating coupler.

For wavelengths where $\theta_y = 0°$, about 40% is emitted in the main lobe and 25% is emitted through each of the two other orders of emission, while the remaining 10% is lost in sidelobes between the different output orders. For wavelengths where $\theta_y = 23°$, we are at the situation where a jump occurs to another output order (Figure 6.33). Both output orders now have an equal power of about 45%.

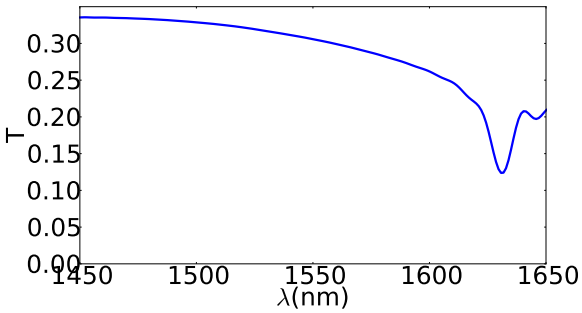

Figure 6.35: 3D-FDTD simulated out-coupling efficiency of a 800 nm wide grating coupler with a grating period of 670 nm as a function of wavelength.

Figure 6.35 shows the out-coupling efficiency calculated using a 3D-FDTD (Finite Difference Time Domain) simulation. The efficiency varies from 33% at 1500 nm to 26% at 1600 nm. The dip near 1630 nm corresponds to the wavelength where the grating acts as a second-order reflection grating. By changing the period of the grating, we can shift the field-of-view to another angular range to ensure operation where the grating strongly couples out light.

6.5 Retroreflectors

Optical retroreflectors provide a versatile way to allow localization and identification of objects or to transmit data using an extra modulating device. Light from a source illuminates the marker, and returns to it due to the action of the retroreflector. When used as a marker, optics has the inherent advantage of working at a small wavelength allowing very precise localization of the markers, compared with RF approaches. Furthermore, there is no problem of electromagnetic interference. However, we are limited by the line-of-sight constraint and typically a limited field-of-view. When used as data transmission nodes (for example in sensor networks), the node typically consists of a bulk corner-cube reflector (CCR) or cat's-eye retroreflector (CERR), together with a transmissive or reflective modulator to impress the data on the retroreflective system. These systems then only require complexity at the base station for tracking the node and data processing, but the nodes can be kept quite simple, low-cost and lightweight.

An example of such a system has been shown in [23], where a corner cube array is used together with a liquid crystal modulator to transmit the data of the 'smart dust motes' and most of the complexity is in the base station. An integrated approach to fabricate retroreflectors makes use of MEMS technology. Such devices are typically useful for short-range applications [24]. In [25], a high contact-angle microdroplet is used to act as a retroreflector with possible applications in optical cross- and inter-connects using photonic integration while in [26], an integrated optical marker for simultaneous localization and identification of objects has been demonstrated. The main drawback in the latter was the limited FOV, which was solved by using a large number of reflectors each looking in different directions.

The retroreflective component discussed in this section can be considered as an OPA as there is an array of radiating elements. As there is no active phase control, the beam can not be steered actively. However, by designing and interconnecting an array of elements in the correct way, a retroreflective structure can be fabricated which will emit a phase front in the same direction as the direction of incidence. Such an integrated on-chip optical retroreflector has applications in chip-readout schemes, active alignment markers, or free-space cross- and inter-connects. It could for example allow data communication between different on-chip photonic layers without the need for very sensitive alignment.

In the current design, the retroreflector has a large FOV (of about 57°) in one-dimension, while the FOV is still limited in the other dimension to about 4°. Only a limited number of retroreflectors is then needed to cover a large FOV. Due to the specific design, the retroreflectivity is wavelength dependent

which allows identification of the retroreflector. By integrating phase tuners, the reflected light can furthermore be modulated without the need of an external modulator. The proposed design can also act as a free-space optical demultiplexer when it is not retroreflecting. The retroreflector is actually the optical analog of an RF Van Atta array antenna [27]. Such an array consists of equally spaced antennas that are interconnected by feeders of the same length. The received RF signal is then retroreflected in the direction of incidence.

Next, the working principle is discussed in Section 6.5.1, followed by the design details in Section 6.5.2. Finally, Section 6.5.3 gives the measurement results and discussion.

6.5.1 Working principle

Intuitive picture

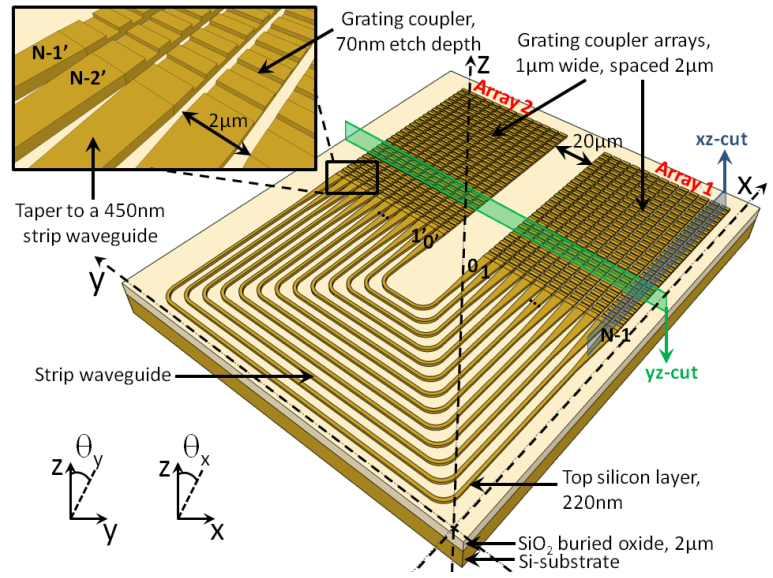

Figure 6.36: Optical retroreflector on SOI.

Figure 6.36 shows a schematic of the retroreflector design. When looking at the xz-cut of the component, the retroreflector simply acts as a reflecting grating. Light at a certain θ_x-angle is coupled into the retroreflector and coupled back out at the same θ_x-angle as there is no wavelength conversion and all the gratings have the same dimensions. The interesting retroreflective behavior occurs in the θ_y-dimension. The impinging wavefront is discretized and interconnected in such a way that the exiting wavefront will have the same angle as the

angle of incidence. To understand the retroreflective behavior in more detail, we need to look at the yz-cut of Figure 6.36 which is given in Figure 6.37.

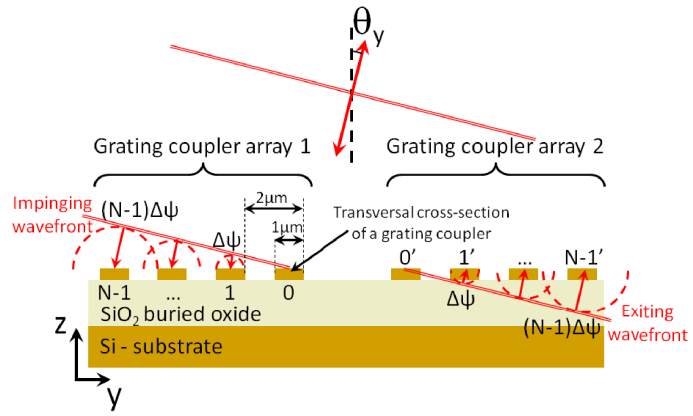

Figure 6.37: Working principle of the retroreflector. Grating couplers 0, 1, … N-1 are connected with grating couplers 0', 1', … N-1'. The incoming wavefront is retroreflected in the same direction.

Figure 6.37 explains the operation principle of the retroreflector. Light that is coupled in using the grating coupler arrays is guided through delay lines and coupled back out through the same grating coupler arrays. Let us first assume that there are no delay length differences between the two grating coupler arrays. Grating couplers 0, 1, …, N-1 are connected with grating couplers 0', 1', …, N-1', respectively. A plane wave impinges on the retroreflector at an angle θ_y. The impinging wavefront on grating coupler array 1 will leave the retroreflector from grating coupler array 2 at the same angle of incidence and vice-versa. When the incident wave front hits grating coupler 0, grating coupler 0' starts radiating. By the time the wave front hits grating coupler 1, grating coupler 1' starts radiating with a phase delay $\Delta\Psi$. This goes on until the wavefront hits grating coupler N-1, and grating coupler N-1' start radiating, which is the exiting phase front depicted in Figure 6.37. The total phase difference between the incoming and exiting phase front shown in Figure 6.37 is the same and equal to $(N-1)\Delta\Psi$ and thus the exiting wave front constructively interferes at the angle of incidence θ_y.

There is a fixed delay length difference ΔL_y between the waveguides. These delay lines between the grating couplers will make the component wavelength dependent. Only when the delay length difference ΔL_y corresponds to a multiple of 2π phase difference, will retroreflectivity be observed:

$$\frac{2\pi}{\lambda} n_{eff} \Delta L_y = q2\pi, \tag{6.17}$$

with λ the free space wavelength, n_{eff} the effective index of the delay lines (being an 800 nm wide waveguide) and q an integer, which is also called the order of the AWG that is formed by these delay lines.

Scalar modeling

The retroreflector behavior in the θ_y-direction is investigated using a scalar approach. From OPA theory, we know that the FOV in the θ_y-direction is determined by the FOV of one grating coupler. The full 1/e mode amplitude width in the y-direction of the fundamental TE-like mode of a 1 μm wide grating coupler is simulated to be about 0.795 μm at 1550 nm and does not vary much with wavelength. It is this field that is coupled out by the grating coupler. The FWHM of the far-field of one such Gaussian is then 57° which is the FOV of the retroreflector shown as the red dashed line in Figure 6.38.

The complete retroreflector is simulated in the θ_y-direction as 2 arrays of 50 Gaussians with a 1/e width of 0.795 μm, spaced 2 μm and with an inner spacing of 20 μm as shown in Figure 6.36 and Figure 6.37. A plane wave impinges on the structure and the overlap of the impinging fields with the grating coupler mode is calculated. These fields are then guided through the delay lines and are coupled back off-chip. The far-field of all these (100) Gaussian profiles, taking into account their phase difference, can then be calculated and is shown as the full blue line in Figure 6.38. In this figure, the structure is simulated for the case that condition (6.17) is fulfilled.

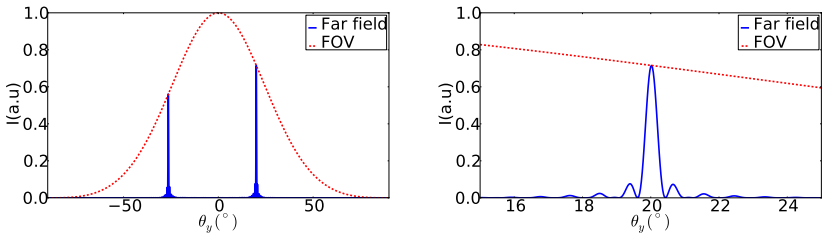

Figure 6.38: (a) Simulated far-field of the retroreflector for an impinging wave at θ_y=20.0° at λ=1523 nm. The dashed line shows the far-field of one grating coupler being the envelope of the far-field pattern. (b) Magnification of (a) at the retroreflective angle.

The beam width of the retroreflected field is determined by the total size of the grating coupler arrays. The FWHM was simulated to be 0.33°. A second beam can also be seen in Figure 6.38(a). This is not a retroreflected beam but is present due to the sampling of our incoming field. When having an array

of radiating apertures, spaced at a distance Λ_y, different lobes are emitted at an angle of $\arcsin(\lambda/\Lambda_y)$ (Equation (3.33)), with λ the free-space wavelength, which is well-known from OPA theory. This results in a lobe spacing of about 50° at λ=1523 nm which is the spacing visible in Figure 6.38(a). This specific wavelength is chosen as it is (one of) the operating wavelengths of the fabricated retroreflectors, given by Equation (6.17).

When condition (6.17) is no longer fulfilled, the demultiplexing effect of the AWG comes into play. In Figure 6.39, a close up of the far-field is shown for different wavelength offsets $\Delta\lambda$. Two reflected lobes now arise which move away from the retroreflective direction for increasing wavelength offsets. The two lobes that are present correspond to the field emitted by grating coupler array 1 and 2, respectively (Figure 6.37). Eventually, they will reach back to the same retroreflective direction when the condition (6.17) is again fulfilled, this time for another integer m, which occurs for a wavelength shift of $\Delta\lambda = 51$ nm. The grating period determines the FOV in the θ_x-direction from the grating equation (4.6):

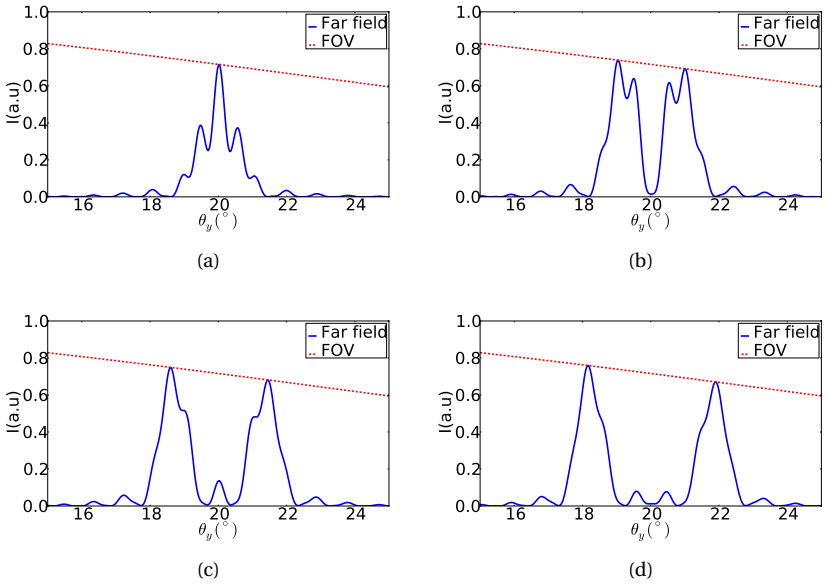

Figure 6.39: Influence of the wavelength on the retroreflectivity in the θ_y-direction: (a) $\Delta\lambda$ = 0.5 nm, (b) $\Delta\lambda$ = 1.0 nm, (c) $\Delta\lambda$ = 1.5 nm, (d) $\Delta\lambda$ = 2.0 nm., where $\Delta\lambda = |\lambda - \lambda_0|$ with λ_0 being the retroreflective wavelength.

$$\sin\theta_x = \frac{\Lambda_{gr} n_{eff,gr} - \lambda}{n_{bg}\Lambda_{gr}}, \tag{6.18}$$

with Λ_{gr} the period of the grating, λ the free-space wavelength, $n_{eff,gr}$ the effective index of the guided mode in the grating area and n_{bg} the refractive index of the background. By having a different grating period, each retroreflector will work at a different, limited θ_x-range, but a large θ_y-range. This limitation is overcome by fabricating different retroreflectors with different grating periods.

When for a certain wavelength and at a certain angle Equation (6.18) is no longer fulfilled, another retroreflector will light up. In this way, there will be retroreflectivity observed for different θ_x-angles for a specific wavelength and a large θ_x-range is covered. The beam width of the reflected light in the θ_x-direction depends on the out-coupling strength of the grating. As we are working with 70 nm deep etched gratings, the grating strength is high resulting in a short out-coupling length and thus a relatively large FWHM beam width of about $3° - 4°$, which is then the FOV of the retroreflector in the θ_x-direction at a specific wavelength.

6.5.2 Design and Fabrication

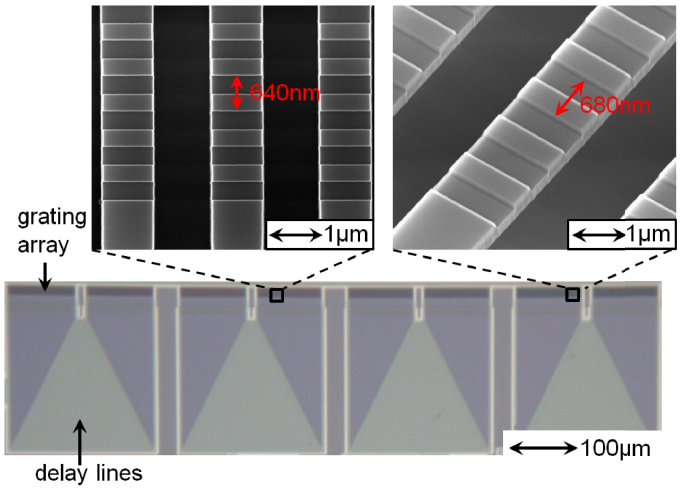

Figure 6.40: Microscope image of the fabricated retroreflectors. Four different retroreflectors are shown with grating periods ranging from 620 nm (left) to 680 nm (right) in steps of 20 nm.

The retroreflector shown in Figure 6.36 was fabricated on SOI using the standard process flow described in Section 4.1. The delay lines have a width of 800 nm, apart from the bends which are tapered to a 450 nm width to allow very sharp bends, with a bend radius down to 3 μm. A waveguide width of 800 nm is used to reduce phase errors in the delay lines as a wide waveguide is more tol-

erant to fabrication errors. The length difference is the same for all retroreflectors and equal to 12 μm. These delay lines form an Arrayed Waveguide Grating (AWG). Finally a BCB layer of about 800 nm is spun on top of the structure, and the structure is covered with a 500 nm gold layer, apart from the grating coupler areas. This reduces interference arising from diffuse reflected light from other parts of the chip which would interfere with the retroreflected signal.

The grating couplers have a width of 1 μm and are spaced 2 μm apart. The retroreflectors consist of two arrays of 50 grating couplers which are interconnected as shown in Figure 6.36. The gratings have a fill factor of 0.5. Four different retroreflectors were fabricated with grating periods ranging from 620 nm up to 680 nm in steps of 20 nm as shown in Figure 6.39. The retroreflectivity for the different retroreflectors will thus occur at the same wavelengths (Equation (6.17)), but at a different θ_x-angle due to the difference in grating period (Equation (6.18)).

6.5.3 Measurements

Setup

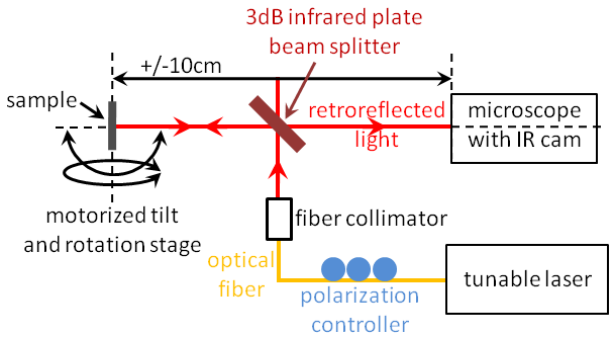

Figure 6.41: Measurement setup to characterize the optical retroreflectors. The infrared light is split through a 3 dB splitter illuminating the sample. The sample is positioned in the center of a tilt and rotation stage. The reflected light is captured by a microscope with an infrared camera for different orientations of the sample.

The measurement setup is shown in Figure 6.41. Light from a tunable laser passes through a polarization controller to a fiber collimator with a $1/e^2$ beam diameter of 7 mm. The collimated beam is then split through an infrared 3 dB plate beam splitter. Half of the light goes to the sample which is positioned in the rotation and tilt center of a motorized rotation and tilt stage, as discussed in Section 6.1.2. This large beam then illuminates different retroreflectors.

The retroreflected light is then guided back to the 3 dB plate beam splitter, where half of the light will be captured by the microscope and infrared camera. When the light impinges perpendicularly on the structure, we get a large reflected beam due to specular reflection. By rotating and tilting the sample, the retroreflected light can be investigated. The numerical aperture of the microscope is about 0.1 meaning that we will measure the retroreflected light as long as the reflected light is in a cone with half-angle of 5.7° around the direction of incidence. More light than only the retroreflected light is captured, which is a limitation of our measurement setup.

Results

In Figure 6.42, the measured retroreflectivity is shown for different θ_x-angles. The four different retroreflectors operate at different θ_x-angles, while the wavelength is kept constant at 1523 nm. For this wavelength, condition (6.17) is fulfilled and retroreflectivity is observed. In these images the θ_y-angle is kept constant at 20°. We can clearly see the two grating coupler arrays of the retroreflectors lighting up at the same time.

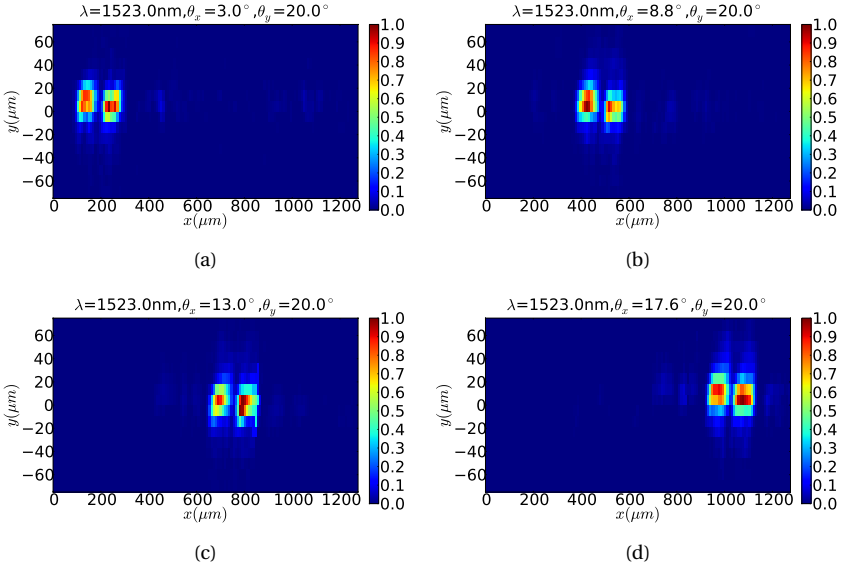

Figure 6.42: Measured retroreflectivity at different θ_x-angles at λ=1523 nm. The four different retroreflectors operate at the angles (a) $\theta_x = 3.0°$, (b) $\theta_x = 8.8°$, (c) $\theta_x = 13.0°$, (d) $\theta_x = 17.6°$. The θ_y-angle is kept fixed at $\theta_y = 20.0°$.

In Figure 6.43, the range for which retroreflectivity was measured is given.

The chip was rotated to different θ_x- and θ_y-angles and the image is then recorded. This image is then integrated and the result (normalized to 1) is shown as a color plot in Figure 6.43. Each retroreflector works for a limited θ_x-range of about 4°, while the measured θ_y-range goes from 0° to 25° and due to symmetry retroreflectivity will be observed for a span of more than 50°, which compares to the theoretical FWHM span of 57° shown in Figure 6.38(a). When the θ_x- and θ_y-angle reaches 0°, the measurement is saturated by the specular reflection of the chip, therefore these small angles are not shown in Figure 6.43, but the influence of the specular reflection is still visible for small angles.

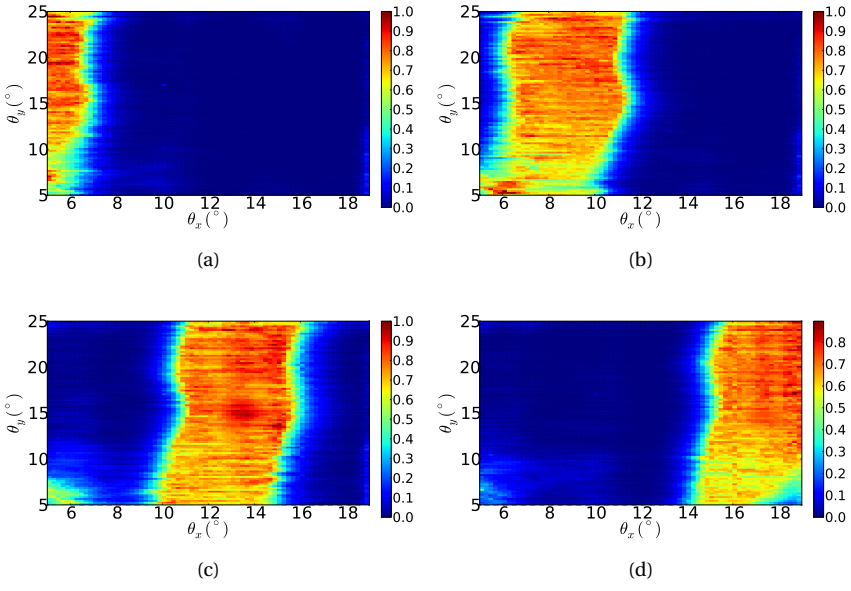

Figure 6.43: Measured retroreflectivity range at λ=1523 nm for four different retroreflectors. Each retroreflector works for a limited θ_x-range, but a large θ_y-range. (a) Λ_{gr} = 620 nm, (b) Λ_{gr} = 640 nm, (c) Λ_{gr} = 660 nm, (d) Λ_{gr} = 680 nm.

The retroreflectivity was observed for a wavelength range of about 5 nm around 1523 nm. This is because the numerical aperture (NA) of the microscope captures more light than only the retroreflected light. As the wavelength increases, two lobes arise moving away from the retroreflective direction as shown in Figure 6.39, but these two lobes are still captured by the microscope.

When used in optical marker applications, one is interested in the power efficiency of these markers. Therefore, 3D-FDTD (Finite Difference Time Domain) simulations are performed to investigate the grating coupler efficiency as

a function of wavelength [4]. The result is shown in Figure 6.44. For a grating period of $\Lambda_{gr} = 620$ nm, there is a dip in the efficiency within the calculated spectral range. This dip is again due to Bragg-coupling between the guided mode in the chip and a surface-normal diffraction order, as well as to the occurrence of second-order coupling between the guided mode and its backward mode. For the larger grating periods, this dip shifts to larger wavelengths and is not visible anymore in the graph. The efficiency of the different gratings at the retroreflective wavelength λ=1523 nm is similar for all retroreflectors and equal to about 34%.

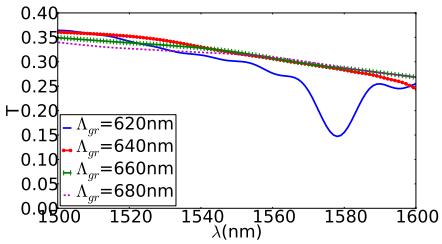

.

Figure 6.44: 3D-FDTD simulated out-coupling efficiency of a 1 μm wide grating coupler as a function of wavelength for different grating periods.

These retroreflectors can be modulated on-chip to transmit data. The simplest method of modulation is to heat the chip. By heating up the delay lines, condition (6.17) will no longer be fulfilled for the same wavelength and the retroreflectivity will disappear, which we have measured experimentally by heating up the complete chip. The phase relation could also be destroyed using other phase tuning techniques discussed in Chapter 5.

6.6 Conclusions

Several optical phased arrays on SOI were presented. Using the array principle with integrated heaters, we have shown 1D steering over the complete FOV, which can be more than 120° using integrated nanophotonic waveguides. By having full phase control over all the elements, there is furthermore the possibility to program a certain phase front to focus light above chip. This is especially useful in sensing applications. Efficient light collection of scattered light into a single mode waveguide can also be done using a similar approach as we can tune the phases to coherently add all the contributions. We have furthermore also shown a DOA measurement which is useful in wavefront sensing applications or optical link setup.

A two-dimensional OPA was presented showing a typical OPA radiation pattern in 2D. Due to the low fill factor and large element spacing, multiple higher order lobes were visible in the far-field. Directivity of the beam, however, scales with the total radiating aperture, and is relatively independent of spacing or fill factor. Integrating phase tuners would allow steering over the complete FOV.

Next, a two-dimensional dispersive wavelength scanner was presented allowing free-space multiplexing using a single integrated component. These components can furthermore be very useful in pulse shaping applications. Finally a retroreflective structure was presented sending a plane wave back to its direction of incidence. This can be useful in chip-readout schemes or optical marker applications.

References

[1] N. Le Thomas, R. Houdré, M. V. Kotlyar, D. C. O'Brien, and T. F. Krauss. *Exploring light propagating in photonic crystals with Fourier optics.* Journal of the Optical Society of America B, 24(12):2964–2971, 2007.

[2] Joseph W. Goodman. *Introduction to Fourier Optics.* McGraw-Hill, Inc., 1986.

[3] K. Van Acoleyen, W. Bogaerts, J. Jágerská, N. Le Thomas, R. Houdré, and R. Baets. *Off-chip beam steering with a one-dimensional optical phased array on silicon-on-insulator.* Optics Letters, 34(9):1477–1479, 2009.

[4] A. F. Oskooi, D. Roundy, M. Ibanescu, P. Bermel, J. D. Joannopoulos, and S. G. Johnson. *MEEP: A flexible free-software package for electromagnetic simulations by the FDTD method.* Computer Physics Communications, 181:687–702, January 2010.

[5] D. N. Kwong, Zhang Yang, A. Hosseini, and R. T. Chen. *Integrated optical phased array based large angle beam steering system fabricated on silicon-on-insulator.* Proceedings of the SPIE - The International Society for Optical Engineering, 7943:79430Y–1 – 79430Y–6, 2011.

[6] Karel Van Acoleyen, Katarzyna Komorowska, Wim Bogaerts, and Roel Baets. *One-Dimensional Off-Chip Beam Steering and Shaping Using Optical Phased Arrays on Silicon-on-Insulators.* IEEE Journal of Lightwave Technology, 29(23):3500–3505, 2011.

[7] Y. Li, S. Meersman, and R. Baets. *Realization of fiber based laser Doppler vibrometer with serrodyne frequency shifting.* Applied Optics, 50(17):2809–2814, 2011.

[8] G. Yurtsever, P. Dumon, W. Bogaerts, and R. Baets. *Integrated photonic circuit in silicon on insulator for Fourier domain optical coherence tomography.* In Proceedings of SPIE-The International Society for Optical Engineering, volume 7554, 2010.

[9] Nur Ismail, Bakiye Imran Akcan, Fei Sun, Kerstin Wörhoff, Réne M. de Ridder, Markus Pollnau, and Alred Driess. *Integrated approach to laser delivery and confocal signal detection.* Optics Letters, 35(16):2741–2743, 2010.

[10] Karel Van Acoleyen, Eva Ryckeboer, Katarzyna Komorowska, and Roel Baets. *Light collection from scattering media in a silicon photonics integrated circuit.* In IEEE Photonics 2011 Conference (IPC11), page WR4, Arlington, Virginia, 2011.

[11] N. Ismail, F. Sun, K. Worhoff, A. Driessen, R. M. de Ridder, and M. Pollnau. *Excitation and Light Collection From Highly Scattering Media With Integrated Waveguides.* IEEE Photonics Technology Letters, 23(5):278–280, 2011.

[12] Chao Geng, Xinyang Li, Xiaojun Zhang, and Changhui Rao. *Coherent beam combination of an optical array using adaptive fiber optics collimators.* Optics Communications, 284(24):5531–5536, 2011.

[13] Python. *SciPy.* http://www.scipy.org/.

[14] P. G. Agrawal. *Fiber-Optic Communication Systems.* John Wiley and Sons, Inc, 2002.

[15] R. J. Green, H. Joshi, M. D. Higgins, and M. S. Leeson. *Recent developments in indoor optical wireless systems.* IET Communications, 2(1):3–10, 2008.

[16] F. Van Laere, T. Claes, J. Schrauwen, S. Scheerlinck, W. Bogaerts, D. Taillaert, L. O'Faolain, D. Van Thourhout, and R. Baets. *Compact focusing grating couplers for silicon-on-insulator integrated circuits.* IEEE Photonics Technology Letters, 19(21-24):1919–1921, 2007.

[17] K. Van Acoleyen, H. Rogier, and R. Baets. *Two-dimensional optical phased array antenna on silicon-on-insulator.* Optics Express, 18(13):13655–13660, 2010.

[18] T. Chan, E. Myslivets, and J. E. Ford. *2-Dimensional beamsteering using dispersive deflectors and wavelength tuning.* Optics Express, 16(19):14617–14628, 2008.

[19] J. Y. Yang, X. Q. Jiang, M. H. Wang, and Y. L. Wang. *Two-dimensional wavelength demultiplexing employing multilevel arrayed waveguides.* Optics Express, 12(6):1084–1089, 2004.

[20] V. R. Supradeepa, C. B. Huang, D. E. Leaird, and A. M. Weiner. *Femtosecond pulse shaping in two dimensions: Towards higher complexity optical waveforms.* Optics Express, 16(16):11878–11887, 2008.

[21] K. Van Acoleyen, W. Bogaerts, H. Rogier, and R. Baets. *Two-dimensional Dispersive Beam Steerer Fabricated on Silicon-On-Insulator.* In 7th International Conference Group IV Photonics (GFP 2010), page FC7, Beijing, China, 2010.

[22] Karel Van Acoleyen, Wim Bogaerts, and Roel Baets. *Two-dimensional Dispersive Off-chip Beam Scanner Fabricated on Silicon-On-Insulator.* IEEE Photonics Technology Letters, 23(17):1270–1272, 2011.

[23] D. C. O'Brien, J. J. Liu, G. E. Faulkner, S. Sivathasan, W. W. Yuan, S. Collins, and S. J. Elston. *Design and Implementation of Optical Wireless Communications with Optically Powered Smart Dust Motes.* IEEE Journal on Selected Areas in Communications, 27(9):1646–1653, 2009.

[24] P. G. Goetz, W. S. Rabinovich, R. Mahon, L. Swingen, G. C. Gilbreath, J. L. Murphy, H. R. Burris, M. F. Stell, and Ieee. *Practical considerations of retroreflector choice in modulating retroreflector systems.* 2005 Digest of the LEOS Summer Topical Meetings, New York, 2005. IEEE.

[25] E. L. Landry, B. Born, G. Ross, and J. F. Holzman. *Integrated photonic retroreflectors for lateral cross-connects and interconnects.* In 2010 IEEE 23rd Canadian Conference on Electrical and Computer Engineering - CCECE 2010, pages 1–4, Calgary, AB, Canada, 2010. IEEE.

[26] M. Verbist, W. Bogaerts, J. Schrauwen, and R. Baets. *Silicon-on-Insulator-Based Retroreflective Optical Marker Chips for Simultaneous Identification and Localization.* IEEE Journal of Selected Topics in Quantum Electronics, 15(5):1427–1431, 2009.

[27] K. Nagai. *Van Atta Array Antenna Device.* United States Patent US3731313, 1973.

7 Conclusions and perspectives

7.1 Conclusions

With the increasing bandwidth of the wired networks, there is a need to increase the bandwidth of wireless networks. The most straightforward option is to follow the same trend that the wired world has undergone, i.e., to go to the optical domain. The advantages and disadvantages of optical wireless networks compared to RF networks have therefore been investigated. The main conclusion is that high speed optical links required LOS links, preferably with beam steering to get a large coverage range.

Beam steering was investigated using a phased array approach. The phased array principle is a non-mechanical way for beam steering allowing rapid and precise beam steering. The theoretical principles have been reviewed, where a large overlap with RF theory can be seen. Such beam steering components do not only have applications in wireless communication, but also in interconnecting, scanning or sensing.

To bring these beam steering elements to a large number of application areas, it is interesting to fabricate these in a low-cost and possibly high volume approach. Therefore, we have investigated the possibilities of the silicon photonics platform to fabricate these beam steering elements. This platform allows the fabrication of very small structures and compact phase modulators bringing the key ingredients to fabricate an OPA together in an integrated platform.

Using this platform, integration with electronics becomes possible as well.

The one-dimensional OPAs are especially promising as we can reach high fill factors and narrow spacings resulting in a very large steering range. Several applications such as steering, efficient light collection and direction-of-arrival estimation have been investigated. One of the advantages of these structures is that light is captured into a single mode waveguide. This allows further processing in the optical domain such as optical filtering, splitting or coherent detection. Using an extra steering approach with another (e.g., LC based) beam steering component, two-dimensional coverage can be obtained. Another approach is to use wavelength as an extra variable. This also results in a two-dimensional steering range.

Two-dimensional integrated OPAs suffer from low fill-factor issues and thus limited steering efficiencies. We have also looked into a dispersive beam steering approach where a two-dimensional space can be addressed by wavelength only. Apart from optical links schemes, these are also useful in pulse shaping or spectroscopy applications. Finally, a passive retroreflective design was investigated that sends a light beam back to its direction of incidence.

We have thus shown several proof-of-principle components clearly showing the potential of the silicon photonics platform in beam steering applications. As there are several phase tuning techniques available, steering can happen very fast in for example free-space switching or scanning applications.

7.2 Perspectives

As the basic components have been investigated, future work lies in the use of these components in actual link or sensing designs. One first needs to carefully specify the needed functionality so that the integrated OPA can be designed accordingly. Integration of photodiodes and electronic post-processing on these structures can further increase the functionality and sensitivity. Depending on the application, there is also still room for improvement by for example specialized grating designs or by using extra optics. The photonic chip can be for example at the heart of a LIDAR system, where extra optics is used to increase collectivity.

As these OPAs actually capture the light in an electro-magnetic mode (as opposed to a simple photodiode) on-chip, a variety of applications becomes possible: optical data filtering, coherent detection, adaptive optics applications, wavefront sensing, interconnecting, interferometry, optical MIMO, LIDARs, optical scanning, biosensing ... The OPA then lies at the center of each of these applications. Integration of feedback loops to continuously monitor the actual measured or applied phase will furthermore result in more stable and reliable components that can compensate for e.g., thermal drift issues. If electronics is

furthermore integrated, very advanced functionality becomes possible at possibly low-cost.

Of course each of the above mentioned application domains is a complete research field on its own. This shows that the future research potential of these basic steering elements is large and may inspire a lot of new and exciting applications.

A

Fourier Imaging Setup

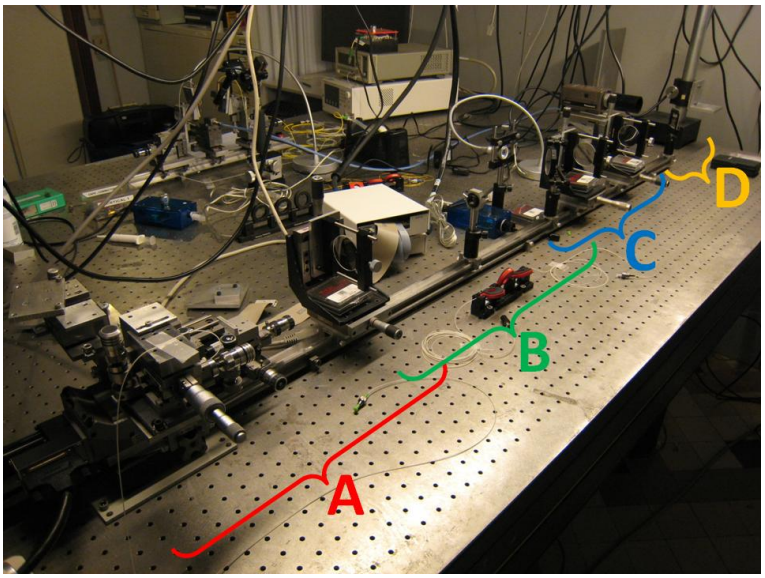

Figure A.1: Practical realization of a Fourier imaging setup.

In this Appendix, the practical realization of the Fourier imaging setup, dis-

cussed in Chapter 6 is given. Figure A.1 shows a general layout. The parts indicated in this Figure are given in detail in Figures A.2- A.5. Figure A.2 shows the sample mount, which is discussed in detail in Section 6.1.2. The probe card is not visible anymore in this picture. Next to the sample mount, the microscope objective can be found, mounted on a 3D translation stage and a small tilt stage to adjust the angle. After the MO, the plano-convex lens is mounted. Figure A.3 shows the real-space filter and visible light excitation with the 3dB plate beam splitter. The positioning of the latter is not so crucial as it is just meant to get some visible light into the setup to align the sample. Figure A.4 again shows the visible light excitation and the two other mounted lenses. To do Fourier imaging, the bi-convex lens needs to be removed. Figure A.5 shows the visible mirror to guide the light to the visible camera. When working in the infrared, the mirror is removed and light will hit the infrared camera (of which the mount is only shown). Note that the setup was optimized for Fourier imaging and not for real-space imaging.

The sample is typically excited through a near-vertical grating coupler that couples light at an angle of 10° to the normal of the sample. As there is only little space between the MO and the sample, the fiber is sent through a bent needle to reach the 10° angle. The fibers are aligned using a small microscope that is movable around the sample as shown in Figure A.6.

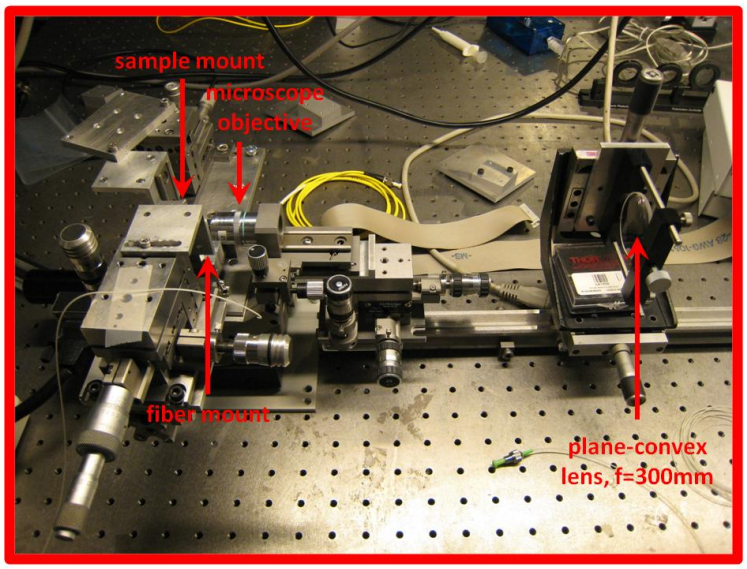

Figure A.2: Part A of Figure A.1.

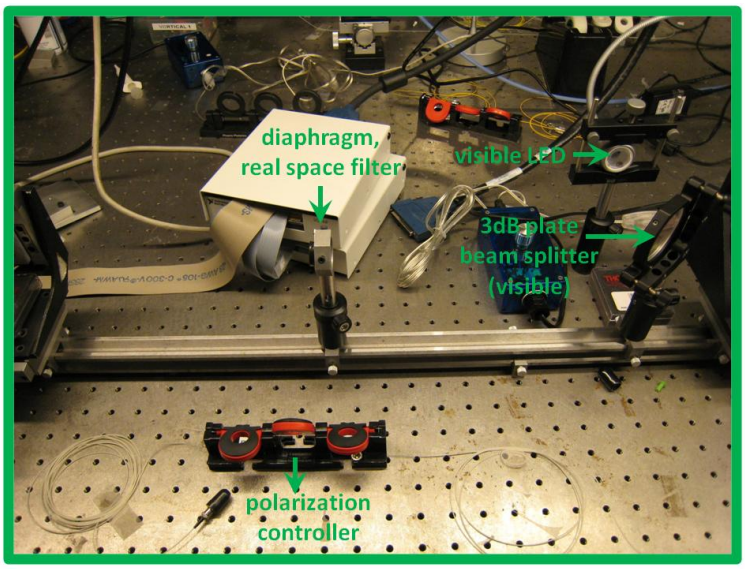

Figure A.3: Part B of Figure A.1.

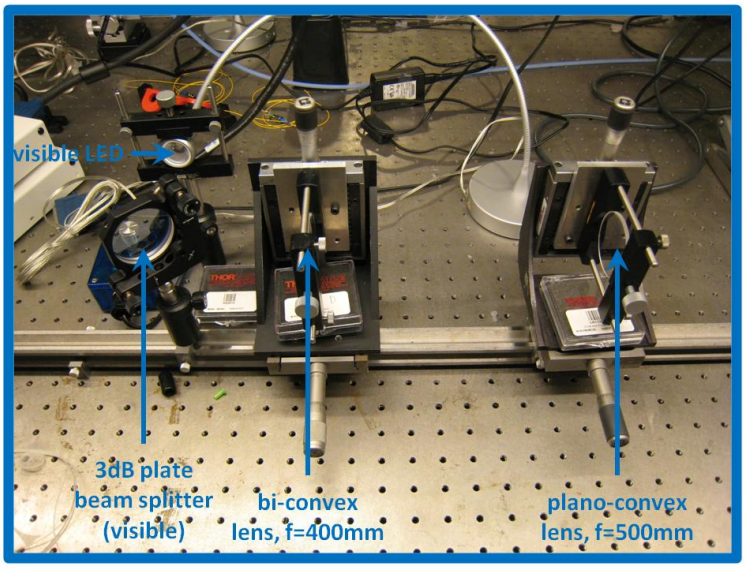

Figure A.4: Part C of Figure A.1.

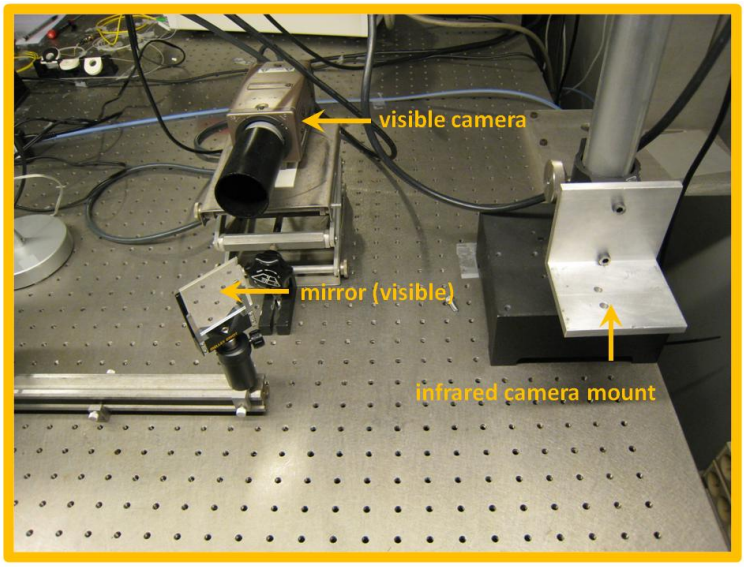

Figure A.5: Part D of Figure A.1.

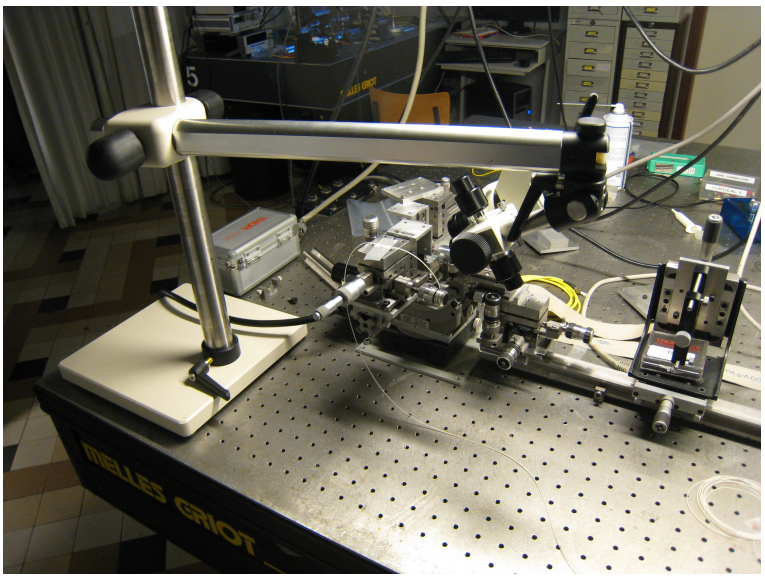

Figure A.6: A movable microscope is mounted to align the fibers.